

# Improving Circuit Performance in a Trapped-Ion Quantum Computer

by

Bichen Zhang

Department of Electrical and Computer Engineering  
Duke University

Date: \_\_\_\_\_

Approved:

---

Kenneth R. Brown, Advisor

---

Jungsang Kim

---

Christopher Monroe

---

Iman Marvian

---

Yiran Chen

Dissertation submitted in partial fulfillment of the requirements for the degree of  
Doctor of Philosophy in the Department of Electrical and Computer Engineering  
in the Graduate School of Duke University  
2021

**ABSTRACT**  
(Electrical and Computer Engineering)

Improving Circuit Performance in a Trapped-Ion  
Quantum Computer

by

Bichen Zhang

Department of Electrical and Computer Engineering  
Duke University

Date: \_\_\_\_\_

Approved:

---

Kenneth R. Brown, Advisor

---

Jungsang Kim

---

Christopher Monroe

---

Iman Marvian

---

Yiran Chen

An abstract of a dissertation submitted in partial fulfillment of the requirements for  
the degree of Doctor of Philosophy in the  
Department of Electrical and Computer Engineering  
in the Graduate School of Duke University  
2021

Copyright © 2021 by Bichen Zhang  
All rights reserved except the rights granted by the  
Creative Commons Attribution-Noncommercial Licence

# Abstract

A quantum circuit is a widely used model for quantum computation. It consists of quantum registers, which we refer to as qubits, and quantum gates. To build a large-scale trapped ion quantum computer, the performance of executing quantum circuits is a bottleneck. Atomic ions are great qubit candidates. However, high-fidelity two-qubit gates extending over all qubits with individual control in a large-scale trapped-ion system have not been achieved. Moreover, coherent gate errors in deep quantum circuits exaggerate the error since they accumulate quadratically. This thesis presents the effort to build a trapped-ion quantum computing system that possesses individual qubit control, scalable high-fidelity two-qubit gates, and the capability to run quantum circuits with multiple qubits. This thesis shows that we realize and characterize high-fidelity two-qubit gates in a system with up to 4 ions using radial modes. The ions are individually addressed by two tightly focused beams steered using micro-electromechanical system (MEMS) mirrors. We accomplish the highest two-qubit gate fidelity using radial motional modes to date. Two methods of robust frequency-modulated two-qubit gate pulse design are introduced. With the state-of-the-art scalable two-qubit gates, we propose a compilation technique, which we refer to as hidden inverses, that creates circuits robust to residual coherent errors. We present experimental data showing that hidden inverses suppress both overrotation and phase misalignment errors in our trapped-ion system, resulting in improved quantum circuit performance.

To my family.

# Contents

<b>Abstract</b>	<b>iv</b>
<b>List of Tables</b>	<b>x</b>
<b>List of Figures</b>	<b>xi</b>
<b>Acknowledgements</b>	<b>xiv</b>
<b>1 Introduction</b>	<b>1</b>
1.1 Quantum Computing Overview . . . . .	2
1.2 Quantum Computing with Trapped Ions . . . . .	4
1.3 Thesis Overview . . . . .	6
<b>2 A Hyperfine Qubit</b>	<b>7</b>
2.1 Hyperfine Qubit . . . . .	8
2.2 Ion Loading: Ionization and Doppler Cooling . . . . .	9
2.3 State Initialization and Detection . . . . .	14
2.4 EIT Cooling . . . . .	14
2.5 Surface Electrode Ion Traps . . . . .	19
2.6 Radial Motional Modes . . . . .	22
<b>3 Quantum Gates with Trapped Ions</b>	<b>25</b>
3.1 Raman Transitions . . . . .	26
3.2 Single-Qubit Gates . . . . .	30
3.3 Mølmer Sørensen Gates . . . . .	33

3.4	Modulated MS Gate Simulation . . . . .	38
3.4.1	Error model . . . . .	38
3.4.2	Pauli transfer matrix . . . . .	40
<b>4</b>	<b>Experimental Hardware and Control</b>	<b>42</b>
4.1	Ultra-High Vacuum Environment . . . . .	42
4.2	Optical Design for CW and Ablation lasers . . . . .	45
4.2.1	Beam modulation for 369 nm beam . . . . .	46
4.2.2	Beam delivery system . . . . .	48
4.2.3	Imaging system . . . . .	50
4.3	Optical Design for Raman Beams . . . . .	50
4.3.1	Beam modulation . . . . .	50
4.3.2	Beam delivery . . . . .	53
4.4	Experimental Control System . . . . .	53
4.4.1	Real-time incoherent control subsystem . . . . .	53
4.4.2	Real-time coherent control subsystem . . . . .	55
4.4.3	Off-line control subsystem . . . . .	57
<b>5</b>	<b>Quantum Gates in Experiments</b>	<b>59</b>
5.1	Single-qubit Gates . . . . .	59
5.1.1	Gate Set Tomography . . . . .	63
5.2	High Fidelity Discrete FM MS Gates . . . . .	67
5.2.1	Introduction . . . . .	67
5.2.2	Experimental setups . . . . .	69
5.2.3	Discrete FM MS gates . . . . .	70
5.2.4	Calibration pipeline . . . . .	72
5.2.5	Results . . . . .	73

5.2.6	Error analysis . . . . .	75
5.2.7	Conclusions . . . . .	76
5.2.8	Performance in a upgraded system . . . . .	77
5.3	High Fidelity Batch-Robust FM MS Gates . . . . .	78
5.3.1	Introduction . . . . .	79
5.3.2	Robustness conditions . . . . .	80
5.3.3	Experimental results . . . . .	82
<b>6</b>	<b>Quantum Circuit Performance Optimization</b>	<b>86</b>
6.1	Introduction . . . . .	86
6.2	Designing gates to control systematic error . . . . .	87
6.3	Experiment implementation of an arbitrary quantum circuit . . . . .	92
6.4	Hidden inverse experimental performance . . . . .	94
6.5	Alternative methods for reducing systematic errors . . . . .	97
6.5.1	Two-Qubit SK1 Composite Pulses . . . . .	97
6.5.2	Randomized Compiling . . . . .	99
6.5.3	Hardware Specific Compilation . . . . .	100
6.5.4	Total optimization . . . . .	101
6.6	Conclusions and outlook . . . . .	101
<b>7</b>	<b>Conclusions</b>	<b>103</b>
7.1	Conclusions . . . . .	103
7.2	Outlooks . . . . .	105
<b>A</b>	<b>Two-dimensional Motional State Reconstruction</b>	<b>108</b>
<b>B</b>	<b>Phase Issues in Experiments and Simulations</b>	<b>113</b>
B.1	Optical Phase Continuity in FM MS Gate Simulation . . . . .	113
B.2	RFSoc Phase Synchronization . . . . .	114

Bibliography	117
Biography	130

# List of Tables

3.1	Approximate magnitudes of the angular frequencies appearing in Fig. 3.1 for $^{171}\text{Yb}^+$ . . . . .	28
5.1	Mølmer-Sørensen gate error budget . . . . .	75
5.2	The updated Mølmer-Sørensen gate error budget . . . . .	78

# List of Figures

1.1	A qubit state $ \psi\rangle$ represented in a Bloch sphere . . . . .	3
2.1	Relevant energy levels of $^{171}\text{Yb}^+$ ions in quantum computing experiments	9
2.2	Microwave transition spectrum . . . . .	10
2.3	Relevant transitions in Doppler cooling procedure . . . . .	12
2.4	Relevant energy level diagram for optical pumping and detection . . .	13
2.5	A general three-level structure driven by two fields . . . . .	15
2.6	EIT cooling illustration . . . . .	17
2.7	Experimental red sideband absorption spectrum before and after EIT cooling . . . . .	20
2.8	A photo of the Phoenix trap . . . . .	21
2.9	Motional modes coupling strength matrices . . . . .	23
3.1	A general three-level system associated with motion . . . . .	27
3.2	Pauli transfer matrix for an $XX(\pi/4)$ gate . . . . .	40
4.1	CAD drawings of the Ultra-high vacuum chamber . . . . .	43
4.2	Photos of customized back flange and back flange assembly . . . . .	44
4.3	Photos of the Phoenix trap and the ablation target installed in the chamber . . . . .	45
4.4	Schematics of 369 nm laser beam path . . . . .	46
4.5	Schematics of the offset frequency stabilization . . . . .	47
4.6	CW laser beam delivery system . . . . .	48

4.7	Ray tracing diagram of the two-stage imaging system generated by Zemax . . . . .	49
4.8	Photo of the Raman beam modulation plate. . . . .	51
4.9	Raman beam delivery system . . . . .	52
4.10	Schematics of the experimental control system . . . . .	54
4.11	Schematics of repetition rate stabilization . . . . .	56
5.1	Schematics of applying a virtual single-qubit phase gate in quantum circuits . . . . .	60
5.2	Long-time Rabi oscillations using couter-propagating Raman transitions	61
5.3	Ramsey experiments . . . . .	62
5.4	Average gate fidelity comparison . . . . .	65
5.5	Characterization of $X(\pi/2)$ and $Y(\pi/2)$ gates using Gate Set Tomography . . . . .	66
5.6	Discrete FM pulse sequences and error analysis . . . . .	71
5.7	Infidelity of the entangled state generated by repeated application of MS gates in a two- and a four-ion chain . . . . .	74
5.8	Infidelity of the entangled state generated by repeated application of MS gates in a three-ion chain with an upgraded system . . . . .	78
5.9	Batch-robust FM MS gates performance . . . . .	83
5.10	Infidelity of Batch-robust FM MS gates in a two-ion chain . . . . .	84
6.1	Standard and Hermitian conjugated decompositions of CNOT gate with native trapped ion quantum operations . . . . .	89
6.2	Circuit diagrams for Hidden inverses experiment . . . . .	90
6.3	Multi-qubit parity controlled- $Z$ circuit simulated performance . . . . .	91
6.4	Hidden inverses experiment data and simulated final state fidelity . . . . .	95
6.5	SK1 two-qubit gates performance . . . . .	98
6.6	Randomized compiling protocol performance . . . . .	99

A.1	Ideal and reconstructed spacial probability of a two-dimensional motional entangling state . . . . .	112
B.1	Phase control scheme using RFSoC . . . . .	115

# Acknowledgements

Happy ions are all alike; every unhappy ion is unhappy in its own way. “Tortured” by unhappy ions in various ways from time to time, I still have enjoyed my life in graduate school because of the supports and the kindness from friends and faculty. The following perfunctory expressions of gratitude are never adequate for thanking their generosity with time and ideas.

I owe special debts to my advisor Ken Brown who has been supportive and helpful since I joined the team. I’m always amazed by Ken’s breadth of knowledge. From ion-trapping to quantum error correction, Ken is the one who can speak with both sides. Because of the diversity, discussing with Ken often provides me with new perspectives. Ken is also the master of balancing guidance and freedom. I would like to thank Ken for allowing me to explore topics that seemed not relevant to lab work at all, inspiring me with his science insights and enthusiasm, and not filing lawsuits against me for modifying equipment in destructive ways.

I would also like to thank my second advisor, Jungsang Kim, for providing me with the opportunity to join Team Red Chamber. Jungsang’s spirit of keeping pursuing perfection has influenced my way of thinking about quantum engineering.

I want to thank all Brown Lab and MIST Lab experimentalists. I’m fortunate enough to be surrounded by the greatest in the field. I appreciate the guidance from experienced research scientists including Kisra Egodapitiya, Jyothi Saraladevi, Geert Vrijzen, Lu Qi, Volkan Inlek, Mark Kuzyk, and Junki Kim. Thanks to Chao Fang,

Gloria Jia, Tripp Spivey, Ke Sun, Yuhi Aikyo, George Schwartz, Ely Novakoski, Jacob Whitlow, Pheobe Chen, Evan Reed, Brad Bondurant, and Leon Riesebos for comforting unhappy ions and celebrating for happy ones together with me in the lab. Rick Shu, Stephen Crain, and Ye Wang deserve a special mention. They are the post-docs with whom I worked closely and from whom I have learned the most.

I appreciate the conversations with Muyuan Li, Dripto Debroy, Michael Newman, and Natalie Brown, making quantum error correction theory less intimidating. Thanks to James Leung, Swarnadeep Majumder, Mingyu Kang, and Catherine Liang for their excellent theory work supporting the experiments. I'm grateful to Shilin Huang for having many enjoyable and productive discussions with me on various aspects of quantum computing.

I would like to thank our collaborators in Chris Monroe's group: Marko Cetina, Michael Goldman, Drew Risinger, etc, for their generous help and fruitful discussions.

I would like to thank my roommate Long Gong who cooks delicious Hunan pork stir-fry. We had a great time driving his unbreakable 1999 Camry.

I want to thank my parents Xinrong Zhang and Yarong Tian, for supporting me to study abroad, especially during the COVID-19 pandemic.

Finally, the tremendous thanks to my wife, Ellen, for providing me with unconditional support and love and proudly introducing me as a quantum computing scientist to all her friends. Under the pressure of pursuing her doctorate in geochemistry, Ellen is willing to listen to my jibber-jabber about atomic physics. Even the "atom"s she is interested in are diatoms.

# 1

## Introduction

Increasing computational power has benefited our lives from every perspective in the past decades and enabled breakthroughs in science and engineering. Theoretically, the modern computer is a specific example of a Turing machine. At its core, it uses transistors to manipulate numbers represented in base-2 or equivalently as series of on and off components. Guided by Moore’s law, the transistor density has doubled approximately every two years for half a century. The exponential scaling law has brought us nanometer-scale bits and gigahertz clock speeds in the second decade of the 21st century. At the same time, we are approaching the end of Moore’s law since when the scale of bits reduces to the size of a few atoms, and quantum mechanics replaces classical physics as the dominant principle. Therefore, if this trend continuous, we are likely to see a “diminishing marginal utility” as transistors continue to reduce in size.

Additionally, there are still a large number of problems that remain unsolvable for classical computers within a reasonable time. Certain problems that are intractable for classical computers, in areas like optimization, quantum chemistry, biomedical, and cryptography, attract a lot of interest from researchers across the world. As

a straightforward example, simulating the dynamics of a single two-level quantum system, such as interactions between electrons and atomic nucleus, can be done quickly with current classical computers. However, once the number of particles increases, the computational complexity of the system grows exponentially. Beyond just dozens of particles, it is already too difficult to solve via classical simulation, let alone a practical problem such as a complex molecular structure simulation. For example, even with the best supercomputer in the world, one cannot accurately simulate the dynamics of an average-sized protein molecule that contains hundreds of atoms.

Fortunately, every coin has two sides. The complexity of systems with quantum properties provides a tool to solve some complex problems. In the early 1980s, Richard Feynman and others proposed the idea that an arbitrary system could be simulated by a well-control complex quantum system [1], which is now referred to as a universal quantum computer. Later, David Deutsch, Richard Jozsa, Lov Grover, Peter Shor, and others developed algorithms that take advantage of quantum properties [2, 3, 4]. Peter Shor and Andrew Steane proposed quantum error correction theory simultaneously [5, 6]. With the pioneering work above, quantum computing has been drawing more interest from academia and industry since the 1990s.

## 1.1 Quantum Computing Overview

The key distinctions of quantum computing with regard to classical computing are quantum *superposition* and quantum *entanglement*. To understand the difference, a fundamental concept, *quantum bit* or *qubit*, is introduced.

The qubit's classical counterpart, the bit, has two possible states, either 0 or 1. However, a qubit can also end up in a state other than  $|0\rangle$  and  $|1\rangle$ . It is called

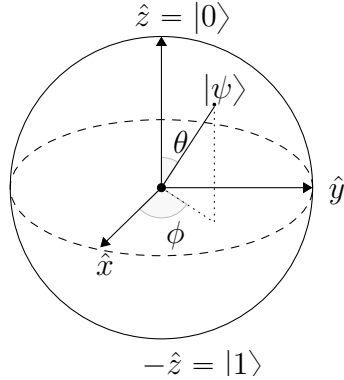


FIGURE 1.1: A qubit state  $|\psi\rangle$  represented in a Bloch sphere.

superposition, which is a linear combination of states with complex coefficients:

$$|\psi\rangle = \alpha|0\rangle + \beta|1\rangle$$

where  $\alpha$  and  $\beta$  are complex numbers.  $|0\rangle$  and  $|1\rangle$  define a computational basis which is called  $Z$  basis. When we measure the qubit we find it in state 0 with probability  $|\alpha|^2$ , or in state 1 with probability  $|\beta|^2$ . Usually, we normalize the state  $|\psi\rangle$  so that  $|\alpha|^2 + |\beta|^2 = 1$ . We can also choose a different basis to represent a quantum state. For example, the two orthogonal  $X$  basis states are  $|+\rangle = \frac{|0\rangle+|1\rangle}{\sqrt{2}}$  and  $|-\rangle = \frac{|0\rangle-|1\rangle}{\sqrt{2}}$ , and the two orthogonal  $Y$  basis states are  $|i\rangle = \frac{|0\rangle+i|1\rangle}{\sqrt{2}}$  and  $|-i\rangle = \frac{|0\rangle-i|1\rangle}{\sqrt{2}}$ . Considering the normalization condition, we can rewrite the quantum state as:

$$|\psi\rangle = \cos\frac{\theta}{2}|0\rangle + e^{i\phi}\sin\frac{\theta}{2}|1\rangle$$

which can be visualized in a *Bloch sphere* in Fig. 1.1.

The most important entangling state is the *Bell state*. For example, we have a state  $|\psi\rangle$  defined as:

$$|\psi\rangle = \frac{|00\rangle + |11\rangle}{\sqrt{2}}. \quad (1.1)$$

Its fascinating property appears after the measurement on one of the two qubits. If we measure the first qubit, we will obtain result 0 or result 1 each with a 50%

probability, and the two-qubit system will stay in a post-measurement state  $|00\rangle$  and  $|11\rangle$ , respectively. The measurement result of the second qubit is always identical to the first qubit's. Such property is a critical pillar in quantum teleportation and quantum algorithms.

In order to perform quantum computation, we need an architecture or computing routine called the *quantum circuit*. It has two basic elements, qubits and *quantum gates*. Quantum gates represent the manipulation of the qubits. In order to do arbitrary operations in the  $2^N$  dimension Hilbert space, we can choose a set of universal quantum gates. A typical choice contains single-qubit rotations, phase shift operations, and a two-qubit entanglement gate. Every physical platform has a different native universal gate set. A quantum circuit is imply the application of a sequence of quantum gates on the qubits. Therefore, the requirements for high-performance quantum circuits can be broken into three parts: 1. High-performance qubits; 2. High fidelity quantum gates; and 3. Circuit-level optimization. These requirements guide the research presented in this thesis.

Since the 1990s, various quantum computing platforms have been developing, and they all have their strength and weakness. In this thesis, I will be focusing on trapped atomic ions, which are one of the leading qubit platforms for realizing a quantum computer.

## 1.2 Quantum Computing with Trapped Ions

To defend the claim that trapped atomic ions are one of the most promising approaches to universal quantum computing, we compare ion trap quantum computers to the five requirements for quantum computers defined by David DiVincenzo in 2000 [7].

- *A scalable physical system with well-characterized qubits*

- *The ability to initialize the state of the qubits to a certain state*
- *Long coherence time*
- *A universal set of quantum gates*
- *The ability to measure the qubit state*

Trapped atomic ions fulfill all five requirements with outstanding gate and measurement fidelities and naturally identical qubits [8]. Comparing to another relatively mature quantum computing platform, superconducting circuits, trapped atomic ions have an advantage in quality of qubit operations and coherence time, and superconducting circuits have implemented larger universal systems [8, 9, 10, 11].

Being one of the two most mature quantum computing platforms, trapped atomic ions still face several problems. High-fidelity qubit operations in a large-scale trapped ion platform remain a challenge. The bottleneck of qubit operations in any platform is usually the entangling gates. Although trapped atomic ions hold the record of the highest fidelity for entangling gates in the year 2021 [12, 13, 14], the best fidelities are not always implemented in a scalable fashion. Most of the high fidelity records are achieved in a two-ion chain without individually addressing single qubits. The recent demonstration of the trapped-ion quantum charge-coupled device (QCCD) proposal reveals the possibility to use ion number  $N = 2$  chain to conduct universal quantum computing [15]; however, the field continues to debate the optimal length of the ion chain [16]. It is beneficial to explore the possibility of performing high fidelity operations in a  $N > 2$  ion chain, and it requires a system with the ability to individually address qubits.

Quantum systems are vulnerable to noises of different kinds, which lead to a wide variety of errors. According to the frequency spectrum of the noise, the error can be divided into coherent error (slow) and stochastic error (fast). In the case of trapped

ions, careful system calibration can reduce the coherent error to such a low level that we can hardly measure it. However, inevitable slow drifts of the environment require constant recalibration, limiting the quantum circuits' depth and performance and the duty-cycle of computation. The coherent error can often be suppressed by clever control, which improves the circuit performance for a small cost. Stochastic error, on the other hand, is trickier. It can only be suppressed by dedicated engineering and fault-tolerant quantum error correction [17].

The theme of this thesis is our contribution to improving gate and circuit performance in ion chains, with the ultimate goal of improving the performance of quantum circuits in a trapped-ion quantum computer.

### 1.3 Thesis Overview

In this thesis, I describe the basics of ion trap quantum computing and then my own work on understanding noise sources and improving ion trap performance. Chapter 2 discusses atomic ion qubit candidate selection, qubit preparation, and qubit measurement. Models of the gates belonging to the universal quantum gate set in our trapped-ion quantum computing platform are introduced in Chapter 3. With the knowledge of the experimental requirements, Chapter 4 presents the hardware and control system of the experimental setup. Characterization of the single-qubit and two-qubit gates performance in experiments are introduced in Chapter 5. Chapter 6 includes the circuit compilation technique that suppresses coherent errors.

## 2

### A Hyperfine Qubit

High-quality qubits are the first requirement for high-performance quantum circuits. In the context of trapped atomic ions, there are a few popular candidates, such as  $\text{Be}^+$ ,  $\text{Mg}^+$ ,  $\text{Ca}^+$ ,  $\text{Sr}^+$ ,  $\text{Ba}^+$ ,  $\text{Yb}^+$ , etc. [8]. These elements share a common point: they are all alkaline-earth-like atoms, which means the neutral atoms have two outer electrons. After ionizing one of the outer electrons, the ion behaves like a hydrogen atom. The relatively simple energy level structures are quantum control friendly.

Another thing we need to consider when we pick the physical qubit candidate is how to encode the qubit states in the energy levels of an atomic ion. Obviously, an ultra-stable two-level system is an excellent choice to encode qubit state  $|0\rangle$  and  $|1\rangle$ . At the moment, the most accurate tool for timekeeping is an atomic clock which takes advantage of the stable hyperfine splitting of the ground state. The hyperfine splitting of the ground state arises only from the Fermi contact interaction between the electron and nuclear spin. Therefore, the interaction is first-order insensitive to any external electric or magnetic field perturbations. Encoding the qubit states in the hyperfine splitting is a popular choice in the trapped-ion community. We choose an isotope with a half nuclear spin so that it has hyperfine structures.

Other than hyperfine qubits, Zeeman qubits are usually encoded in ground state Zeeman splitting, and optical qubits, which are usually encoded in the  $S \leftrightarrow D$  transition, are also popular candidates for quantum computing.

## 2.1 Hyperfine Qubit

In our system, we trap  $^{171}\text{Yb}^+$  ions as our hyperfine qubits. Pioneer work on trapping and manipulating  $^{171}\text{Yb}^+$  has been conducted over a decade [18]. We have a great foundation to start from, and our work shown in this chapter further polishes the quantum control protocol. The qubit states  $|0\rangle$  and  $|1\rangle$  are encoded in the hyperfine structure of the  $^2S_{1/2}$  ground state, where  $|0\rangle = |F = 0, m_F = 0\rangle$  and  $|1\rangle = |F = 1, m_F = 0\rangle$  are separated by  $12.642812118566 \text{ GHz} + 310.8(B^2) \text{ Hz}$ . The detailed energy structures can be found in Fig. 2.1.

The transition frequency between the qubit states is in the microwave frequency range. Therefore, we can drive the transitions by broadcasting resonant microwaves. Fig. 2.2 represents the frequency spectrum of two microwave transitions. The peak on the left is the carrier transition which is between  $|F = 0, m_F = 0\rangle$  and  $|F = 1, m_F = 0\rangle$ . The peak on the right corresponds to the Zeeman transition between  $|F = 0, m_F = 0\rangle$  and  $|F = 0, m_F = 1\rangle$ . The experiment data shows that in our system. the Zeeman splitting between  $|F = 0, m_F = 0\rangle$  and  $|F = 0, m_F = 1\rangle$  is around 7.286 MHz which infers a  $\sim 5.2 \text{ G}$  magnetic field at the ion location. Using the calculated strength of the magnetic field, we can predict the carrier transition frequency to be

$$12.642812118566 \text{ GHz} + 310.8(5.2^2) \text{ Hz} \approx 12.64282 \text{ GHz},$$

which agrees with the measured carrier frequency.

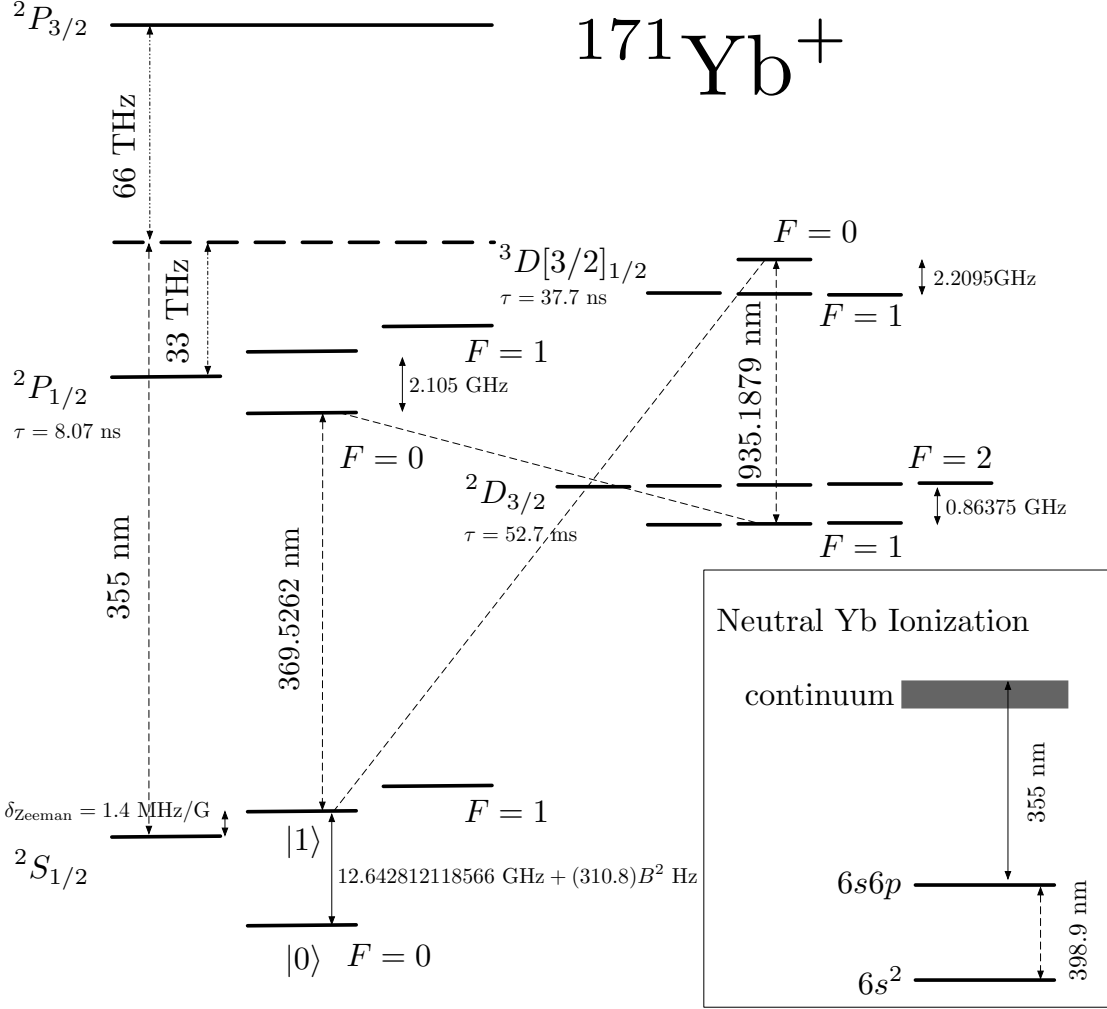


FIGURE 2.1: Relevant energy levels of  $^{171}\text{Yb}^+$  ions in quantum computing experiments. Inset shows the ionization route where 398.9 nm and 355 nm beams are used to ionize one of the two outer electrons.

## 2.2 Ion Loading: Ionization and Doppler Cooling

The ions can be trapped in a harmonic potential well because they are charged particles. The method to construct the potential will be discussed later in this chapter. Suppose we have the harmonic potential and hot Yb atoms at the trapping location. We need to ionize the neutral atoms and cool down the ions to lower the kinetic energy than the trapping potential depth. We use a 398.9 nm laser beam and a 355 nm laser beam to perform the ionization, which is a two-photon process. At

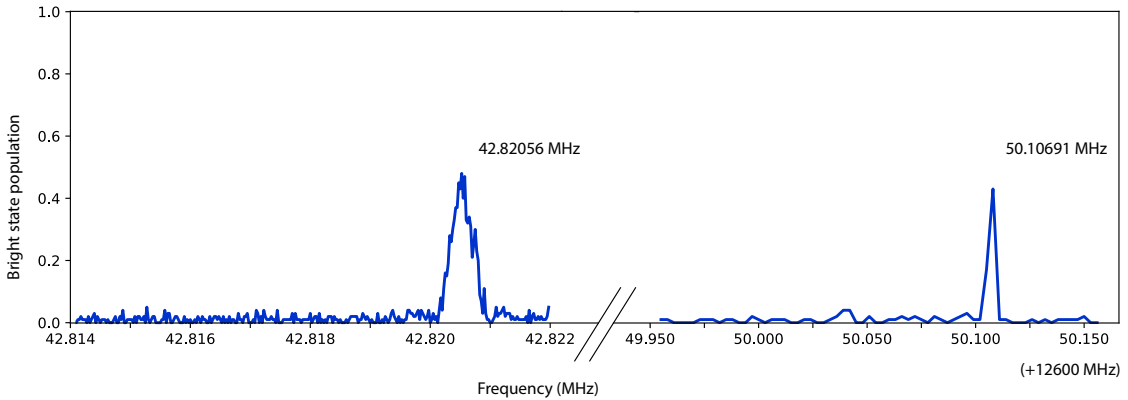


FIGURE 2.2: Microwave transition spectrum. The left peak corresponds to  $|0\rangle \leftrightarrow |1\rangle$  carrier transition. The right peak corresponds to  $|0\rangle \leftrightarrow |F = 1, m_F = 1\rangle$  Zeeman transition.

the same time, we illuminate the ions with a 369 nm laser beam to apply Doppler cooling.

The inset of Fig. 2.1 shows the ionization scheme for isotope  $^{171}\text{Yb}$ . First, the 398.9 nm laser beam brings the atom from the ground state  $6s^2$  to the excited state  $6s6p$ . Then any laser beam whose wavelength is shorter than 393 nm can cover the gap between  $6s6p$  to continuum. In theory, 398.9 nm beam and 369 nm beam are able to ionize the neutral atoms. In practice, the 369 nm beam, which is used mainly for Doppler cooling, has limited beam intensity at the trapping location. We can increase the intensity of the 369 nm beam; however, the large intensity reduces the Doppler cooling effect. Another more convenient way to go is using a 355 nm pulse laser beam. We use the pulse laser for operations relevant to Raman transitions, which require relatively large power. Also, 355 nm is a wavelength where we can obtain almost “infinite” power from commercial laser devices. Therefore, the ionization scheme in our system includes a 398.9 nm continuous wave laser from Toptica<sup>1</sup>, which drives the  $6s^2 \leftrightarrow 6s6p$  transition, and a 355 nm pulse laser from Coherent<sup>2</sup>, which close

---

<sup>1</sup> Toptica DL 100 399 nm, 0.1 mW at the trapping location

<sup>2</sup> Coherent Paladin Compact 355-4000, 40 mW at the trapping location

the gap between  $6s6p$  to continuum. As a reference, in order to obtain the isotope  $^{171}\text{Yb}^+$ , the measured frequency of 398.9 nm laser beam from the wavelength meter<sup>3</sup> is 751.527600 THz.

In experiments, we have two methods to produce neutral Ytterbium atoms. Method 1 is using a tube-shaped oven that contains Ytterbium metal pieces. We heat the oven and evaporate neutral Ytterbium atoms to the trapping location. Method 2 is ablating Ytterbium metal pieces with an IR pulsed laser to produced neutral atoms.

We use a 369 nm laser<sup>4</sup> beam which are red-detuned from the  $|^2S_{1/2}, F = 1\rangle \leftrightarrow |^2P_{1/2}, F = 0\rangle$  and  $|^2S_{1/2}, F = 0\rangle \leftrightarrow |^2P_{1/2}, F = 1\rangle$  transitions. The zeroth-order 369 nm laser beam is locked to the transition  $|^2S_{1/2}, F = 1\rangle \leftrightarrow |^2P_{1/2}, F = 0\rangle$  (15 to 20 MHz red-detuned), and a 14.7 GHz sideband is applied to the beam with an EOM<sup>5</sup> to drive the  $|^2S_{1/2}, F = 0\rangle \leftrightarrow |^2P_{1/2}, F = 1\rangle$  transition. The red-detuned 369 nm photons scatter off the ions which are moving towards the beam source and on average dissipate the kinetic energy of ions. The final Doppler cooling temperature is limited by the frequency uncertainty and the recoil limit. The final cooling temperature can be estimated from the velocity distribution and is given by

$$T_{Doppler} = \frac{\hbar\gamma}{2k_B}, \quad (2.1)$$

where  $k_B$  is the Boltzmann constant. Also, The temperature limit due to the recoil effect is given by

$$T_{recoil} = \frac{\hbar^2 k^2}{2Mk_B}, \quad (2.2)$$

where  $M$  is the mass of the atom. Typically, recoil temperature is lower than the Doppler temperature. To maximize the cooling efficiency, the Doppler cooling beam

---

<sup>3</sup> HighFinesse Wavelength Meter WS Ultimate

<sup>4</sup> MogLabs 369 nm diode laser

<sup>5</sup> Qubig Free-space EOM PM - Yb+14.7

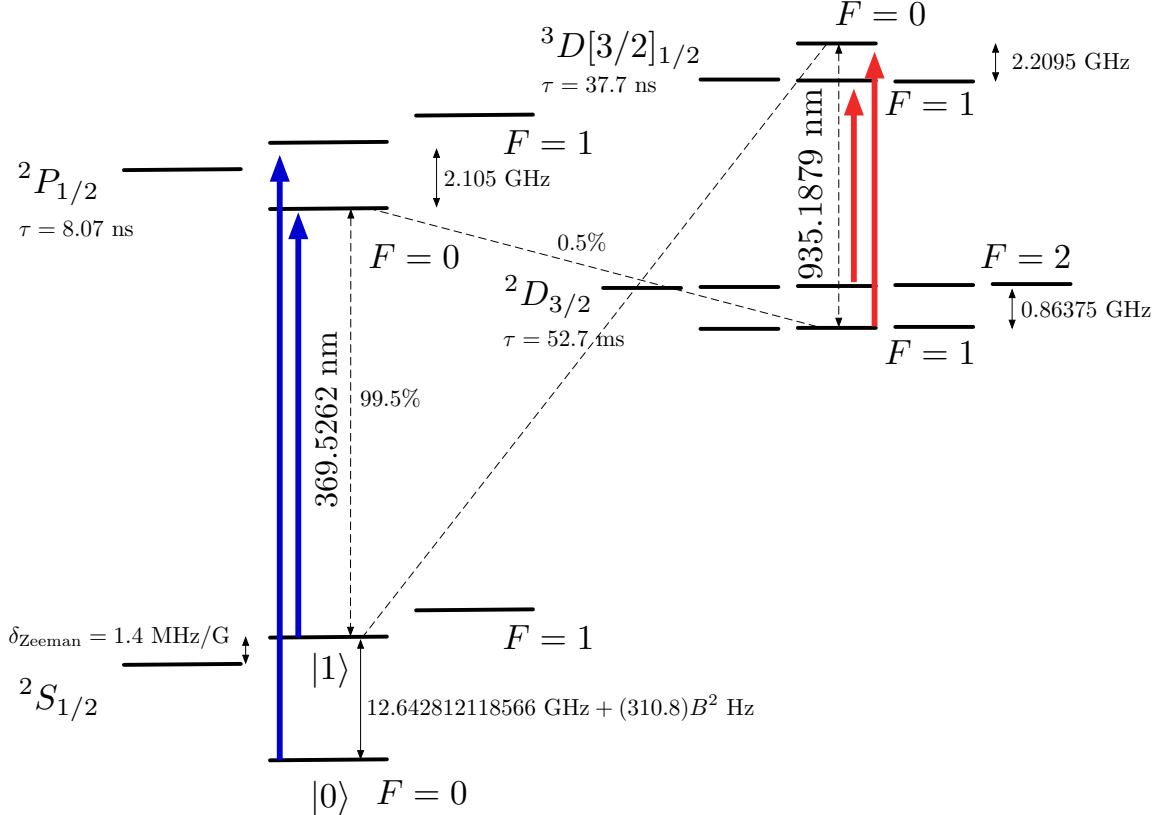


FIGURE 2.3: Relevant transitions in Doppler cooling procedure. A 369 nm laser with 14.7 GHz sidebands and a 935 nm laser with 3.1 GHz sidebands are involved.

intensity is below the saturation intensity  $I_{sat} = \frac{\pi hc}{3\lambda^3\gamma}$ , where  $\gamma = 2\pi \times 19.6$  MHz is the natural linewidth of the S to P transition, and the frequency of the cooling beam is about half of the natural linewidth  $\gamma$ . The atom can hop to the  $^2D_{3/2}$  state with a small probability, and we can bring it back to the cooling cycle by applying 935 nm laser<sup>6</sup> beam with 3.1 GHz sidebands which are added by a fiber EOM<sup>7</sup>.

Fig. 2.3 presents the details of the energy levels and the laser beams which we use in the Doppler cooling procedure. As a reference, the resonant frequency of 369 nm is 811.288800 THz reading from the lab wavelength meter. The frequency of the 935 nm laser is read as 320.569540 THz. In the experiment, we find that the transverse

<sup>6</sup> Toptica DL 100 935 nm

<sup>7</sup> iXblue NIR-MPX800-LN-10-P-P-FA-FA

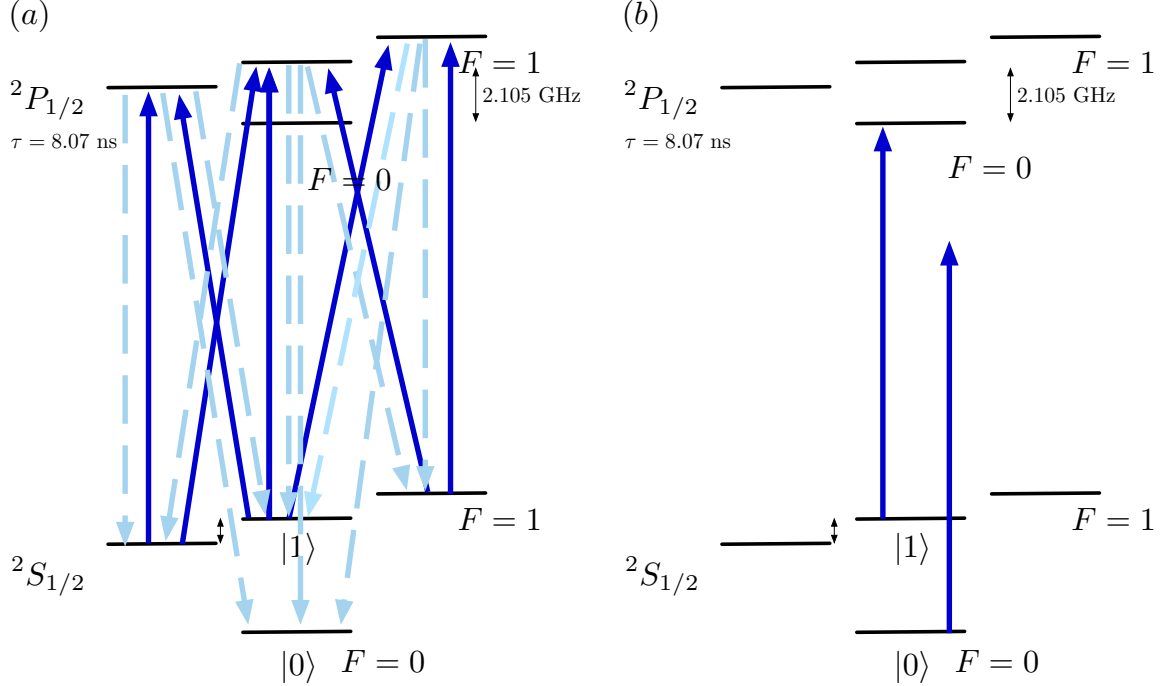


FIGURE 2.4: Relevant energy level diagram for optical pumping and detection. (a) Relevant transitions for optical pumping. Solid blue arrows represent the transition we drive with a pumping laser beam. The light sky blue dashed arrows show the possible spontaneous emissions. (b) Population in  $|1\rangle$  can be excited to  $^2P_{1/2} F = 0$  state. It emits ion fluorescence at a high rate because of the 8.07 ns lifetime. Population in  $|0\rangle$  cannot be excited because the 12.6 GHz detuning is much larger than the 20 MHz natural linewidth. A portion of the fluorescence photons is collected by either a camera or PMT.

motional mode temperature after Doppler cooling can be as low as 5 to 8 phonon at a motional frequency around 2.5 MHz. We note that the cooling process cannot sustain when an external magnetic field absents [19], so we have a 5.2 G magnetic field at the trapping location generated by several permanent magnets.

When cooling beyond the Doppler limit is required, we have two “sub-Doppler cooling” methods , sideband resolved Raman cooling and electromagnetically-induced transparency (EIT) cooling, available in our system.

## 2.3 State Initialization and Detection

States of ion qubits are initialized to  $|0\rangle$  by optical pumping. The resonant 369 nm beam with 2.1 GHz sidebands<sup>8</sup> drives transitions between the  $F = 1$  S manifold and the  $F = 1$  P manifold. The  $F = 1$  P manifold has a probability of decaying to qubit state  $|0\rangle$  or  $F = 1$  S manifold. Any population in state  $|0\rangle$  is settled here since the laser is 12.6 GHz off-resonant from any possible transition. The process will keep going until all population is settled in  $|0\rangle$  state. Fig. 2.4(a) shows the relevant transitions we drive in optical pumping. In the experiment, we turn on the transition for 15  $\mu$ s. We note that the 2.1 GHz signal we added to the EOM should be limited in power. Driving the EOM with high power results in drifting beam polarization after the free-space EOM. Depending on how one designs the 369 nm laser modulation optics, drifting beam polarization will reduce Doppler cooling efficiency or detection efficiency.

State detection uses the standard state-dependent ion fluorescence techniques. We take advantage of the short P state lifetime. The detection beam is resonant with the  $|1\rangle$  and  $F = 0$  P state. If the qubit is in  $|0\rangle$  state, the detection beam will not scatter the ion due to the 12.6 GHz frequency detuning. If the ion is in  $|1\rangle$  state, detection photons will be scattered and collected by a camera or photomultiplier tube (PMT). The state preparation and measurement (SPAM) error in our system is about 99.93%.

## 2.4 EIT Cooling

As mentioned previously, electromagnetically induced transparency (EIT) cooling is one ground-state cooling technique that can go beyond the Doppler cooling limit. EIT cooling was initially proposed two decades ago [20]. To understand the cooling

---

<sup>8</sup> Added by Qubig Free-space EOM PM - Yb+\_2.1

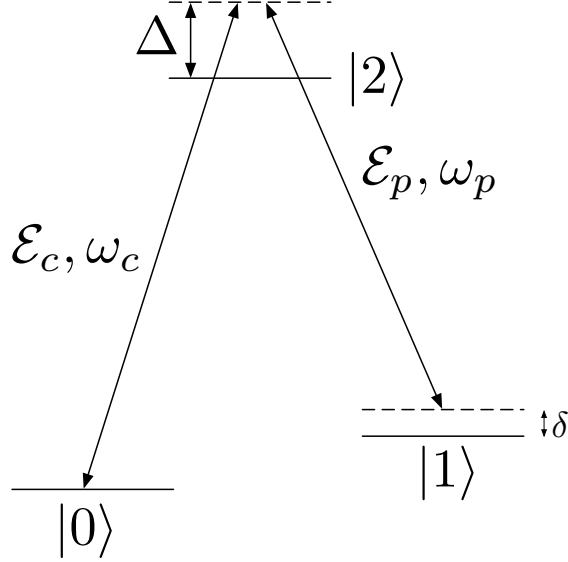


FIGURE 2.5: A general three-level structure driven by two fields.

technique, we review the EIT phenomena here. We can obtain the basic idea from its name. The atomic medium that was opaque to a certain color becomes transparent due to EM induction (illumination by carefully calibrated laser beams).

EIT phenomena happen in a three-level system driven by two EM fields which are shown in Fig. 2.5. Let us consider the case that we have a strong coupling beam  $\mathcal{E}_c$  and a weak probe beam  $\mathcal{E}_p$ . We call a beam a strong coupling beam when its Rabi frequency is either larger or comparable to the spontaneous emission rate of state  $|2\rangle$ . The weak probe beam has a Rabi frequency that is much smaller than the spontaneous emission rate. The coupling beam is resonant with the transition frequency of  $|0\rangle \leftrightarrow |2\rangle$ . So we have  $\omega_c = \omega_2 - \omega_1$  and  $\Delta = 0$ . When we scan the driving frequency  $\omega_p$  of the probe beam, we obtain an absorption spectrum. With the absence of the coupling beam, a peak appears at  $\delta = 0$  on the absorption spectrum. It is when the probe beam is resonant with  $|1\rangle \leftrightarrow |2\rangle$  transition. At the moment, the atomic medium is opaque to the probe beam.

However, when the strong coupling beam is turned on, the excited state  $|2\rangle$  is dressed. Let us consider the subsystem which only involves state  $|0\rangle$ , state  $|2\rangle$ , and

the coupling beam. The simplification is valid because the probe beam is so weak that its influence on the energy structure is negligible. Therefore, the system can be described by the Jaynes-Cummings model. The Hamiltonian is written as

$$\hat{H}(t) = \frac{\hbar}{2}\Omega_c e^{-i\omega_c t} |2\rangle\langle 0| + h.c. \quad (2.3)$$

where  $\Omega_c$  is the Rabi frequency of the coupling beam. Solving the Schrödinger equation and we can obtain two stationary states:

$$|\psi_+\rangle = e^{i\Omega_c t/2} \frac{|0\rangle + |2\rangle}{\sqrt{2}}, \quad (2.4)$$

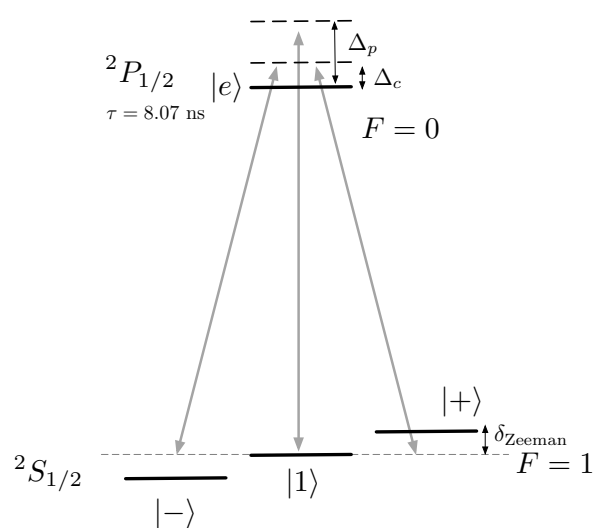
$$|\psi_-\rangle = e^{-i\Omega_c t/2} \frac{|0\rangle - |2\rangle}{\sqrt{2}}. \quad (2.5)$$

The corresponding eigenvalues are  $\hbar\omega_2 \pm \hbar\Omega_c/2$ . From another perspective, we say that  $|2\rangle$  is dressed into two separated energy levels by the coupling beam. The two energy levels are separated by  $\hbar\Omega_c$ , so we can tune the energy levels by adjusting the coupling beam intensity. With the presence of the coupling beam, the peak in the absorption spectrum splits into two peaks. The transitions  $|1\rangle \leftrightarrow |\psi_+\rangle$  and  $|1\rangle \leftrightarrow |\psi_-\rangle$  destructively interfere at where  $|1\rangle \leftrightarrow |2\rangle$  used to be. The scattering rate drops to exactly zero. Therefore, if the probe beam is resonant to  $|1\rangle \leftrightarrow |2\rangle$ , the atomic medium becomes transparent to it because of the interaction with the coupling beam. That is why the phenomena is called electromagnetically-induced transparency.

The basic idea of cooling by taking advantage of EIT is using the Fano-shaped absorption spectrum to enhance the red sideband transition while simultaneously suppressing the carrier and blue sideband transitions. Because of the short  $^2P_{1/2}$  state lifetime, 8.07 ns, the system keeps losing phonons, so the temperature of the corresponding motional modes is cooled down.

In the case of  $^{171}\text{Yb}^+$ , it is more complicated than a  $\Lambda$  system— three ground states

(a)



(b)

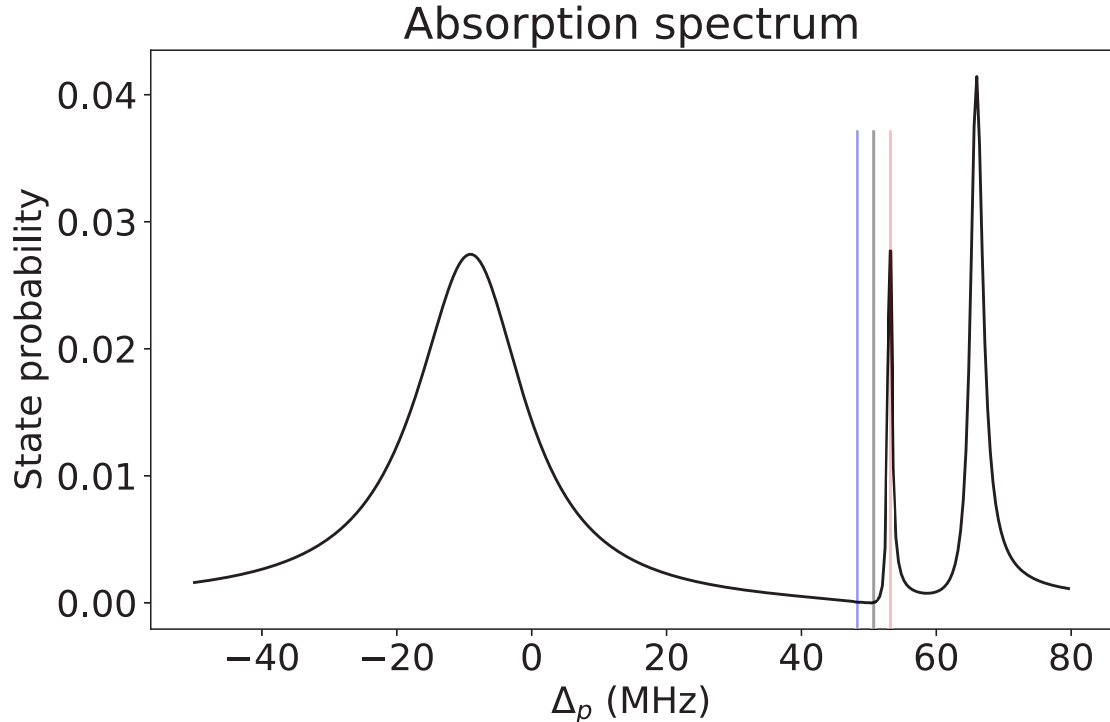


FIGURE 2.6: (a) Relevant energy levels involved in  $^{171}\text{Yb}^+$  EIT cooling. The probe beam is blue detuned  $\Delta_p$  from  $|1\rangle \leftrightarrow |e\rangle$  resonance. The coupling beam is blue detuned  $\Delta_c$  from resonance. (b) The simulated absorption spectrum. The light red, black, and blue vertical lines correspond to red sideband, carrier, and blue sideband transition frequencies. The red sideband transition is enhanced, while the carrier and blue sideband transition are suppressed.

and one excited state are involved [21] as shown in Fig. 2.6 (a). Three stationary states are generated in this case, as showed in Fig. 2.6 (b). The system can be described by an effective Hamiltonian:

$$\hat{H}/\hbar = \begin{pmatrix} 0 & \frac{\Omega_{\sigma-}}{2}e^{-i\vec{k}_c\cdot\vec{r}} & -\frac{\Omega_{\pi}}{2}e^{-i\vec{k}_p\cdot\vec{r}} & \frac{\Omega_{\sigma+}}{2}e^{-i\vec{k}_c\cdot\vec{r}} \\ \frac{\Omega_{\sigma-}}{2}e^{i\vec{k}_c\cdot\vec{r}} & \Delta_c + \delta_{\text{Zeeman}} & 0 & 0 \\ -\frac{\Omega_{\pi}}{2}e^{i\vec{k}_p\cdot\vec{r}} & 0 & \Delta_p & 0 \\ \frac{\Omega_{\sigma+}}{2}e^{i\vec{k}_c\cdot\vec{r}} & 0 & 0 & \Delta_c - \delta_{\text{Zeeman}} \end{pmatrix} + \nu a^\dagger a, \quad (2.6)$$

where  $\Delta_j$  is the detuning from  $|e\rangle$  and  $\vec{k}_j$  is the wave vector for beam  $j$ .  $j = c$  corresponds to the two coupling beams with  $\sigma_\pm$  polarizations, and  $j = p$  corresponds to the probe beam with a  $\pi$  polarization. The absorption spectrum and cooling limit can be obtained by solving the master equation with Lindblad terms:

$$\frac{d\hat{\rho}}{dt} = -i[\hat{H}, \hat{\rho}] + \mathcal{L}\hat{\rho}, \quad (2.7)$$

where  $\mathcal{L}$  is the Lindblad operator corresponding to the three spontaneous decay channels. The emission rates to the three ground states are all  $\Gamma/3$ . Therefore,  $c_i = \sqrt{\Gamma/3}|i\rangle\langle e|$ ,  $i \in \{+, 0, -\}$ ,  $\Gamma \approx 2\pi \times 20$  MHz. Further details can be found in Ref. [21].

In experiments, the probe beam (EIT 1) is  $2\pi \times 44$  MHz blue-detuned from resonance of transition  $|1\rangle \leftrightarrow |^2P_{1/2}, F = 0\rangle$ . The coupling beam (EIT 2) is  $2\pi \times 37.68$  MHz blue-detuned from resonance. The two beams have a counter-propagating configuration. The details of the optical setup are discussed in Sec. 4.2.1. Because of the wide width of the absorption peak, we can cool multiple motional modes of the ion chain simultaneously. In our setup, after 1 ms Doppler cooling and  $250 \mu\text{s}$  EIT cooling, a two-ion chain transverse COM mode and tilt mode can be cooled under 0.3 quanta/s. The ability to cool multiple modes in a two-ion chain and a ten-ion chain ( $n = 10$ ) is shown in the red sideband spectrum in Fig. 2.7. After EIT cooling, the

red sideband transition peaks are well suppressed, meaning that the corresponding motional modes are in states closed to motional ground state.

## 2.5 Surface Electrode Ion Traps

In this section, we can for the time forget about all properties of  $^{171}\text{Yb}^+$  ions but the fact that they are positively charged particles. Coulomb interaction allows ions to be trapped in a “bowl”-shaped electric potential. The trapping potential is a combination of static direct current electric field and radio frequency oscillating electric fields. The radiofrequency oscillating field applies a ponderomotive force on ions and creates a pseudo-potential as,

$$\psi_p = \frac{v_{\text{rf}}^2 q^2}{4m\omega_{\text{rf}}^2} E^2, \quad (2.8)$$

where  $v_{\text{rf}}$  is the amplitude of voltage on RF electrodes,  $q$  and  $m$  is the charge and the mass of an ion,  $\omega_{\text{rf}}$  is the driving frequency of RF field, and  $E$  is the static electric field generated by RF electrodes when they are applied with 1 V DC voltage.

Fig. 2.8 shows the surface electrode ion trap used in our experiments, the Phoenix trap fabricated by Sandia National Laboratories [22]. It contains a large RF electrode that generates the ponderomotive pseudo-potential. It also has 94 independent DC electrodes to make further potential adjustments. Like Phoenix traps’ predecessor High Optical Access Trap 2 (HOA 2) [23], they all have a slot at the center region of the trap for optical accessing.

In experiments, ions are trapped  $\sim 70 \mu\text{m}$  above the trap surface. Applying 250 V, 46.3415 MHz RF signal, the trap features 2.5 MHz z-direction radial trap frequency.

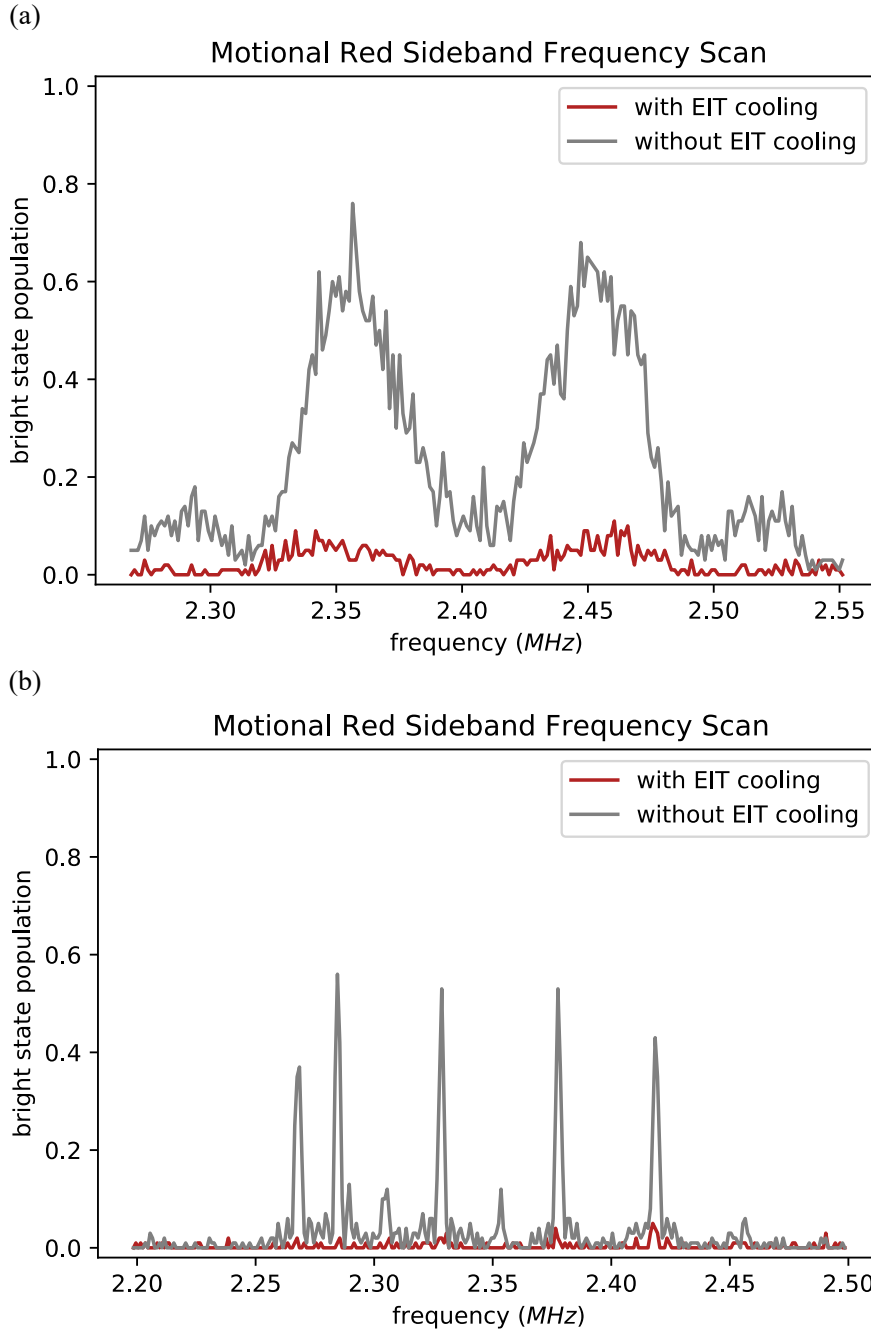


FIGURE 2.7: Experimental red sideband absorption spectrum before and after EIT cooling. Gray curves represent the red sideband spectrum after 1 ms Doppler cooling. Red curves represent the red sideband spectrum after 1 ms Doppler cooling and then 250  $\mu$ s EIT cooling. (a) The top figure shows the spectra in a two-ion chain. The temperature after EIT cooling is around 0.23 quanta/s. (b) The bottom one shows the spectra in a ten-ion chain.

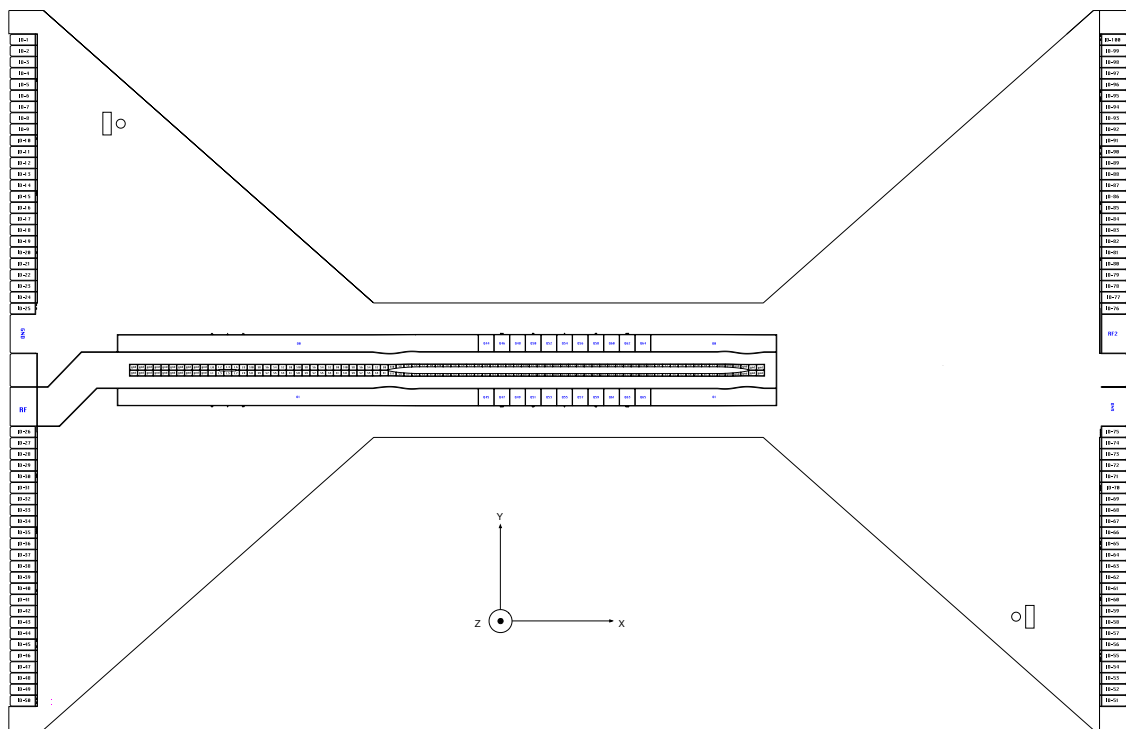
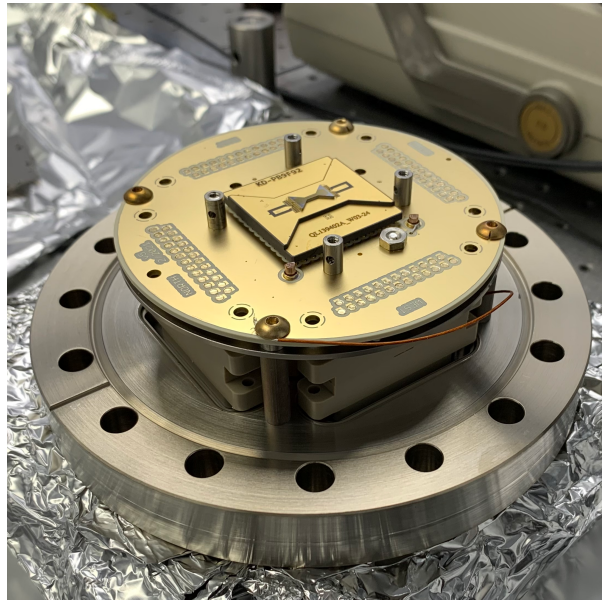


FIGURE 2.8: On the top is a picture of the Phoenix surface trap mounted on the back flange of the ultra-high vacuum chamber. The bottom figure is the electrode layout of the Phoenix trap. It has 94 independent DC electrodes and 1 RF electrode. It has a slot at the center region, which allows optical access from top and bottom.

## 2.6 Radial Motional Modes

Conventionally, the axial phonon modes are used for entanglement gate operations in ion traps. The axial modes are more stable than radial modes because it is defined by DC voltages, while radial modes depend on RF voltages. RF signal is more vulnerable to noises than DC signals. In fact, most of the high fidelity entanglement gates are implemented by using axial modes [13, 14, 12].

However, axial phonon modes do not meet the requirement of conducting quantum computing operations in a long ion chain. First, when ion number  $N > 2$ , individual qubit addressing is required. It is natural to have tightly focused laser beams propagate along the ion chain's radial directions and simultaneously aim at separate target ion qubits. Second, as the ion number grows, the axial confinement decreases. Thus, the axial mode frequencies decrease at the same time. The gates using axial motional mode are more sensitive to ion heating and thermal motion. Therefore, we apply the entanglement gates with radial motional modes in this thesis [24].

Here we review the basics of phonon modes [25]. Assume we have an  $N$ -ion chain along the x-direction. The potential of the ion chain generated by external trapping potential and internal ion-ion Coulomb interactions is written as

$$V = \frac{1}{2}m \sum_{i=1}^N (\omega_x^2 x_i^2 + \omega_y^2 y_i^2 + \omega_z^2 z_i^2) + \sum_{i < j} \frac{e^2}{\sqrt{(x_i - x_j)^2 + (y_i - y_j)^2 + (z_i - z_j)^2}}, \quad (2.9)$$

where  $m$  is the mass of an ion,  $\omega_\xi, \xi \in \{x, y, z\}$  are the center-of-mass trap frequency along  $\xi$ -direction. In the case of a ion chain, the equilibrium position of ion  $i$  is  $(\bar{x}_i, \bar{y}_i, \bar{z}_i) = (\bar{x}_i, 0, 0)$ . We denote  $q_{i,\xi} = \xi_i - \bar{\xi}_i$ ,  $i \in \{1, \dots, N\}$ ,  $\xi \in \{x, y, z\}$ . When the ion chain is sufficiently cooled, the displacements from the equilibrium positions are

small. We can rewrite the potential up to a second-order approximation:

$$V \approx \frac{1}{2} \sum_{\xi', \xi, i, j} q_{i, \xi} q_{j, \xi'} \left( \frac{\partial^2 V}{\partial q_{i, \xi} \partial q_{j, \xi'}} \right) = \frac{1}{2} m \omega_x^2 \sum_{\xi, i, j} A_{ij}^\xi q_{i, \xi} q_{j, \xi}, \quad (2.10)$$

where

$$A_{ij}^\xi = \begin{cases} \beta_\xi^2 + \frac{2e^2}{m\omega_x^2} \sum_{p=1, p \neq i}^N a_\xi / |\bar{x}_i - \bar{x}_p|^3 & (i = j) \\ -\frac{2e^2}{m\omega_x^2} a_\xi / |\bar{x}_i - \bar{x}_j|^3 & (i \neq j) \end{cases}, \quad (2.11)$$

$\beta_\xi = \omega_\xi / \omega_x$ ,  $a_\xi = 1$  for  $\xi = y, z$ , and  $a_\xi = -2$  for  $\xi = x$ .

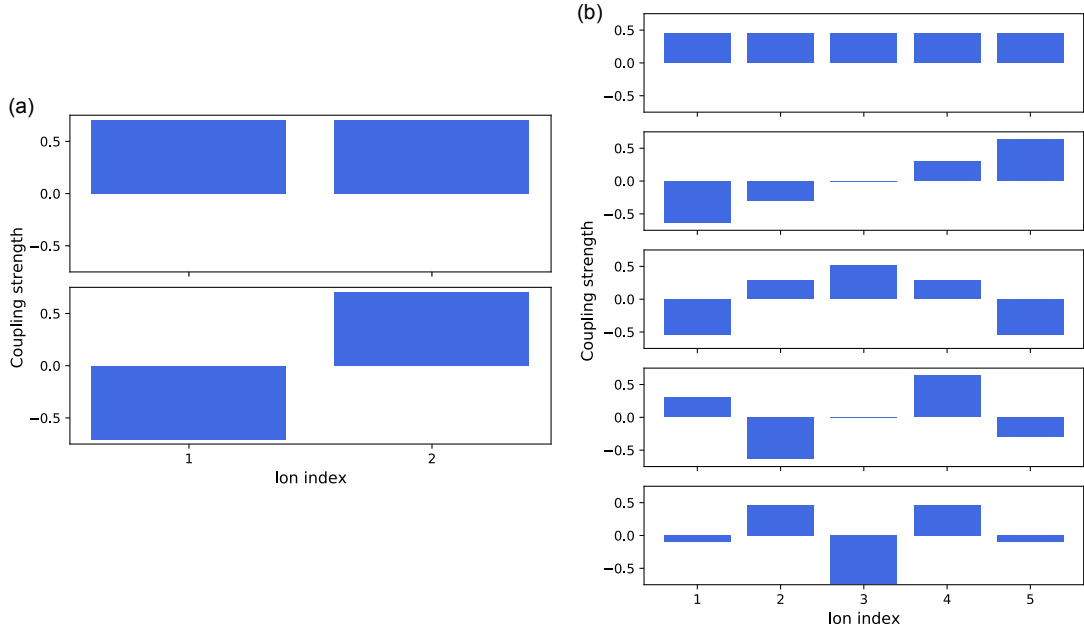


FIGURE 2.9: Motional modes coupling strength for a (a) two-ion and (b) five-ion chain. In each column, from top to bottom, the subplots present the coupling strengths from the highest frequency COM mode to the lowest frequency zig-zag mode.

In our system, we implement entanglement gates using radial phonon modes along z-direction, so we care about matrix  $A_{ij}^z$ . The  $i$ -th eigenvector of matrix  $A_{ij}^z$  represents the corresponding coupling strength for each ion in the chain to the  $i$ -th

motional mode along the z-direction. Fig. 2.9 shows two examples of radial motional modes coupling strength in a two-ion and five-ion chain, assuming the trap potential is harmonic.

Besides being used as the medium of qubit-qubit interaction, motional states in trapped-ion platform are ideal for bosonic system quantum simulation. A method that determines the density matrix of two motional modes entangling states is introduced in Appdenix A.

# 3

## Quantum Gates with Trapped Ions

Quantum gates transform the states of qubits. Just like their classical counterpart, they include single-qubit gates and multi-qubit gates. Single-qubit gates are unitary operators which can be represented in  $2 \times 2$  matrices. Similarly, a  $N$ -qubit entangling gate can be represented by a  $2^N \times 2^N$  matrix. Quantum gates do include not only discrete bit flips but also continuous rotations and phase flips. High-quality quantum gates are the foundation for high-performance quantum circuits. Therefore, it is necessary to understand the details before implementing the gates in the laboratory. This chapter will review the physics principles of the qubit operations and the quantum gate set we choose for our trapped-ion quantum computer. Finally, we introduce a simulation tool for entangling gate performance analysis.

In experiments, single-qubit gates are realized by driving Rabi oscillations between the qubit states. In the case of  $^{171}\text{Yb}^+$ ion qubits, the qubit states are separated by 12.6 GHz showing in Fig. 2.1. Therefore, the Rabi oscillations are driven by a resonant microwave field or two laser fields via Raman transitions. Arbitrary single-qubit gates can be implemented by controlling Rabi frequencies, rotation axis, and gate duration. However, we prefer applying arbitrary rotation angles (except

for  $\pi/2$ ) along  $Z$  axis than applying them by controlling gate duration and Rabi frequency. This is because we realize an arbitrary  $RZ(\theta)$  rotation in a virtual way by accumulating a  $-\theta$  phase in the following gate operations on the target qubit. The virtual  $RZ$  operations have higher fidelity than  $RX$  and  $RY$  operations, especially when the rotation angle is small. In practice, we have a single-qubit gate set consisting of  $RX(\pi/2)$  rotation and arbitrary  $RZ(\theta)$  rotations to realize an arbitrary single-qubit gate. In order to individually address ions, we realize the  $RX$  operations by Raman transitions.

### 3.1 Raman Transitions

Raman transitions take place in a three-level system illustrated in Fig. 2.5. We consider the case of the three-level  $\Lambda$  system in a harmonic potential. Like the situation of EIT cooling, a coupling field  $\omega_c$  and a probe field  $\omega_p$  are applied to the system. We note that we only use the name “coupling” and “probe” here to distinguish them, but we do not require that the coupling field is stronger than the probe field. The system can be described by Hamiltonian  $H = H_0 + H_I$ .  $H_0$  consists of an atom term and a motion term.

$$H_0^{(\text{atom})} = \hbar\omega_{10}|1\rangle\langle 1| + \hbar\omega_{20}|2\rangle\langle 2|, \quad (3.1)$$

$$H_0^{(\text{motion})} = \hbar\nu \left( a^\dagger a + \frac{1}{2} \right), \quad (3.2)$$

$$H_0 = H_0^{(\text{atom})} + H_0^{(\text{motion})}, \quad (3.3)$$

where we set the energy of  $|0\rangle$  as zero.  $\nu$  is the frequency of the harmonic potential. Creation and annihilation operators of phonon are represented by  $a^\dagger$  and  $a$ , respectively. The Interaction between the three-level system (the ion) and laser fields are electric dipole interaction. Thus,  $H_I = -q\vec{E}\cdot\hat{\mathbf{r}} = H_I^{(c)} + H_I^{(p)}$  includes the interactions

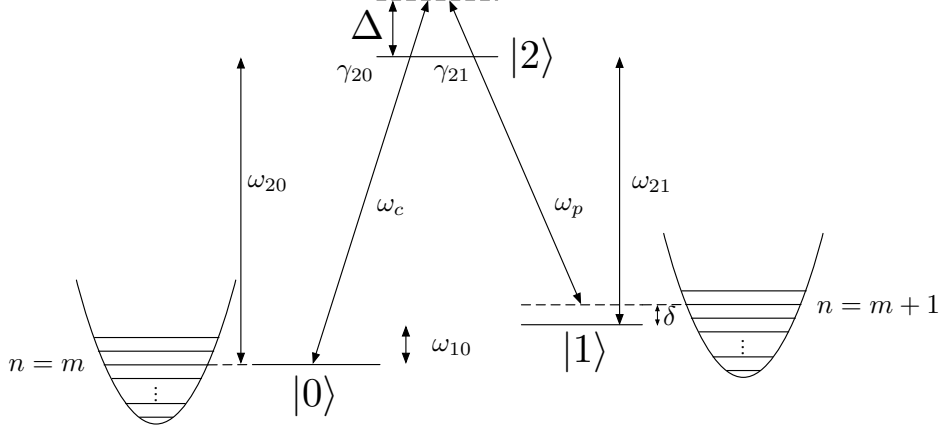


FIGURE 3.1: A three-level system. Two laser fields are applied, marked as coupling field  $\omega_c$  and probe field  $\omega_p$ . Single-photon detuning is represented by  $\Delta$ . Two-photon detuning is represented by  $\delta$ . The spontaneous emission rate from  $|2\rangle$  to  $|i\rangle$  is  $\gamma_{2i}$  ( $i = 0, 1$ ). The parabolas on the sides of the figure illustrate the motional states of the ion, and  $n$  is the motional state quantum number. It describes a blue sideband transition between  $|0, m\rangle \leftrightarrow |1, m+1\rangle$ .

with coupling and probe fields. Therefore, two terms of the interaction Hamiltonian are written as:

$$H_I^{(c)} = (\hbar\Omega_c |0\rangle\langle 2| + \hbar\Omega_c^* |2\rangle\langle 0|) \cos(\omega_c t - \vec{k}_c \cdot \vec{x} + \phi_c), \quad (3.4)$$

$$H_I^{(p)} = (\hbar\Omega_p |1\rangle\langle 2| + \hbar\Omega_p^* |2\rangle\langle 1|) \cos(\omega_p t - \vec{k}_p \cdot \vec{x} + \phi_p), \quad (3.5)$$

where  $\hbar\Omega_c = -qE_0^{(c)}\hat{\epsilon}_c \cdot \hat{r}d_{02}$  and  $\hbar\Omega_p = -qE_0^{(p)}\hat{\epsilon}_p \cdot \hat{r}d_{12}$ .

For convenience, we treat the whole Hamiltonian in a rotating frame corresponding to

$$H_D = \hbar(\omega_c - \omega_p) |1\rangle\langle 1| + \hbar\omega_c |2\rangle\langle 2| = \hbar(\omega_{10} + \delta) |1\rangle\langle 1| + \hbar\omega_c |2\rangle\langle 2|. \quad (3.6)$$

Since the commutation relation  $[H_0, H_D] = 0$ , the effective Hamiltonian in the new

Table 3.1: Approximate magnitudes of the angular frequencies appearing in Fig. 3.1 when the atomic mediate is  $^{171}\text{Yb}^+$ . We use 355 nm ( $\sim 844$  THz) pulsed laser beams for Raman transitions.

$\omega_{20}, \omega_{21}$	$2\pi \cdot 844$ THz
$\Delta$	$2\pi \cdot 33$ THz
$\omega_{10}$	$2\pi \cdot 12.64$ GHz
$\Omega_c, \Omega_p$	$2\pi \cdot 3.6$ GHz
$\gamma_{20}, \gamma_{21}$	$2\pi \cdot 10$ MHz
$\nu$	$2\pi \cdot 2$ MHz
$\delta$	$< 2\pi \cdot 10$ kHz

frame is

$$\begin{aligned} \tilde{H} &= H_0 - H_D + e^{iH_D t/\hbar} H_I e^{-iH_D t/\hbar} \\ &= -\hbar\delta |1\rangle\langle 1| - \hbar\Delta |2\rangle\langle 2| + \hbar\nu \left( a^\dagger a + \frac{1}{2} \right) + \tilde{H}_I^{(c)} + \tilde{H}_I^{(p)}, \end{aligned} \quad (3.7)$$

$$\tilde{H}_I^{(c)} = \hbar\Omega_c e^{-i\omega_c t} |0\rangle\langle 2| \cos(\omega_c t - \vec{k}_c \cdot \vec{x} + \phi_c) + h.c. \quad (3.8)$$

$$\tilde{H}_I^{(p)} = \hbar\Omega_p e^{-i\omega_p t} |1\rangle\langle 2| \cos(\omega_p t - \vec{k}_p \cdot \vec{x} + \phi_p) + h.c. \quad (3.9)$$

Now we consider the realistic parameters in  $^{171}\text{Yb}^+$  ion. The magnitudes of the frequencies showing in Fig. 3.1 can be found in Table. 3.1. The frequencies have the relation of  $\omega_{20} \approx \omega_{21} \gg \Delta \gg \omega_{10} \gg \gamma_{20}, \gamma_{21} > \nu > \delta$ . Because of the relation, we can apply rotating wave approximation (RWA) to Eq. 3.8 and Eq. 3.9. When solving the time evolution,  $\int e^{i\omega t} = -\frac{ie^{i\omega t}}{\omega}$  is evaluated from  $t = 0$  to  $t = \tau$ . When  $\omega$  is large then contribution can be safely neglected. Therefore, we neglect the fast oscillating terms in Eq. 3.8 and Eq. 3.9, and we obtain the following interaction Hamiltonians:

$$\tilde{H}_I^{(c)} \approx \frac{\hbar}{2} \Omega_c e^{i(-\vec{k}_c \cdot \vec{x} + \phi_c)} |0\rangle\langle 2| + h.c., \quad (3.10)$$

$$\tilde{H}_I^{(p)} \approx \frac{\hbar}{2} \Omega_p e^{i(-\vec{k}_p \cdot \vec{x} + \phi_p)} |1\rangle\langle 2| + h.c.. \quad (3.11)$$

The ion is trapped in a harmonic potential, and we can quantize its motion by replace  $\vec{k}_c \cdot \vec{x}$  with  $\eta_c(a^\dagger + a)$ , where  $\eta_c \equiv \vec{k}_c \cdot \hat{\varepsilon}_x \sqrt{\frac{\hbar}{2m\nu}}$ . Similarly, we have  $\vec{k}_p \cdot \vec{x} =$

$\eta_p(a^\dagger + a)$ .  $\eta_c$  ( $\eta_p$ ) is the Lamb-Dicke parameter and measures the interaction strength between spin states and motional states. In the following derivations, we assume that the interaction is sufficiently small so that any transitions that change the motional quantum number by more than one are strongly suppressed. It is also known as the Lamb-Dicke regime. Within this regime, we can neglect the higher order terms in the Taylor expansion of  $e^{\pm i\eta_c(a^\dagger + a)}$  and  $e^{\pm i\eta_p(a^\dagger + a)}$ .

The spontaneous emissions from  $|2\rangle$  to  $|0\rangle$  and  $|1\rangle$  are depicted by two collapse operators:

$$L_{20} = \sqrt{\gamma_{20}} |0\rangle\langle 2|, \quad (3.12)$$

$$L_{21} = \sqrt{\gamma_{21}} |1\rangle\langle 2|. \quad (3.13)$$

We note that these collapse operators in the rotating frame with respect to  $H_D$  are  $\tilde{L}_{20} = e^{-i\omega_c t} \sqrt{\gamma_{20}} |0\rangle\langle 2|$  and  $\tilde{L}_{21} = e^{-i\omega_p t} \sqrt{\gamma_{21}} |1\rangle\langle 2|$ . Since  $e^{-i\omega_c t}$  and  $e^{-i\omega_p t}$  are scalars, they commute with any operator. Conveniently, we can just use  $L_{20}$  and  $L_{21}$  without modifying the master equation.

Now we have all required components of the master equation, which is presented in Eq. 3.14. In theory, we can numerically simulate the Raman transitions by solving the master equation. However, the computation is relatively slow and unstable when  $\Delta/\Omega_{c,p}$  is too large, which is the situation  $^{171}\text{Yb}^+$  faces. Not only to effectively simulate the system but also to obtain a physics intuition about Raman transitions, further analysis is needed. We will treat the Hamiltonian slightly differently when we consider the single-qubit rotations and the entangling gates, respectively.

$$\dot{\tilde{\rho}} = -\frac{i}{\hbar} [\tilde{H}, \tilde{\rho}] + \sum_i \left[ L_i \tilde{\rho} L_i^\dagger - \frac{1}{2} (L^\dagger L \tilde{\rho} + \tilde{\rho} L^\dagger L) \right] \quad (3.14)$$

### 3.2 Single-Qubit Gates

We focus on spin state transformations in single-qubit rotations, while ideally, motional state transitions are not evoked. Within the Lamb-Dicke regime, where  $\eta^2(2n + 1) \ll 1$ , the interaction Hamiltonians are written as:

$$\tilde{H}_I^{(c)} \approx \frac{\hbar}{2} \Omega_c e^{i\phi_c} |0\rangle\langle 2| + h.c., \quad (3.15)$$

$$\tilde{H}_I^{(p)} \approx \frac{\hbar}{2} \Omega_p e^{i\phi_p} |1\rangle\langle 2| + h.c.. \quad (3.16)$$

Only the zeroth-order corresponding to the carrier transition is reserved, and higher orders which involve motional states are neglected. This treatment is accurate when the motional states are not driven at all ( $\eta_c - \eta_p = 0$ ). This condition can be realized when we apply two co-propagating Raman beams. This treatment is still a good approximation even if the net Lamb-Dicke parameter is not zero, as long as we choose proper  $\delta$  to drive the carrier transition resonantly while motional sideband transitions are far-detuned ( $\sim 2\pi \cdot 2$  MHz away). The second condition corresponds to a counter-propagating Raman transition. No matter which condition we use, the effective Hamiltonian is always written as:

$$\tilde{H} = -\hbar\delta |1\rangle\langle 1| - \hbar\Delta|2\rangle\langle 2| + \left[ \frac{\hbar}{2} \Omega_c e^{i\phi_c} |0\rangle\langle 2| + \frac{\hbar}{2} \Omega_p e^{i\phi_p} |1\rangle\langle 2| + h.c. \right]. \quad (3.17)$$

Substitute this for the effective Hamiltonian in Eq. 3.14. We obtain nine equa-

tions, and each of them represents an entry for the  $3 \times 3$  matrix:

$$\dot{\tilde{\rho}}_{00} = -\frac{i}{2}(\Omega_c e^{i\phi_c} \tilde{\rho}_{20} - \Omega_c^* e^{-i\phi_c} \tilde{\rho}_{02}) + \gamma_{20} \tilde{\rho}_{22} \quad (3.18)$$

$$\dot{\tilde{\rho}}_{11} = -\frac{i}{2}(\Omega_p e^{i\phi_p} \tilde{\rho}_{21} - \Omega_p^* e^{-i\phi_p} \tilde{\rho}_{12}) + \gamma_{21} \tilde{\rho}_{22} \quad (3.19)$$

$$\dot{\tilde{\rho}}_{22} = -\dot{\tilde{\rho}}_{00} - \dot{\tilde{\rho}}_{11} \quad (3.20)$$

$$\dot{\tilde{\rho}}_{01} = \dot{\tilde{\rho}}_{10}^* = -i\delta \tilde{\rho}_{01} - \frac{i}{2}(\Omega_c e^{i\phi_c} \tilde{\rho}_{21} - \Omega_p^* e^{-i\phi_p} \tilde{\rho}_{02}) \quad (3.21)$$

$$\dot{\tilde{\rho}}_{02} = \dot{\tilde{\rho}}_{20}^* = -i\Delta \tilde{\rho}_{02} - \frac{i}{2}(\Omega_c e^{i\phi_c} (\tilde{\rho}_{22} - \tilde{\rho}_{00}) - \Omega_p e^{i\phi_p} \tilde{\rho}_{01}) - \frac{\gamma_{20} + \gamma_{21}}{2} \tilde{\rho}_{02} \quad (3.22)$$

$$\dot{\tilde{\rho}}_{12} = \dot{\tilde{\rho}}_{21}^* = -i(\Delta - \delta) \tilde{\rho}_{12} - \frac{i}{2}(\Omega_p e^{i\phi_p} (\tilde{\rho}_{22} - \tilde{\rho}_{11}) - \Omega_c e^{i\phi_c} \tilde{\rho}_{10}) - \frac{\gamma_{20} + \gamma_{21}}{2} \tilde{\rho}_{12} \quad (3.23)$$

In the context of a  $^{171}\text{Yb}^+$  ion, we know from Table 3.1 that the single-photon detuning  $\Delta \approx 2\pi \cdot 33$  THz is much larger than the Rabi frequencies of coupling and probe beam. Moreover,  $^2P_{1/2}$  of  $^{171}\text{Yb}^+ (|2\rangle)$  has a  $2\pi \cdot 20$  MHz spontaneous emission rate, which keeps the population in  $|2\rangle$  at a level close to zero. Therefore, we make the approximation that  $\tilde{\rho}_{22} = 0$  and  $\dot{\tilde{\rho}}_{02} = \dot{\tilde{\rho}}_{20}^* = 0$ . This approximation basically neglects the  $|2\rangle$  state and reduces the system to a two-level one. After reorganization, the number of equations is reduced to four, and the equations only involve  $|0\rangle$  and  $|1\rangle$ :

$$\dot{\tilde{\rho}}_{00} = -\frac{i}{4\Delta} \Omega_p^* e^{-i\phi_p} \Omega_c e^{i\phi_c} \tilde{\rho}_{10} + \frac{i}{4\Delta} \Omega_p e^{i\phi_p} \Omega_c^* e^{-i\phi_c} \tilde{\rho}_{01}, \quad (3.24)$$

$$\dot{\tilde{\rho}}_{11} = \frac{i}{4\Delta} \Omega_p^* e^{-i\phi_p} \Omega_c e^{i\phi_c} \tilde{\rho}_{10} - \frac{i}{4\Delta} \Omega_p e^{i\phi_p} \Omega_c^* e^{-i\phi_c} \tilde{\rho}_{01} = -\dot{\tilde{\rho}}_{00}, \quad (3.25)$$

$$\dot{\tilde{\rho}}_{01} = -i\tilde{\rho}_{01} \left( \delta + \frac{|\Omega_c|^2 - |\Omega_p|^2}{4\Delta} \right) - \frac{i}{4\Delta} \Omega_p^* e^{-i\phi_p} \Omega_c e^{i\phi_c} (\tilde{\rho}_{11} - \tilde{\rho}_{00}) = \dot{\tilde{\rho}}_{10}^*. \quad (3.26)$$

The set of ordinary differential equations can be written in an effective form showing in Eq. 3.27 and 3.28. The effective form is the same as the driving Rabi

oscillations in a two-level system with one resonant field.

$$\tilde{H}_{\text{eff}} = \frac{\hbar}{2} \begin{pmatrix} 0 & \Omega \\ \Omega^* & -2\delta' \end{pmatrix}, \quad (3.27)$$

$$\dot{\tilde{\rho}}_{\text{eff}} = -\frac{i}{\hbar} [\tilde{H}_{\text{eff}}, \tilde{\rho}_{\text{eff}}]. \quad (3.28)$$

The effective Rabi frequency  $\Omega = \frac{\Omega_p^* \Omega_c e^{i(\phi_c - \phi_p)}}{2\Delta}$  includes the information of amplitude and phase. The effective two-photon detuning  $\delta' = \delta + \frac{|\Omega_c|^2 - |\Omega_p|^2}{4\Delta}$ .  $\frac{|\Omega_c|^2 - |\Omega_p|^2}{4\Delta}$  is the differential ac Stark shift.

In the context of  $^{171}\text{Yb}^+$ , the 12.6 GHz qubit state separation is considered as a quite large modulation for CW lasers. We can cover the 12.64 GHz gap with a high-frequency EOM, but the strength of the modulation sidebands is weak. In experiments, we use a pulsed laser to drive the Raman transitions [26]. For the pulsed laser beam, the electric field amplitude varies in time. In the frequency domain, each pulse is an optical frequency comb whose teeth are spaced by the repetition rate  $f_{\text{rep}} \approx 117.8$  MHz. The pulse width is so short that the bandwidth of the frequency comb is larger than the qubit transition. Pairs of teeth in two frequency combs whose center frequency is off by  $f_c - f_p < f_{\text{rep}}$  can resonantly drive the Raman transition when  $f_c - f_p + n f_{\text{rep}} = \omega_{10}/2\pi$ . The effective transition can be analyzed by adding up all frequency comb pairs. It will introduce a different Rabi frequency expression and a different Stark shift nulling condition. Further details can be found in Ref. [27]. However, the transition behaves similarly to the CW laser treatment in experiments once we calibrate the effective Rabi frequency and suppress the Stark shift. We note that we do not stabilize the center frequency of Raman beams, but we have to stabilize the repetition rate  $f_{\text{rep}}$ . Instead of applying direct stabilization on the repetition rate, we monitor the fluctuation of the rate and compensate for the frequency difference. Further details about the repetition rate stabilization are introduced in Sec. 4.4.

### 3.3 Mølmer Sørensen Gates

In a two-qubit entangling gate, the state of one qubit is controlled by the state of another one. For example, a Controlled-NOT gate is similar to XOR in classical binary logic. In ion qubits, Coulomb interaction serves as the shuttle to realize entanglement. Coulomb interaction is strong and long-range ( $\sim 1/R$ ). These advantages provide us with high connectivity in a long ion chain. However, the “long-range” and “always present” properties increase the quantum control difficulty and complexity when the number of qubits in a single chain increases.

Because of the presence of Coulomb interaction, the qubits in a chain of ions share motional states. As we discuss in Sec. 2.6, we use radial motional modes as the shuttle to implement entangling gates. The scheme we select for our native entangling gate is the Mølmer Sørensen (MS) gate [28, 29]. Since we use motional states to entangle qubits, motional state operators need to be included in the Hamiltonian. The interaction Hamiltonians are:

$$\tilde{H}_I^{(c)} = \frac{\hbar}{2} \Omega_c e^{i\phi_c} e^{-i\eta_c(a^\dagger + a)} |0\rangle\langle 2| + h.c. \quad (3.29)$$

$$\tilde{H}_I^{(p)} = \frac{\hbar}{2} \Omega_p e^{i\phi_p} e^{-i\eta_p(a^\dagger + a)} |1\rangle\langle 2| + h.c. \quad (3.30)$$

Unlike what we did in the previous section, here we undo the Taylor expansion for  $e^{-i\eta(a^\dagger + a)}$ , and we keep the  $\hbar\nu(a^\dagger a + \frac{1}{2})$  term in  $H_0$ . Following the same process as the previous section, we obtain a similar effective Hamiltonian:

$$\tilde{H}_{\text{eff}} = \frac{\hbar}{2} \begin{pmatrix} 0 & \Omega \\ \Omega^* & -2\delta' \end{pmatrix} + \hbar\nu \left( a^\dagger a + \frac{1}{2} \right), \quad (3.31)$$

where  $\Omega = \frac{\Omega_p^* \Omega_c e^{i(\phi_c - \phi_p)} e^{-i\eta_c(a^\dagger + a)} e^{i\eta_p(a^\dagger + a)}}{2\Delta} = \frac{\Omega_p^* \Omega_c e^{i(\phi_c - \phi_p)}}{2\Delta} e^{-i(\eta_c - \eta_p)(a^\dagger + a)}$ , and  $\delta' = \delta + \frac{|\Omega_c|^2 - |\Omega_p|^2}{4\Delta}$ .

Since we add a term in the “solvable” Hamiltonian  $H_0$ , it would be convenient to do another frame rotation:

$$H_{D,2} = -\hbar\delta' |1\rangle\langle 1| + \hbar\nu \left( a^\dagger a + \frac{1}{2} \right). \quad (3.32)$$

Recall the first frame rotation in Eq. 3.6, after the second rotation, the total frame rotating  $H_{D,\text{total}} = \hbar \left( \omega_{10} - \frac{|\Omega_c|^2 - |\Omega_p|^2}{4\Delta} \right) |1\rangle\langle 1| + \hbar\omega_c |2\rangle\langle 2| + \hbar\nu \left( a^\dagger a + \frac{1}{2} \right)$  is independent to  $\delta$ . This conclusion is a prerequisite for the derivation involving bi-chromatic field.

After rotating the frame, the effective Hamiltonian becomes:

$$\begin{aligned} \tilde{H}_{\text{eff}} &= e^{iH_{D,2}t/\hbar} \left[ \frac{\hbar}{2} \Omega^* |1\rangle\langle 0| + \frac{\hbar}{2} \Omega |0\rangle\langle 1| \right] e^{-iH_{D,2}t/\hbar} \\ &= \frac{\hbar}{2} \Omega_{\text{eff}} e^{i\phi_{\text{eff}}} e^{-i\eta_{\text{eff}}(e^{i\nu t} a^\dagger + e^{-i\nu t} a)} e^{i\delta' t} \hat{\sigma}_- + h.c., \end{aligned} \quad (3.33)$$

where  $\Omega_{\text{eff}} = \frac{\Omega_p^* \Omega_c}{2\Delta}$ ,  $\phi_{\text{eff}} = \phi_c - \phi_p$ , and  $\eta_{\text{eff}} = \eta_c - \eta_p$ . Within Lamb-Dicke regime,  $e^{-i\eta_{\text{eff}}(e^{i\nu t} a^\dagger + e^{-i\nu t} a)} \approx 1 - i\eta_{\text{eff}}(e^{i\nu t} a^\dagger + e^{-i\nu t} a)$ . Therefore, the effective Hamiltonian splits into three parts which correspond to carrier, red sideband, and blue sideband transitions, respectively:

$$\tilde{H}_{\text{eff}} = \frac{\hbar}{2} \Omega_{\text{eff}} e^{i\phi_{\text{eff}}} \hat{\sigma}_- (e^{i\delta' t} - i\eta_{\text{eff}} e^{i(\nu+\delta')t} a^\dagger - i\eta_{\text{eff}} e^{i(\delta'-\nu)t} a) + h.c.. \quad (3.34)$$

*Case 1: Red sideband transition.*  $|\delta'_r|, |\delta'_r - \nu| \gg |\delta'_r + \nu|$ . Carrier and blue sideband terms can be neglected in RWA. Thus, the effective red sideband Hamiltonian is written as:

$$\tilde{H}_{r,\text{eff}} = -i \frac{\hbar}{2} \eta_{\text{eff}} \Omega_{r,\text{eff}} e^{i\phi_{r,\text{eff}}} e^{i(\delta'_r + \nu)t} a^\dagger \hat{\sigma}_- + h.c. \quad (3.35)$$

*Case 2: Blue sideband transition.*  $|\delta'_b|, |\delta'_b + \nu| \gg |\delta'_b - \nu|$ . Carrier and red sideband terms can be neglected in RWA. Thus, the effective blue sideband Hamiltonian is

written as:

$$\tilde{H}_{b,\text{eff}} = -i\frac{\hbar}{2}\eta_{\text{eff}}\Omega_{b,\text{eff}}e^{i\phi_{b,\text{eff}}}e^{i(\delta'_b-\nu)t}a\hat{\sigma}_- + h.c. \quad (3.36)$$

The MS gate requires bi-chromatic fields illuminating on two ions that share motional states. The total Hamiltonian includes four terms: Red sideband transition and blue sideband transition on both ions. In an ideal MS Hamiltonian, the power of red and blue sideband transitions are balanced, and the driving frequency of the red and blue tones are symmetric about the carrier frequency.

$$\begin{aligned}\Omega &= \Omega_{r,\text{eff}} = \Omega_{b,\text{eff}} \\ \delta &= \delta'_b - \nu = -(\delta'_r + \nu)\end{aligned}$$

In general, we can control the frequency with higher accuracy than the amplitude in experiments. So the frequency symmetry is straightforward to be realized, while the two-tone power balancing is tricky. The power balance assumption is made in an early stage, and the following analysis is based on it. Therefore, we implement two-tone power balancing calibration in experiments to achieve high fidelity MS gates.

The absolute phase difference between ion one and ion two does not matter as long as they are coherent within the duration of the coherent operations. Without loss of generality, we can have:

$$\begin{aligned}\phi_{r,\text{eff}} &= \phi_{r,\text{eff}}^{(1)} = \phi_{r,\text{eff}}^{(2)}, \\ \phi_{b,\text{eff}} &= \phi_{b,\text{eff}}^{(1)} = \phi_{b,\text{eff}}^{(2)}.\end{aligned}$$

Therefore we have the effective Hamiltonian for the MS gate:

$$\tilde{H}_{\text{eff}} = \sum_{j=1}^2 -i\frac{\hbar\eta_{\text{eff}}^{(j)}\Omega^{(j)}}{2}[e^{i\phi_{r,\text{eff}}}e^{-i\delta t}a^\dagger\hat{\sigma}_-^{(j)} + e^{i\phi_{b,\text{eff}}}e^{i\delta t}a\hat{\sigma}_-^{(j)}] + h.c., \quad (3.37)$$

where index  $j$  denotes different ions. We note that when we implement frequency-modulated (FM) gate solutions, the derivation is also valid. In frequency modulated

gates,  $\delta$  varies during the pulse duration, and the optical phase is continuous. As we've discussed previously, the total frame rotating is independent to  $\delta$ , therefore we can substitute  $\delta t$  with  $\delta(t)t$  and compensate the phase of the blue and red tone to fulfill the optical phase continuity. We note that the phase compensation is automatically accomplished by DDS/RFSoc's phase accumulator in experiments, while in master equation simulation, we need to emulate a virtual phase accumulator. It is even more straightforward to express amplitude modulated (AM) and phase-modulated (PM) pulses by simply making  $\Omega^{(j)}$ ,  $\phi_{r,\text{eff}}$ , and  $\phi_{b,\text{eff}}$  time-dependent. Therefore, a more general effective Hamiltonian is written as:

$$\tilde{H}_{\text{eff}} = \sum_{j=1}^2 -i \frac{\hbar \eta_{\text{eff}}^{(j)} \Omega^{(j)}}{2} [e^{i\phi_{r,\text{eff}}(t)} e^{-i\delta(t)t} a^\dagger \hat{\sigma}_-^{(j)} + e^{i\phi_{b,\text{eff}}(t)} e^{i\delta(t)t} a \hat{\sigma}_-^{(j)}] + h.c.. \quad (3.38)$$

Reorganize the general effective Hamiltonian, and we can separate the spin and motion operators.

$$\tilde{H}_{\text{eff}} = \sum_{j=1}^2 -i \frac{\hbar \eta_{\text{eff}}^{(j)} \Omega^{(j)}}{2} (\hat{\sigma}_-^{(j)} e^{i\phi_s} - \hat{\sigma}_+^{(j)} e^{-i\phi_s}) (a^\dagger e^{-i\delta(t)t} e^{i\phi_m(t)} + a e^{i\delta(t)t} e^{-i\phi_m(t)}) \quad (3.39)$$

$$= \sum_{j=1}^2 -i \frac{\hbar \eta_{\text{eff}}^{(j)} \Omega^{(j)}}{2} \Sigma^{(j)} A(t) \quad (3.40)$$

where  $\phi_s = \frac{\phi_{r,\text{eff}}(t) + \phi_{b,\text{eff}}(t)}{2} \equiv \text{const}$  is the spin phase, and  $\phi_m(t) = \frac{\phi_{r,\text{eff}}(t) - \phi_{b,\text{eff}}(t)}{2}$  is the motion phase. The spin operator  $\Sigma^{(j)} = \hat{\sigma}_-^{(j)} e^{i\phi_s} - \hat{\sigma}_+^{(j)} e^{-i\phi_s}$ . The motion operator  $A(t) = a^\dagger e^{-i\delta(t)t} e^{i\phi_m(t)} + a e^{i\delta(t)t} e^{-i\phi_m(t)}$ .

The resulting time evolution unitary operator is obtained by Magnus expansion.

$$\begin{aligned} U(t) &= \exp(-i\tilde{H}_{\text{eff}}t/\hbar) \\ &= \exp\left(\sum_{k=1}^{\infty} M_k(t)\right) \end{aligned} \quad (3.41)$$

$$\begin{aligned}
M_1(t) &= -\frac{i}{\hbar} \int_0^t \tilde{H}_{\text{eff}}(\tau) d\tau \\
&= \sum_{j=1}^2 \Sigma^{(j)} \frac{\eta_{\text{eff}}^{(j)} \Omega^{(j)}}{2} (a^\dagger \alpha(t) + a \alpha^*(t))
\end{aligned} \tag{3.42}$$

$$\begin{aligned}
M_2(t) &= \frac{1}{2} \left( -\frac{i}{\hbar} \right)^2 \int_0^t \int_0^{t_1} [\tilde{H}_{\text{eff}}(t_1), \tilde{H}_{\text{eff}}(t_2)] dt_2 dt_1 \\
&= -i \frac{1}{\hbar^2} \int_0^t \int_0^{t_1} S^2 \sin(\theta(t_1) - \theta(t_2)) dt_2 dt_1
\end{aligned} \tag{3.43}$$

where  $\alpha(t) = \int_0^t \Omega^{(j)}(\tau) e^{i\phi_m(\tau)} e^{-i\delta(\tau)\tau} d\tau$ , and  $S = \sum_j -i \frac{\hbar \eta_{\text{eff}}^{(j)} \Omega^{(j)}(t)}{2} \Sigma^{(j)}$ . Because  $[\Sigma^{(i)}, \Sigma^{(i)}] = 0$  and  $[a, a^\dagger] = 1$ , the expansion terminates at the second term. Under the continuous optical phase condition, we can evaluate the phase term of the displacement operator argument  $\alpha(t)$ :

$$\begin{aligned}
\exp(i\phi_m(\tau)) \exp(-i\delta(\tau)\tau) &= \exp(i(\phi_m(\tau) - \delta(\tau)\tau)) \\
&= \exp(i(\int_0^t -\delta(\tau)d\tau) + \delta(t)t - \delta(t)t) \\
&= \exp(i \int_0^t -\delta(\tau)d\tau)
\end{aligned} \tag{3.44}$$

$$= \exp(i\theta(t)) \tag{3.45}$$

where  $\theta(t) = \int_0^t -\delta(\tau)d\tau$ . Further details about the phase continuity can be found in Appendix B.1.

The first-order term corresponds to a state-dependent displacement. At the end of the gate, the displacement returns to origin ideally. When we design MS gate pulse sequences, we can suppress the displacement at the end of the gate—minimizing  $|\alpha(T_{\text{gate}})|$ . In the experiments we will discuss in Chapter 5, we implement FM pulse sequences to achieve this goal.

The second-order term corresponds to a rotation along  $\hat{\sigma}_\phi^{(1)} \otimes \hat{\sigma}_\phi^{(2)}$  axis. When  $\phi_s = 0$ , the Hamiltonian represents a  $\hat{\sigma}_y^{(1)} \otimes \hat{\sigma}_y^{(2)}$  rotation. The global phase does not matter in quantum computing, and we normally call an MS gate an  $XX(\pi/4)$  gate. The rotation angle  $\pi/4$  is selected because the rotation creates a maximal entangling state or a Bell state between two qubits. This angle can be achieved by calibrating the amplitude  $\Omega$ .

In the previous analysis, we only consider one motional mode. Since  $M_2(t)$  is independent of motion operators, the contribution to the rotation angle from different motional modes commute. Therefore, we can sequentially calculate the evolution of different motional modes to avoid having an extremely large Hilbert space. This property makes pulse design for a longer ion chain possible and makes numerical simulating gate performance more efficient.

### 3.4 Modulated MS Gate Simulation

This section contains results from

Ye Wang, Stephen Crain, Chao Fang, **Bichen Zhang**, Shilin Huang, Qiyao Liang, Pak Hong Leung, Kenneth R. Brown, and Jungsang Kim, Phys. Rev. Lett. **125**, 150505 (2020) [30]

#### 3.4.1 Error model

The study of imperfections and error mechanisms in a modulated MS gate provides insights into whether the limitations are of fundamental nature, or technical challenges. We use Schrödinger equation simulation and the master equation simulation for the study of these error mechanisms. We use the Schrödinger equation to study coherent systematic errors without consideration of dissipation, e.g., detuning errors, drifts of laser intensity and calibration drifts. The Hamiltonian of the MS evolution

of the  $j$ th motional mode with no modulation is written as [28, 29, 31]

$$\hat{H}(t)_{j,MS} = \frac{i}{2} \sum_{n=1,2} \eta_j^{(n)} \hat{\sigma}_+^{(n)} \left( \Omega_r^{(n)} \hat{a}_j e^{i\phi_r - i\delta_{j,r}^{(n)} t} + \Omega_b^{(n)} \hat{a}_j^\dagger e^{i\phi_b - i\delta_{j,b}^{(n)} t} \right) + h.c. \quad (3.46)$$

where  $\Omega_r^{(1)}$ ,  $\Omega_b^{(1)}$ ,  $\Omega_r^{(2)}$  and  $\Omega_b^{(2)}$  are the Rabi frequencies of red and blue sideband transitions for the two target ions,  $\delta_{j,r}^{(1)}$ ,  $\delta_{j,b}^{(1)}$ ,  $\delta_{j,r}^{(2)}$ , and  $\delta_{j,b}^{(2)}$  are the detunings for the  $j$ th motional mode,  $\phi_r$  and  $\phi_b$  are the laser phases of the red and blue tone, respectively. With the expansion in Eq. 3.46, we can simulate number of error mechanisms: power imbalance on two target ions, power imbalance on red and blue tones, and detuning imbalance due to Stark shift. For the full MS evolution, the modes are sequentially simulated to minimize the computing resource. We only save the spin state result for the next round of simulation. The Hamiltonian of different modes commute when  $\Omega_r^{(1)} = \Omega_b^{(1)}$  and  $\Omega_r^{(2)} = \Omega_b^{(2)}$ , which is a reasonable assumption in the MS gate.

We sequentially simulate every segment to obtain the final state for the evolution of discrete segments in discrete modulated gates. While in a continuously modulated gate, we use Hamiltonian in Eq. 3.38.

We use a master equation [32] to simulate an open-quantum system considering multiple dissipative error mechanisms: motional heating, motional dephasing, and laser dephasing. The master equation is written in Lindblad form [33]

$$\frac{d\hat{\rho}}{dt} = \frac{1}{i\hbar} [\hat{H}, \hat{\rho}] + \sum_j \left( \hat{L}_j \hat{\rho} \hat{L}_j^\dagger - \frac{1}{2} \hat{L}_j^\dagger \hat{L}_j \hat{\rho} - \frac{1}{2} \hat{\rho} \hat{L}_j^\dagger \hat{L}_j \right),$$

where  $\rho$  is the density matrix of the system,  $H$  is the Hamiltonian of the MS gate,  $\hat{L}_j$  is the Lindblad operator for the  $j$ th decoherence process. The motional dephasing can be described by the Lindblad operator of the form  $\hat{L}_m = \sqrt{2/\tau_m} \hat{a}^\dagger \hat{a}$ , where  $\tau_m$  is the motional coherence time. The anomalous heating can be described by  $\hat{L}_+ = \sqrt{\Gamma} \hat{a}^\dagger$

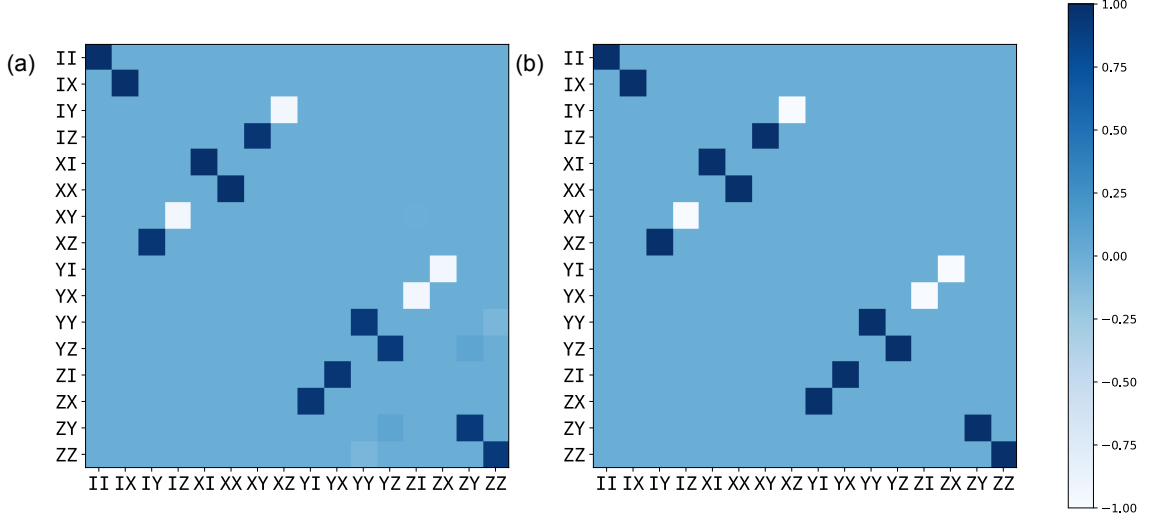


FIGURE 3.2: Pauli transfer matrix for an  $XX(\pi/4)$  gate. (a) The PTM describes an  $XX(\pi/4)$  gate considering stochastic error such as motional heating, motional coherence time, and laser coherence time. (b) The PTM describes an ideal  $XX(\pi/4)$  gate.

and  $\hat{L}_- = \sqrt{\Gamma}\hat{a}$ , where  $\Gamma$  is the heating rate. For these two operators, we sequentially simulate the evolution of each mode, then combine them to obtain the final state. The master equation simulations represent the full density matrix representation for a truncated state space of two qubits and one motional mode truncated to the first 13 Fock states ( $n \leq 12$ ). The laser dephasing can be described by the Lindblad operator of  $\hat{L}_l = \sqrt{1/\tau_l}(\hat{\sigma}_z^{(1)} + \hat{\sigma}_z^{(2)})$ , where  $\tau_l$  is the laser coherence time. We perform a full master equation simulation for this Lindblad operator with all motional modes and spin states included. We truncate the far-off-resonance motional modes, which have a smaller motional excitation, to smaller Fock states to save on computational resources.

### 3.4.2 Pauli transfer matrix

Solving the master equations is efficient enough to analyze gate-level performance, but it becomes redundant for quantum circuit-level simulation. To avoid expensive differential equation solving procedures whenever we encounter an MS gate in a

quantum circuit, we calculate the Pauli transfer matrices (PTMs) before simulating the circuit. The PTM is represented as:

$$(R_\Lambda)_{ij} = \frac{1}{d} \text{Tr}\{P_i \Lambda(P_j)\}, \quad (3.47)$$

where  $P_i$  is the Pauli basis,  $d = 2^n$ ,  $n$  is the number of qubits, and  $\Lambda$  is the linear map [34].  $\Lambda(P_j)$  is equivalent to applying the master equation simulation on a Pauli basis  $P_j$ . Fig. 3.2 (a) shows the PTM which describes the  $XX(\pi/4)$  gate we implemented in experiments, considering the leading order dephasing noise and motional heating.

Single-qubit gates suffer from negligible stochastic noise. Therefore, we represent them with corresponding quantum operation matrices subject to minor coherent errors. In superoperator formalism, a quantum circuit comprising quantum maps (the Mølmer Sørensen gates and the single-qubit rotations) is equivalent to matrix multiplication of the corresponding PTMs and can be calculated efficiently.

# 4

## Experimental Hardware and Control

In this chapter, we discuss the details of experimental hardware and control systems. The experimental hardware includes an ultra-high vacuum chamber, vacuum-related devices, beam modulation and delivery systems for five lasers, and ion fluorescence photon collection optics. The experimental control system contains a main FPGA for experimental logical sequences, a radio frequency system on chip (RFSoC) for coherent qubit operations, a digital PID locking system, several direct digital synthesizers (DDS), and a micro-electromechanical system (MEMS) mirrors steering control device.

### 4.1 Ultra-High Vacuum Environment

Trapping ions for quantum computing requires an ultra-high vacuum (UHV) environment to avoid frequent collisions between ions and background gas molecules. Ideal operating pressure is at a level of  $10^{-11}$  Torr for Ytterbium ions. For lighter atomic species, such as Beryllium, a  $10^{-12}$  Torr pressure is preferred. Fig. 4.1 presents the design of our UHV chamber with accessories. The ion trap, Ytterbium sources, and electronics feedthroughs are mounted in the octagon main chamber. The octagon

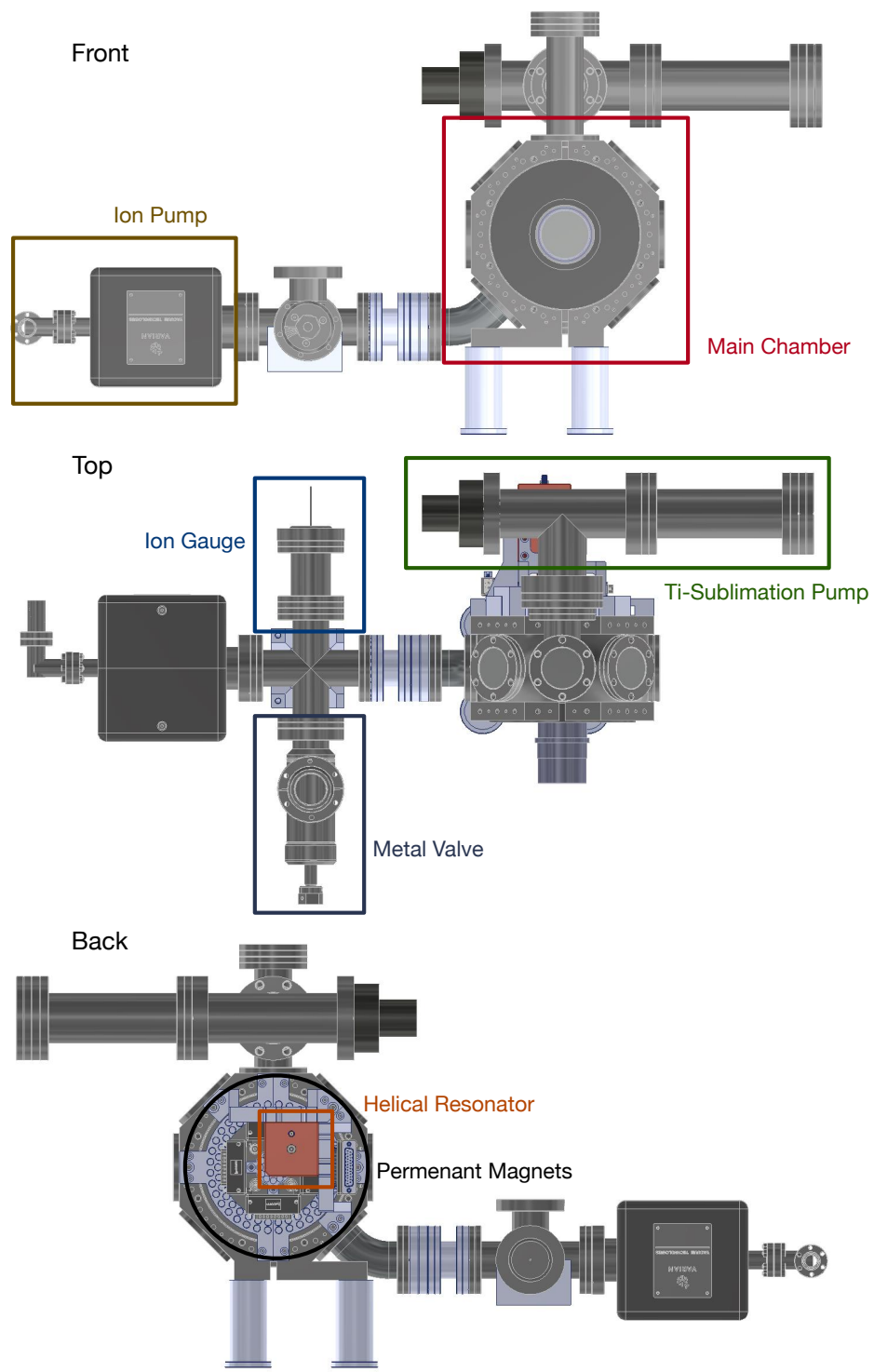


FIGURE 4.1: CAD drawings of the UHV chamber.

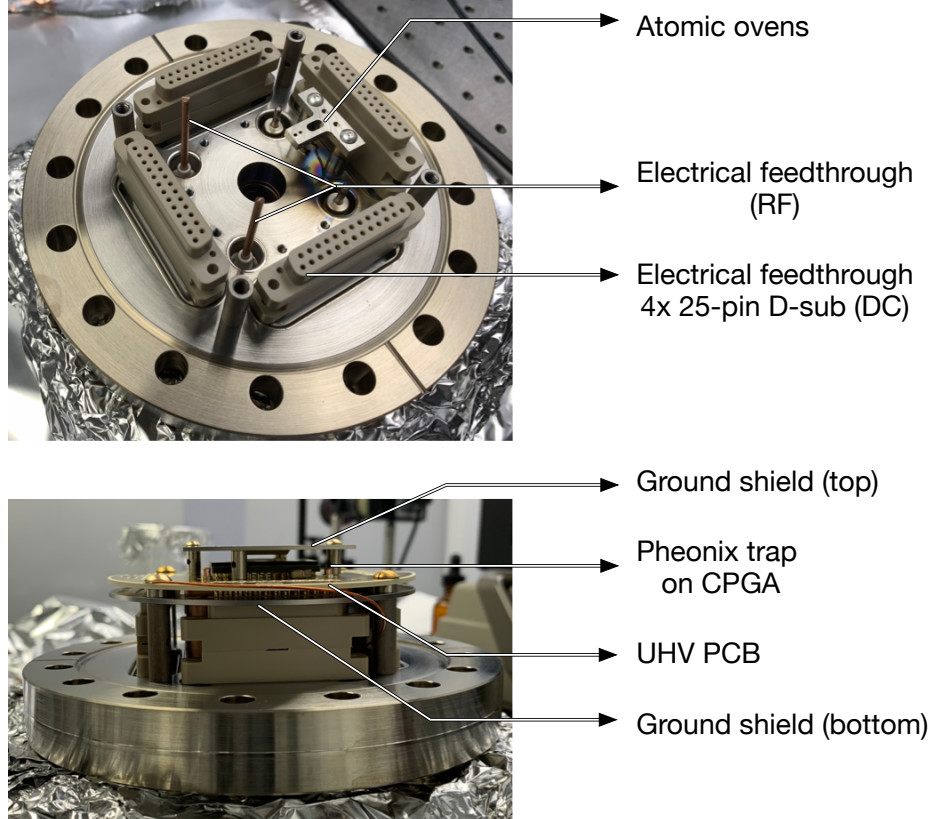


FIGURE 4.2: Photos of customized back flange and back flange assembly.

chamber has seven viewports on the sides, a large front viewport, and a small back viewport. An ion pump and a Ti-sublimation pump are installed to maintain the required vacuum. The vacuum system also features an ion gauge for pressure readout and a metal valve for the initial pump down. A helical resonator and a ring of permanent magnets are mounted directly on the back flange of the octagon chamber. The chamber-mounted design improves mechanical stability.

The back flange is a customized part to fulfill DC and RF voltage control. As we show in Fig. 4.2, the back flange has two high voltage RF feedthroughs, two high current feedthroughs for ovens, and four 25-pin D-Sub feedthroughs for DC voltages control. In the bottom picture of Fig. 4.2, from top to bottom, a titanium ground shield, a UHV PCB, a Phoenix trap with CPGA packaging, and another titanium

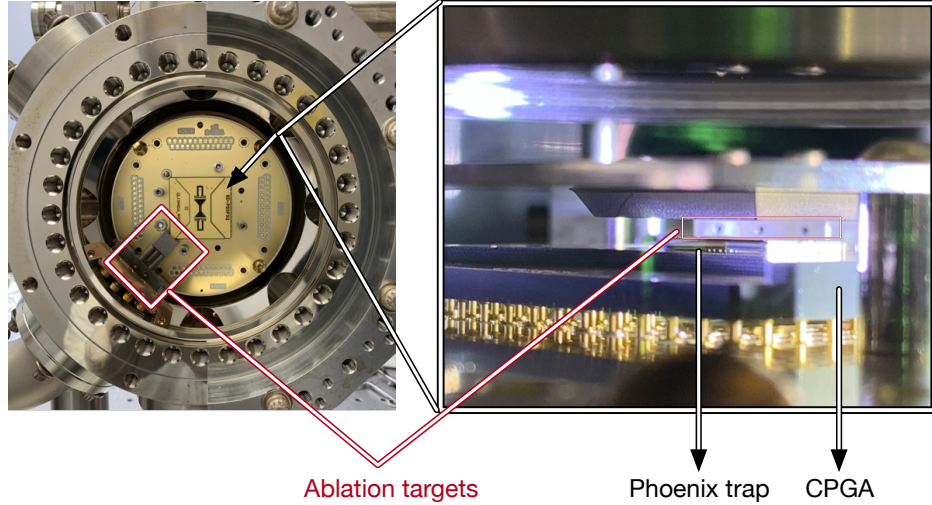


FIGURE 4.3: The photo of a Phoenix trap installed in the chamber without the top ground shield is on the left. The red box marks the ablation targets for ion loading. The photo on the right shows the holes of ablation targets viewing from the top right 45° viewport. The target holes are aligned slightly above the trap surface.

ground shield are stacked up on the back flange like a lasagne.

In Fig. 4.3, the back flange assembly is mounted in the main chamber. We assemble a machined part of ablation targets on the edge of the chamber. The ablation targets are pointing to the top right 45° viewport. The ablation laser<sup>1</sup> beam is aligned to the hole of the ablation target from the viewport.

## 4.2 Optical Design for CW and Ablation lasers

Three CW lasers and one ablation laser are deployed in the system. The wavelengths of the three continuous wave (CW) lasers are 369, 399, and 935 nm, respectively. The CW lasers are responsible for Doppler cooling, optical pumping, and ionization. A 1064 nm pulsed laser is used for ablation loading. Further details can be found in Chapter 2.

No real-time operation is required for 399, 935, and 1064 nm lasers. Therefore, the beam modulation setups for them are trivial. 399 nm laser requires a mechanical

---

<sup>1</sup> Amplitude Minilite Series 1064 nm

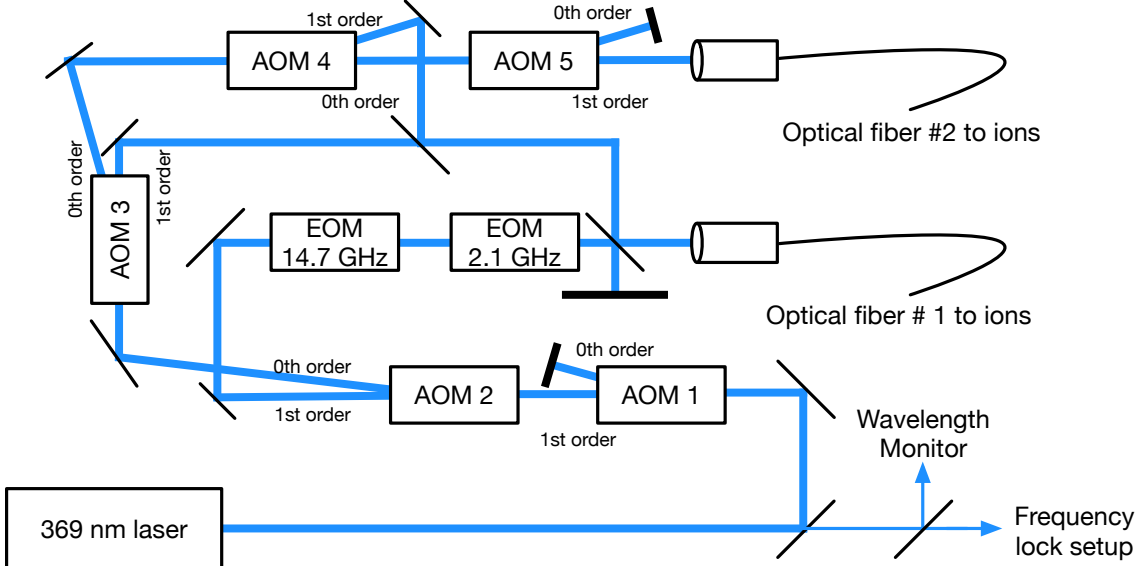


FIGURE 4.4: Schematics of 369 nm laser beam path. AOM 1 serves as an optical shutter for all 369 nm laser beams. AOM 2 serves as the shutter for Doppler cooling and optical pumping. The 1st order beam out of AOM 2 is frequency modulated by a 14.7 GHz EOM and a 2.1 GHz EOM for Doppler cooling and optical pumping, respectively. The detection beam is controlled by AOM 3. AOM 4 and AOM 5 are responsible for two EIT cooling beams. The MogLabs 369 nm laser has only 5 mW output power. To squeeze out as much power as possible, AOM 2, AOM 3, AOM 4, and AOM 5 share the 0th order beam. We note that the AOM diffraction angles in the figure are not to scale. One should use the labels next to beams as a reference.

beam shutter, a wavelength meter lock, and sufficient power. The frequency of the 935 nm laser is stabilized with a wavelength meter lock, and a fiber EOM adds a 3.1 GHz sideband on the beam. We use a 1064 nm laser as an ablation laser, so sufficient beam intensity is the only requirement. Meanwhile, 369 nm lasers require careful frequency, amplitude, and timing control.

#### 4.2.1 Beam modulation for 369 nm beam

In Chapter 2, we discuss the scenarios which require 369 nm laser beams, including Doppler cooling, optical pumping, detection, and EIT cooling. They have a different frequency, amplitude, and polarization requirements. We have the 369 nm beam modulation optics setup as showed in Fig. 4.4. We combine the Doppler cooling

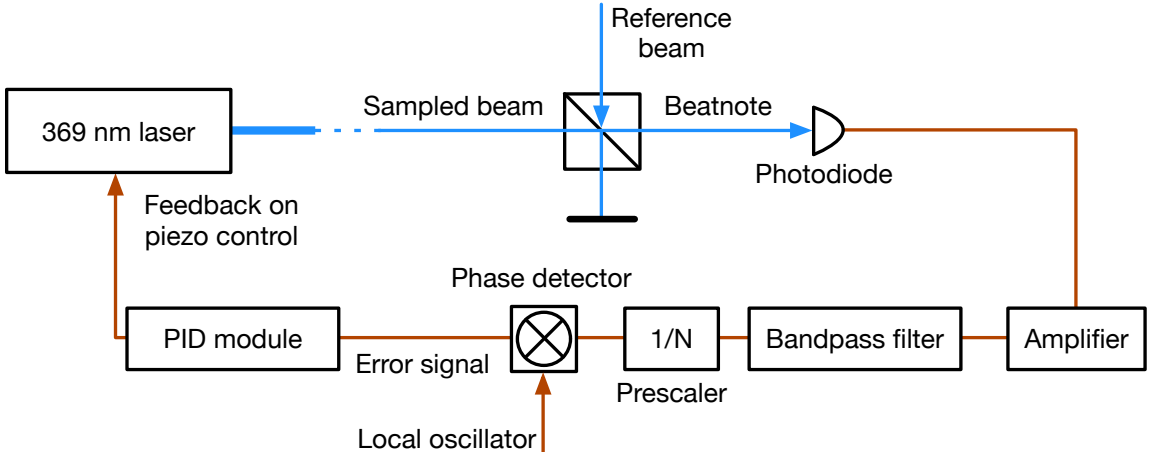


FIGURE 4.5: Schematics of the offset frequency stabilization.

beam, optical pumping beam, detection beam, and the weak probe beam for EIT cooling into one single-mode optical fiber, and we couple the strong coupling beam for EIT cooling and the 399 nm ionization beam into another optical fiber.

In our lab, since we have multiple setups that conduct  $^{171}\text{Yb}^+$  experiments, we implement a scalable offset frequency lock system for CW laser stabilization [35]. Several setups share a single stabilized master laser. We use a reference cavity manufactured by Stable Laser Systems<sup>2</sup>. It is a Fabry-Perot type optical cavity consisting of one plano mirror and one spherical mirror, high-reflective (HR) coated for 369 nm. The master laser is locked to cavity resonance frequency utilizing Pound-Drever-Hall (PDH) technique. Fig. 4.5 shows the schematic of the offset frequency lock on a minion laser side. In experiments, the stabilized master laser has a  $\sim 1$  GHz frequency offset compared to the minion laser. The offset frequency is flexible as long as the beat note signal has a high signal-to-noise (SNR) ratio. Normally, a 20 dB SNR is sufficient. The  $\sim 1$  GHz beat note frequency is divided by a 1/10 prescaler<sup>3</sup> and then compared to the setpoint frequency ( $f_{\text{set}} \approx 100$  MHz) using a

---

<sup>2</sup> Model number: 6010-4

<sup>3</sup> RF-Bay FPS-10-12

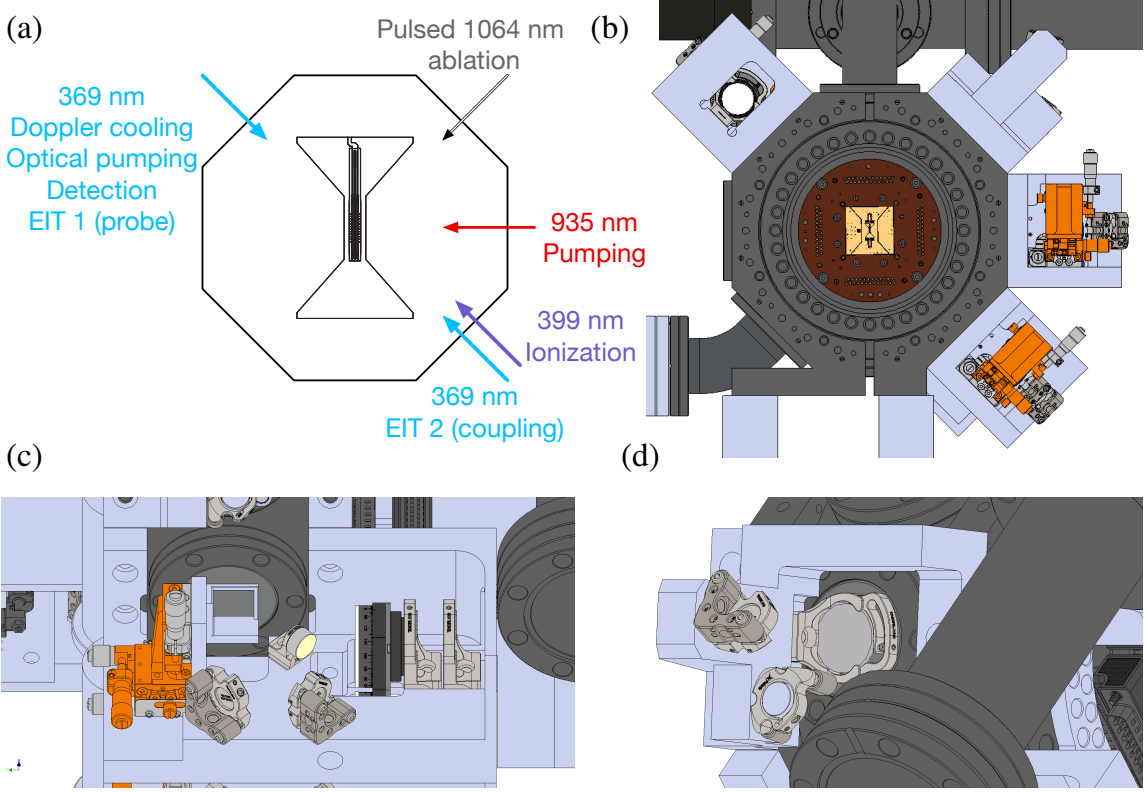


FIGURE 4.6: (a) CW laser delivery geometry (not to scale). 399 nm ionization beam and 369 nm EIT 2 beam are combined before entering the UHV chamber. (b) The front view CAD drawing of four chamber-mounted CW laser delivery plates. (c) The CAD drawing of a CW laser delivery plate. (d) The CAD drawing of the ablation laser delivery plate.

phase detector<sup>4</sup>. The PID module processes the error signal out of the phase detector and feeds the results back to the piezo-controlled grating of the minion laser. When the minion laser is locked, the frequency offset between master and minion laser is  $10f_{\text{set}}$ . Therefore, by adjusting the setpoint frequency, which DDS generates, the frequency of the minion laser is digitally programmable.

#### 4.2.2 Beam delivery system

Fig. 4.6 (a) presents the beam geometry for CW lasers and the ablation laser. Doppler cooling beam propagates along an axis which is  $45^\circ$  to the trap axis, so

---

<sup>4</sup> RF-Bay, PDF-100

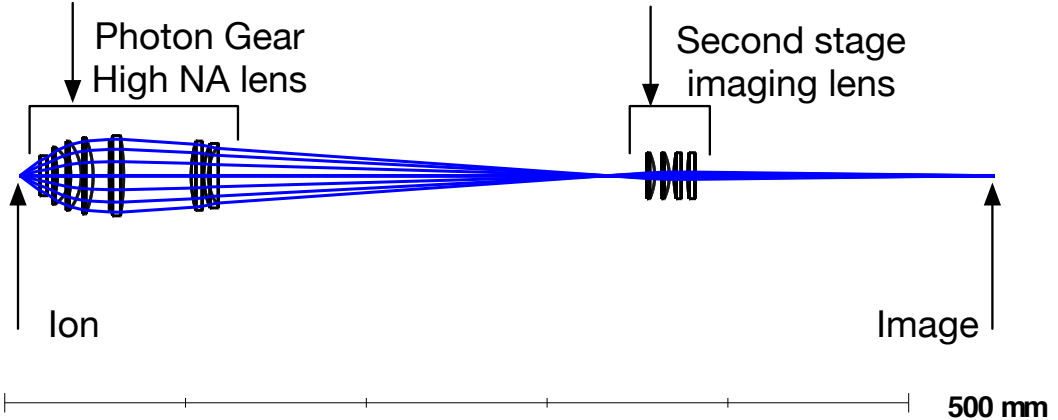


FIGURE 4.7: Ray tracing diagram of the two-stage imaging system generated by Zemax.

both axial and radial motional modes can be Doppler cooled. To maximize the EIT cooling effect requires that the probe beam and the coupling beam maintain a counter-propagating configuration. The ablation laser propagates from the top right viewport to aim at the ablation target showing in Fig. 4.3. There is no geometrical constraint for 935 nm and 399 nm beams.

Traditionally, beam delivery optics and the vacuum chamber are mounted on the same optical platform. However, mechanical vibration causes displacement fluctuation between the optics and the vacuum chamber in such an arrangement. In order to improve the mechanical stability, we design the chamber-mounted CW and ablation laser delivery plate showing in Fig. 4.6 (b), (c), and (d). The CW lasers are delivered to the corresponding chamber-mounted plates by optical fibers. The beams can be steered precisely by two mirrors on kinetic mounts and a final projection lens on an XYZ linear translation stage. All three CW laser delivery plates share a similar design, and the differences include coating and lens selections. Delicate CAD design in advance improves the optical alignment stability and makes initial alignment much more effortless.

#### *4.2.3 Imaging system*

There are two stages in the ion fluorescence imaging system. It contains a 0.6 NA lens, which is designed and fabricated by Photon Gear [36], and a second stage lens set assembled by off-the-shelf lenses. The total magnification is designed to be 50 times ( $\sim 8.6x$  for Stage I and  $\sim 6x$  for Stage II). When the ion separation is  $\sim 5 \mu\text{m}$ , the image separation is  $\sim 250 \mu\text{m}$ , which matches the  $250 \mu\text{m}$  pitch of the 32 channel multi-mode fiber array<sup>5</sup>. The collected photons from individual ions are coupled into individual multi-mode fibers and sent to corresponding fiber PMTs<sup>6</sup>.

### 4.3 Optical Design for Raman Beams

A 355 nm pulsed laser is used to drive Raman transitions. We denote 355 nm laser as Raman laser or Raman beam. Further details about Raman transitions can be found in Chapter 3.

#### *4.3.1 Beam modulation*

We use acousto-optic modulators (AOMs) to control the frequency, phase, and amplitude of all three Raman beams. A photon of the beam modulation optics is showed in Fig. 4.8 with the optical paths marked with colored lines. The repetition rate feed-forward compensation frequency is added to two individual beams. The beam deflection angle varies with the change of RF signal frequencies applied on the individual AOMs. To compensate for the beam pointing deviation, we use a double-pass AOM configuration for individual AOMs. When we run Mølmer Sørensen gates, a bichromatic waveform is applied on the global AOM. The power of two tones needs to be balanced to minimize the four-photon Stark shift; however, the frequencies of two tones vary up to 6 MHz. In order to compensate for the deflection angle differ-

---

<sup>5</sup> Fiberguide Industries, 100  $\mu\text{m}$  cores, 250  $\mu\text{m}$  pitch

<sup>6</sup> Hamamatsu, H10682-210

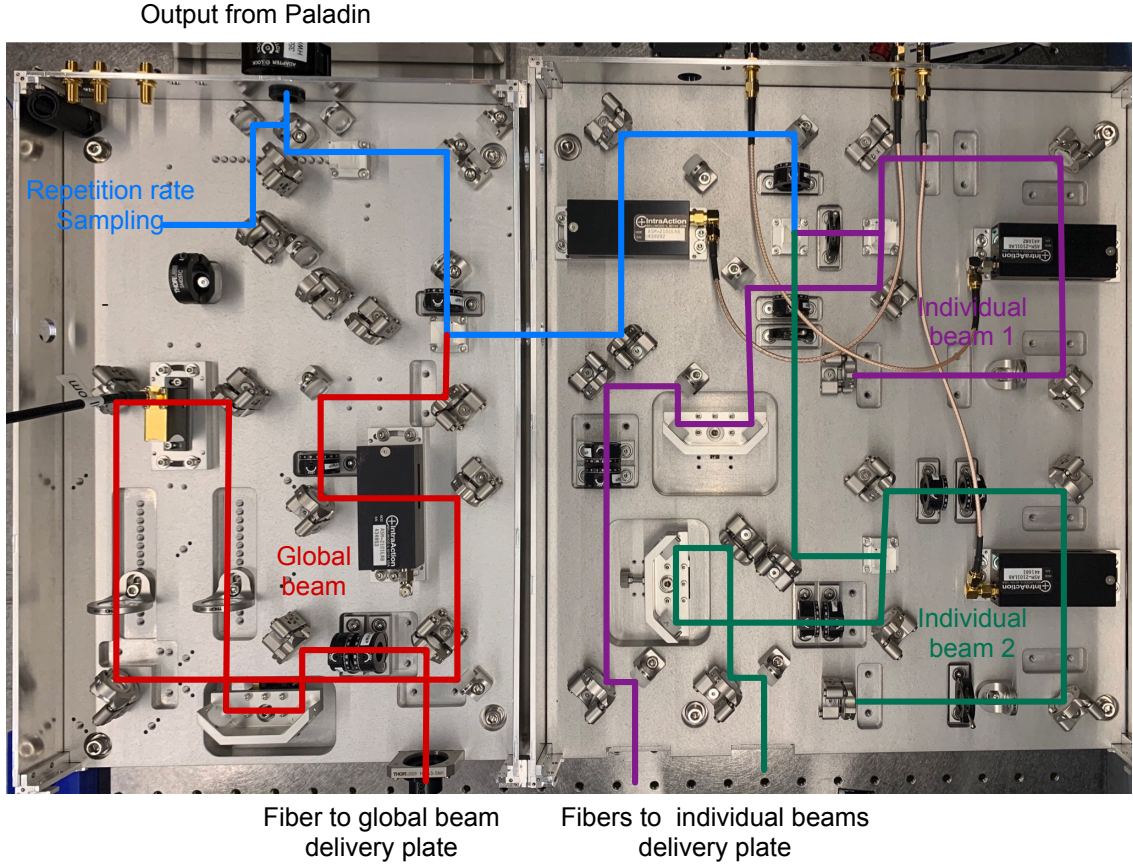


FIGURE 4.8: Photo of the Raman beam modulation plate. Beam paths of the global beam and two individual beams are marked with red, purple, and green lines.

ence and conserve beam power, instead of using a double-pass AOM configuration, we build a 1 : 1 telescope and place the global AOM at the focal point. Single-mode photonic crystal fibers are used to deliver the individual addressing beams to the beam-steering system and deliver the global beam to beam-shaping optics [37].

As showed in Fig. 4.8, the optics are mounted directly on a custom aluminum plate. Together with the custom Raman beam delivery plates (showed in Fig. 4.9 (d)), they improve the mechanical stability along the beam path. Comparing the current Raman optics implementation to the traditional “posts + mirror/lens mounts” combination, the Raman laser coherence time improves from 83.3 ms to 334 ms.

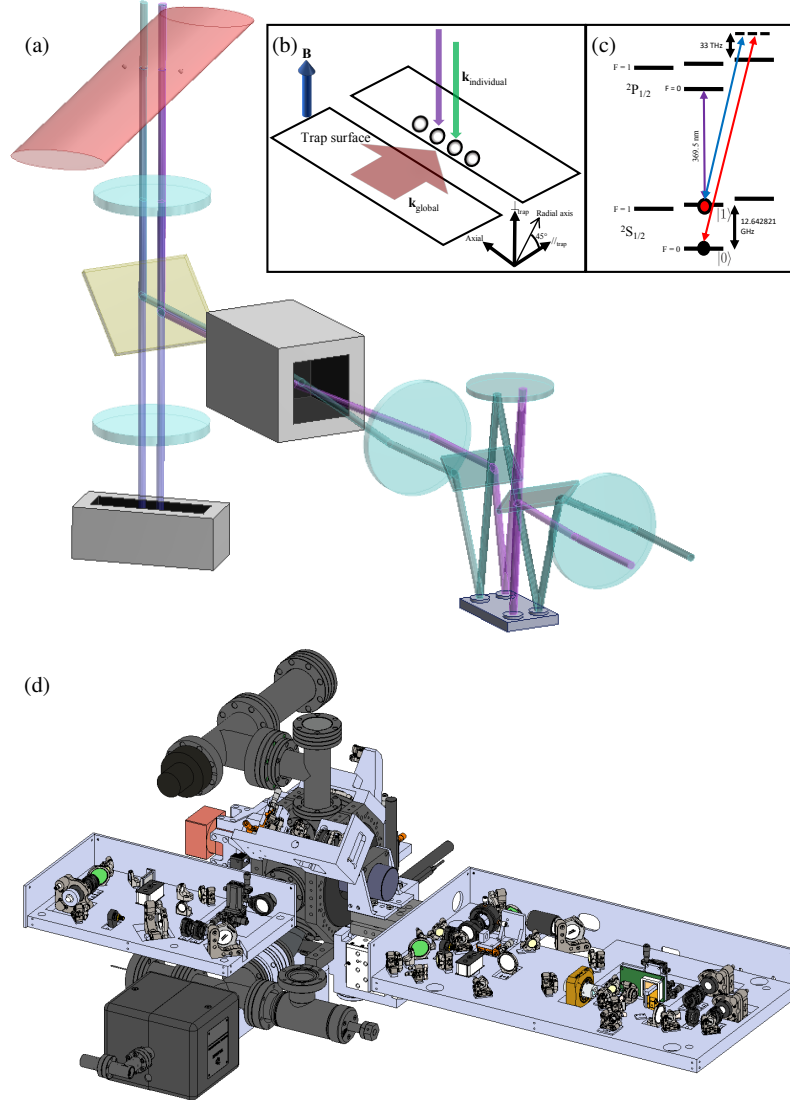


FIGURE 4.9: (a), (b) Schematic representation of the Raman beam optical setup. The two individual addressing beams (purple) are steered by two pairs of mirrors tilting in orthogonal directions on a MEMS device to address any qubit in a chain (steered beam is shown in green). The trap's axial axis is rotated by 45° with respect to both tilting axes of the MEMS mirrors to utilize orthogonal tilting mirrors in order to maximize the addressable qubits. The projection and beam combining optics are represented by a black box. (c) Energy level schematic of a  $^{171}\text{Yb}^+$  ion. The red and blue lines indicate the two-photon Raman transition for qubit operations. (d) CAD drawing of the Raman beam delivery system.

### 4.3.2 Beam delivery

The optical setup for implementing Raman quantum gates is schematically illustrated in Fig. 4.9 (a) and (b). One of the two orthogonal Raman beams is a global beam with an elliptical profile that simultaneously illuminates all of the qubits. The optical power and beam waist radius of the global beam are 40 mW and  $8 \mu\text{m} \times 110 \mu\text{m}$ . The other is a pair of tightly focused individual addressing beams independently steered across the qubit chain using a MEMS device. Steering of each individual beam is accomplished by a pair of MEMS mirrors each tilting in orthogonal directions. The details of the beam steering system is described in Refs. [38, 30].

## 4.4 Experimental Control System

The experimental control system can be divided into three subsystems, a real-time incoherent control subsystem, a real-time coherent control subsystem, and an off-line control subsystem. The real-time incoherent control is responsible for ion loading, ion cooling, qubit initialization, qubit state detection, ion trap DC electrodes control, and MEMS mirrors steering. The real-time coherent control focuses on Raman beam modulation, and we call it “coherent” due to the fact that the phase of beams matters in qubit operations. The off-line control consists of several fixed-parameter RF sources and a digital PID device for beam frequency and amplitude stabilization. Fig. 4.10 presents the experimental control schematic.

### 4.4.1 Real-time incoherent control subsystem

The nexus of the experimental control system is an FPGA that coordinates all real-time operations. This FPGA controls the real-time incoherent operations directly. We design the control hardware to be compatible with sets of control software/firmware. When Opal Kelly XEM 6010-LX45 serves as the main FPGA, we use the IonControl firmware and software developed by Sandia National Laboratories.

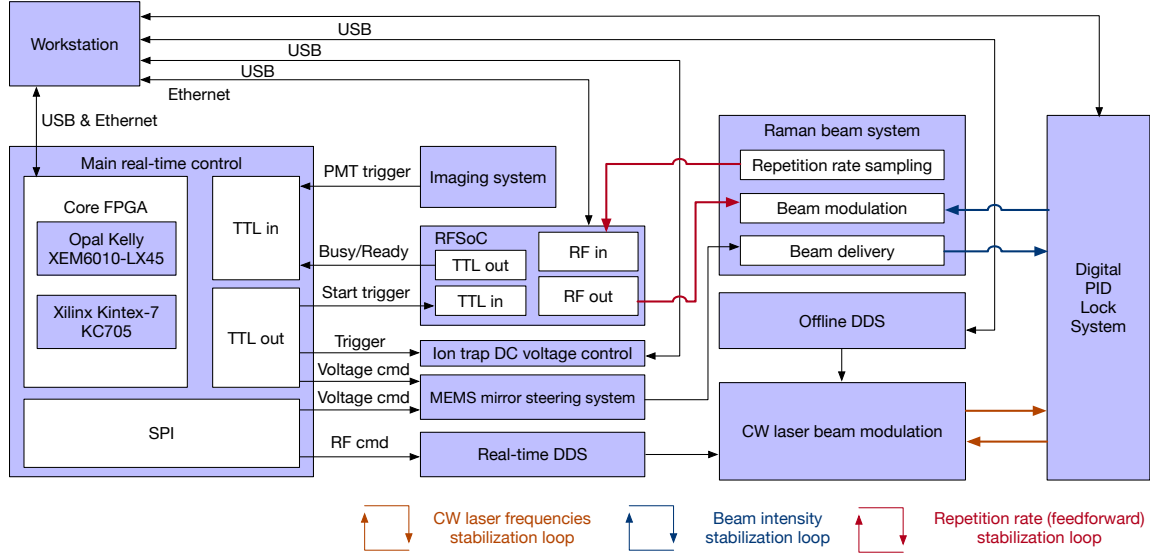


FIGURE 4.10: Schematics of the experimental control system.

When Xilinx KC705 serves as the main FPGA, it is programmed to run Advanced Real-Time Infrastructure for Quantum physics (ARTIQ) control system developed by M-Labs.

The main FPGA is connected to a custom breakout board. It features 56 general-purpose input/out (GPIO) channels. Thirty-two of them serve as digital outputs, and 24 of them serve as digital inputs. The breakout board provides serial peripheral interfaces (SPIs) to control 8 DDS chips and MEMS mirror steering angles.

Thirty-two digital outputs control all real-time output triggers and switches in experiments. All external triggers, including the PMT counts, are sent to the digital input channels. Eight real-time DDS channels drive CW laser AOMs which require real-time frequency or amplitude modifications. Meanwhile, six off-line DDS channels provide fixed RF signals for some of the CW laser AOMs. All fourteen DDS channels are switched on/off by digital outputs from the main control breakout board. MEMS mirrors deployed in the Raman beam delivery system are steered by applying a high voltage (0 to 150 V) on the electrodes underneath the mirrors. Therefore, the main FPGA programs the MEMS control device consisting of 8 DAC output channels and

switches.

#### 4.4.2 Real-time coherent control subsystem

In a general experimental sequence, the main FPGA performs cooling and qubit initialization, and then it relays the duty to the real-time coherent control subsystem to execute the coherent qubit operations through an output trigger. After the coherent operations, the system is returned under the control of the main FPGA to execute the latter sequences.

The core device of the real-time coherent control subsystem is RFSoC<sup>7</sup>. The Raman beams pass through AOMs driven by RFSoC, which provides the ability to change the amplitude, frequency, and phase of each beam. The RFSoC firmware is provided by Sandia National Laboratories QSCOUT project [39]. We note that RFSoC can be considered as more sophisticated DDSs. It preserves the merit that DDS provides a long sequence for free, and it also supports complex modulations like an arbitrary waveform generator (AWG), although the number of tones for one channel is limited at two. Each RF channel supports two-tone output, and it is convenient for running Mølmer Sørensen gates.

Another RFSoC advantage over AWG is the built-in Raman laser repetition rate stabilization. It reads the repetition rate sampling signal with an ADC channel. The digital result is mixed with a setpoint frequency. The beat note mixed with the feedback signal is sent to a built-in PID module as the error signal. Once this feedback loop is stabilized, it adds the real-time feedback frequency (with an adjustable prefactor) to the output RF signal. The repetition rate lock is illustrated schematically in Fig. 4.11. We note that the repetition rate of the laser is not actually stabilized, but the fluctuation of the repetition rate is measured. A real-time compensation due to the repetition rate fluctuation is then calculated and added to the corresponding

---

<sup>7</sup> Xilinx Zynq ULtraScale+ RFSoC ZCU111 Evaluation Kit

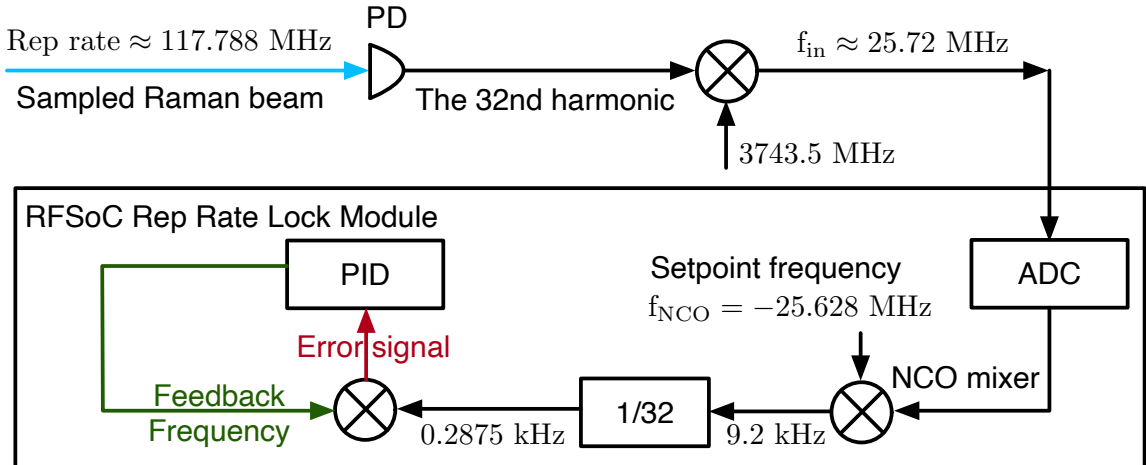


FIGURE 4.11: Schematics of repetition rate stabilization. We take the 32nd harmonic of the sampled repetition rate from a photodiode and mix it with a 3.7435 GHz signal. The ADC then reads the beat note in the repetition rate stabilization module of RFSoC. The digital signal passes through an NCO mixer, and the frequency difference between the sampled and desired repetition rates is obtained. Finally, a PID module is used to generate the feedback frequency by stabilizing the error signal at zero. The feedback frequency is the  $\delta_{\text{rep}}$  in Eq. 4.1.

RF output.

For example, when a counter-propagating single-qubit rotation is implemented, we fulfill the following equation for the whole time:

$$f_{\text{qubit}} = n \times (f_{\text{rep}} + \delta_{\text{rep}}) + 2(f_1 + \delta_1) + f_s - f_g, \quad (4.1)$$

where  $f_{\text{qubit}} = 12.64282263$  GHz is the qubit transition frequency,  $f_{\text{rep}} = 117.785$  MHz is the repetition rate set point,  $n$  is a positive integer (we set it to 104 for convenience),  $f_1 = 195$  MHz is the frequency applied on the double-pass AOM for individual beam modulation,  $f_s = 210$  MHz is the frequency applied on the shutter AOM for individual beam, and  $f_g = 206.843$  MHz is the frequency applied on the global beam AOM. When the real repetition rate deviates from the set point for  $\delta_{\text{rep}}$ , the feedback frequency  $\delta_1$  compensates the difference. Therefore,

$$\delta_1 = -\frac{n}{2} \times \delta_{\text{rep}}, \quad (4.2)$$

and the adjustable prefactor is  $-n/2 = -52$  in this example.

The phase bookkeeping feature of RFSoC is introduced in Appendix B.2.

#### 4.4.3 Off-line control subsystem

The off-line control subsystem consists of off-line RF sources and a multi-channel digital PID controller. Both of them are featured in Fig. 4.10. The off-line RF sources provide RF signals to acousto- and electro-optic modulators for CW lasers. The driving frequency, phase, and amplitude of these AOMs and EOMs do not change in real-time. The main FPGA switches these RF signals on/off in real-time by digital outputs.

The multi-channel PID controller consists of an Opal Kelly XEM 6010 LX-45 FPGA mounted on a custom breakout board. It has the same configuration as the main FPGA setup. The FPGA is programmed with a PID control firmware that supports 8 DAC channels, 4 DDS channels, and 8 ADC channels. The PID module uses 128-bit registers for computing to ensure high precision. Fig. 4.5 shows the schematic of frequency offset locking for 369 nm. The error signal is read by one ADC channel, and it is handed over to the PID module for processing, then the feedback voltage output is sent back to piezo control of the laser by one DAC channel. The principle of this stabilization loop is also true for other CW laser frequency stabilization.

We stabilize the Raman beam intensity with the PID controller. All three Raman beams are sampled before entering the UHV chamber by photodiodes<sup>8</sup>. The current signals out of the photodiodes are converted to a voltage signal by transimpedance amplifiers<sup>9</sup>. Carrying the beam intensity information, the voltage signal is read by an ADC channel and is processed by the PID module. The RF signal goes through

---

<sup>8</sup> Thorlabs SM05PD3A

<sup>9</sup> Thorlabs AMP120

a voltage variable attenuator<sup>10</sup> (VVA) before applying on the Raman beam AOM. Therefore, the feedback voltage out of the DAC channel is applied on the VVA to adjust the amplitude of the RF signal applied on the Raman beam AOM. We note that the beam intensity and RF amplitude on AOM maintains a non-linear and monotonic relation.

---

<sup>10</sup> Mini-Circuits ZX73-2500+

# 5

## Quantum Gates in Experiments

### 5.1 Single-qubit Gates

The single-qubit gates consist of the single-qubit rotation  $R(\theta, \phi)$  and phase gate  $RZ(\theta)$  which can be described by unitary operators:

$$R(\theta, \phi) = \begin{pmatrix} \cos \frac{\theta}{2} & -ie^{-i\phi} \sin \frac{\theta}{2} \\ -ie^{-i\phi} \sin \frac{\theta}{2} & \cos \frac{\theta}{2} \end{pmatrix}, \text{ and} \quad (5.1)$$

$$RZ(\theta) = \begin{pmatrix} 1 & 0 \\ 0 & e^{i\theta} \end{pmatrix}. \quad (5.2)$$

We note that  $R(\theta, \phi)$  is universal, but it is convenient to have  $RZ(\theta)$  in the toolkit.

The single-qubit rotation  $R(\theta, \phi)$  is implemented by applying the effective Hamiltonian:

$$\tilde{H}_{\text{eff}} = \frac{\hbar}{2} \begin{pmatrix} 0 & \Omega \\ \Omega^* & 0 \end{pmatrix}$$

where  $\Omega = \frac{\Omega_p^* e^{-i\phi_p} \Omega_c e^{i\phi_c}}{2\Delta} = \frac{\Omega_p^* \Omega_c e^{i(\phi_c - \phi_p)}}{2\Delta}$ . The rotation angle  $\theta = \Omega t$  is controlled by the Rabi frequency and the pulse duration, while the phase  $\phi$  is determined by  $\phi_c - \phi_p$ . We note the absolute global phase does not matter in quantum computing,

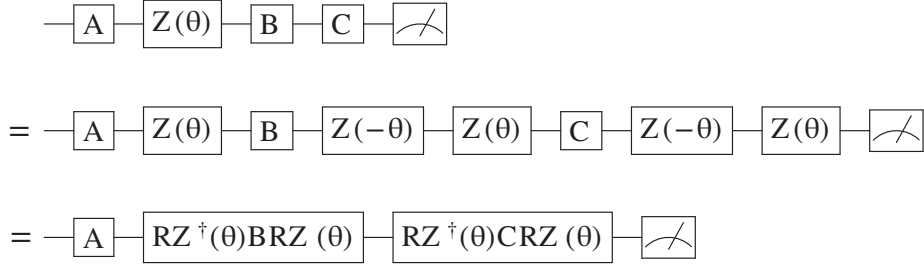


FIGURE 5.1: The schematic of applying a virtual single-qubit phase gate in quantum circuits.  $RZ^\dagger(\theta)BRZ(\theta)$  represents a  $B$  operation whose phase is advanced by  $-\theta$ . Since the native measurement in experiments is on the Z basis, the last  $RZ(\theta)$  can be ignored.

and when we assume  $\phi_c - \phi_p = \phi'$  produces X rotations  $\phi_c - \phi_p = \phi' + \pi/2$  produces Y rotations. For a convenient notation, we have  $\phi' = 0$ .

The phase gate  $RZ(\theta)$  can be implemented both physically and virtually. The phase difference can be generated by inducing a certain amount of light shift for a duration,  $\theta = \delta_{LST}$ . A better way to implement the phase gate in a circuit is to advancing the phase of all subsequent gates by  $-\theta$ . The scheme is illustrated in Fig. 5.1. The virtual phase gate has much higher fidelity, and it is much easier to apply an arbitrary  $\theta$  in experiments, especially when  $\theta$  is small.

We can drive  $|0\rangle \leftrightarrow |1\rangle$  Rabi oscillations with counter-propagating and co-propagating configurations using Raman transitions. For single-qubit rotations, co-propagating configuration produces better gate fidelity because it decouples from motional mode by nature. However, since we need a counter-propagating configuration for entangling gates, the Raman beam polarization is different in the two configurations. We usually use counter-propagating single-qubit gates in quantum circuits. Note that we can simultaneously use co-propagating single-qubit gates and counter-propagating entangling gates in a quantum circuit at the expense of the more complicated control. However, since the bottleneck of the circuit performance is entangling gates, we choose to perform counter-propagating single-qubit gates for

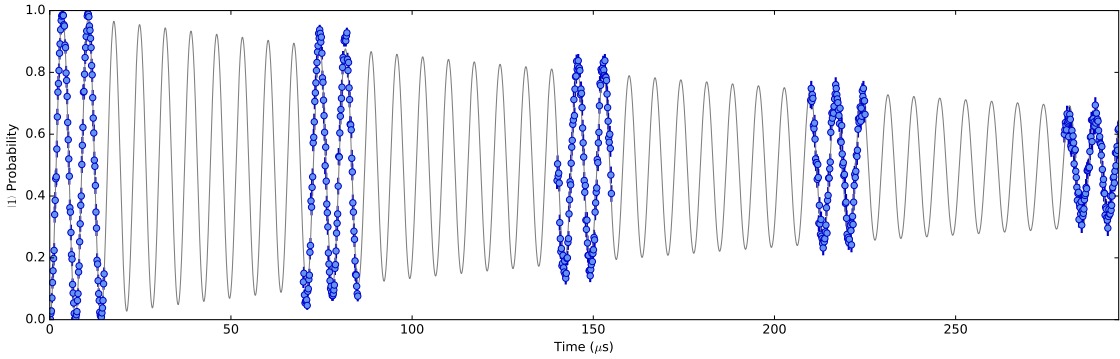


FIGURE 5.2: Long-time Rabi oscillations using counter-propagating Raman transitions. The single-qubit rotation is driven with  $\Omega = 2\pi \times 141$  MHz. A  $1/e$  coherence of  $\sim 84$  cycles ( $\sim 300$   $\mu$ s) is found.

convenience.

Even with counter-propagating configuration gates, the gate error can be as low as  $10^{-4}$ . Fig. 5.2 shows a long-time Rabi oscillation. The Rabi frequency is  $\approx 2\pi \times 141$  MHz. We observe the contrast decay due to beam intensity instability, motional heating, and beam phase instability. A  $1/e$  coherence of  $\approx 84$  cycles is found in the long-time Rabi oscillation. The dominant error source for the decoherence is beam intensity instability.

A Ramsey experiment, which is illustrated in Fig. 5.3(a), can be used to study the decoherence as a result of motional heating and Raman beam phase instability. In counter-propagating configuration, the coupling beam and probe beam have independent beam paths. Any mechanical vibration along the beam path will cause fluctuation in  $\phi_c - \phi_p$ . However, in the co-propagating configuration, two Raman beams share an identical beam path. Even if mechanical vibration happens,  $(\phi_c + \Delta\phi) - (\phi_p + \Delta\phi)$  remains unchanged. Also, co-propagating is not affected by the instability of motional states.

As we expected, we measure a coherence time of 494 ms with counter-propagating configuration and a coherence time of 1685 ms with co-propagating configuration as

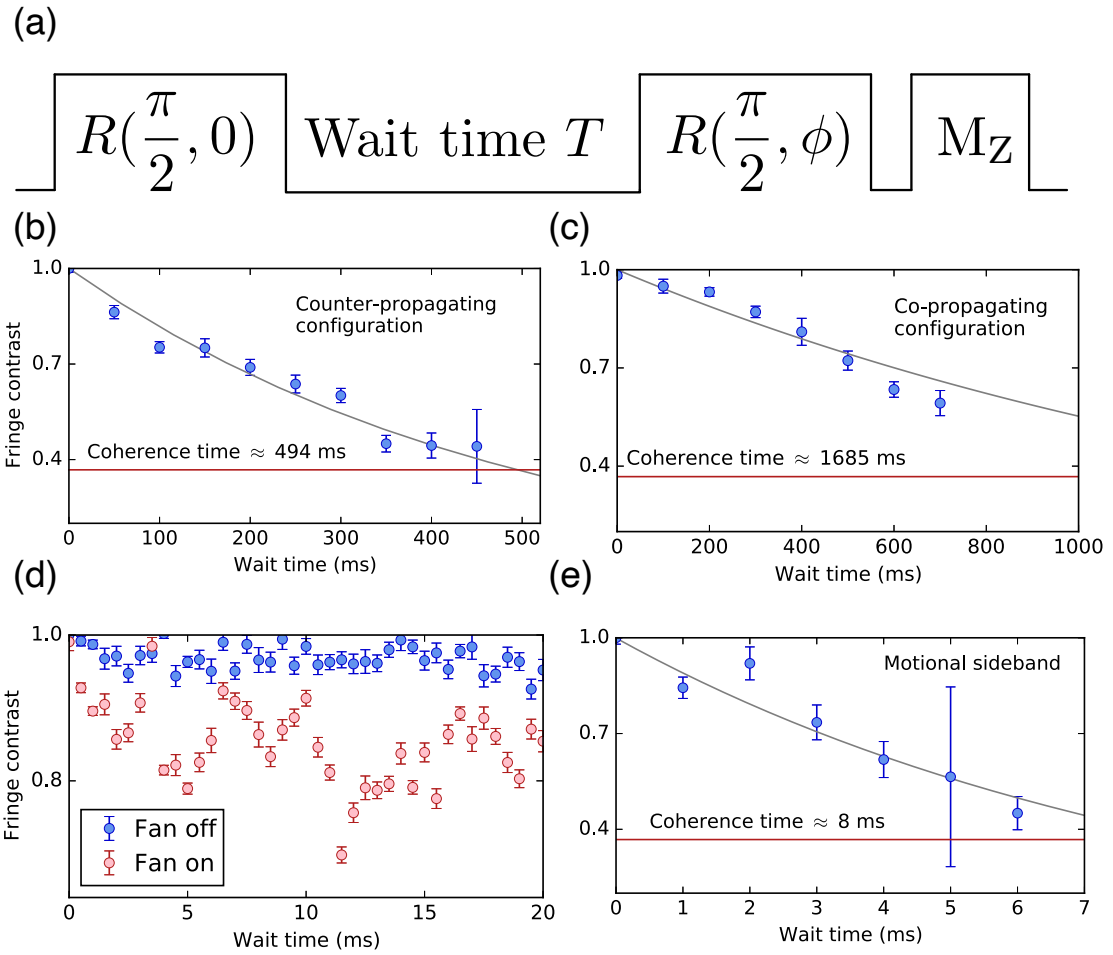


FIGURE 5.3: Ramsey experiments. (a) The pulse sequence of a bare Ramsey measurement. A wait time  $T$  is between two half  $\pi$  rotations. The relative phase between two rotations varies, and we obtain a sinusoidal curve in the plot of bright state population v.s. relative phase. Ideally, the fringe contrast is 1, and it reduces due to decoherence. (b) The data of Ramsey contrast depending on wait time using counter-propagating carrier transitions. A coherence time of 494 ms is observed. (c) The data of Ramsey contrast depending on wait time using co-propagating carrier transitions. A coherence time of 1.6 s is observed. (d) A fine scan of Ramsey contrasts using counter-propagating carrier transitions. Blue data points are taken with the HEPA filter fan off, and red data points are taken with the HEPA filter on. We observe a  $\approx 8$  ms (125 Hz) revival period (frequency) due to mechanical fluctuations from the HEPA filter fan. (e) A motional coherence time of  $\approx 8$  ms is measured by applying blue sideband half pi transitions before and after the wait time.

shown in Fig. 5.3(b) and (c). The measurements are done with bare Ramsey sequences, and we can increase the coherence time with dynamic decoupling techniques [40]. Fig. 5.3(d) presents the comparison between an undisturbed Raman beam path and a disturbed Raman beam path, both using counter-propagating configuration. When periodical mechanical fluctuations happen along the beam path, the coherence is sabotaged. It is the reason why we fabricate stable Raman optics and box them up. The efforts of building high stability optics are introduced in Chapter 4.

Replacing the carrier rotations  $R(\pi/2, 0)$  and  $R(\pi/2, \phi)$  with blue sideband half- $\pi$  rotations in Ramsey sequences, we can extract an estimated motional coherence time lower bound of  $\approx 8$  ms. The motional coherence time used to be  $\approx 36$  ms before we moved the setup to a new lab. We assign this reduction to higher 60 Hz Magnetic field noises (25 mG peak-to-peak). The 60 Hz noises couple into the RF power stabilization loop and sabotage the motional coherence. We are actively solving the problem by both protecting the RF stabilization electronics and shielding the chamber with a  $\mu$ -metal shield.

### 5.1.1 Gate Set Tomography

This section contains results from

**Bichen Zhang**, Swarnadeep Majumder, Pak Hong Leung, Stephen Crain, Ye Wang, Chao Fang, Dripto M. Debroy, Jungsang Kim, and Kenneth R. Brown, arXiv preprint arXiv:2104.01119 (2021) [41].

We design an experiment to measure the performance of SK1 gates and test how well GST predicts their performance. The experiment serves as a preliminary systematic error characterization. First, we run GST on a gate set composed of the SK1 compiled gates  $\{X_{SK1}(\pi/2), Y_{SK1}(\pi/2)\}$ , followed by an experiment where we run GST on a gate set comprised of the raw gates that generate SK1 sequences  $\{X(\pi/2), Y(\pi/2), SK1_X^+(2\pi), SK1_X^-(2\pi), SK1_Y^+(2\pi), SK1_Y^-(2\pi)\}$ . GST produces

a completely positive trace-preserving map for each gate, represented as a Pauli Transfer Matrix (PTM).

We calculate the fidelity of the SK1 gates and the raw gates from these PTMs. The PTMs allow us to calculate any fidelity and we choose the average gate fidelity,  $\mathcal{F}(U, \mathcal{E}) = \int d\psi \langle \psi | U^\dagger \mathcal{E}(|\psi\rangle\langle\psi|) U |\psi\rangle$  where  $U$  is the ideal gate and  $\mathcal{E}$  is the actual gate [42]. From the GST PTMs, we calculate a fidelity for SK1  $X(\pi/2)$  and SK1  $Y(\pi/2)$  of 0.99936(5) and 0.99927(3), respectively, while the fidelity for raw-compiled  $X(\pi/2)$  is 0.9982(1) and for  $Y(\pi/2)$  is 0.9985(2). We see a clear improvement in fidelity due to the SK1 composite pulses. Also, smaller error bars in the calculated fidelity of SK1 gates indicate that the gates are more uniform. The estimated error generator for each gate, which is a Lindbladian type operator that acts after the ideal gate ( $G = e^L G_0$ ), describes how the gate is failing to match the target. Specifically, the Hamiltonian projection of this error generator produces the coherent part of the error. We find that SK1 turns  $\sim 1\%$  overrotation into  $\sim 0.01\%$  overrotation as expected.

We then combine the PTMs obtained from the raw pulse GST to construct SK1  $X(\pi/2)$  and  $Y(\pi/2)$  gate PTMs. Notice that the constructed PTMs are significantly different from the direct SK1 gate PTMs obtained from composite pulse GST. The fidelity for the predicted SK1  $X(\pi/2)$  gate is 0.9917(4), and for the  $Y(\pi/2)$  gate it is 0.9931(2). Fig. 5.4 contains box plots of the calculated fidelities. It indicates that raw pulse GST predicts SK1 composite pulses degrade gate fidelities. This result contradicts the experiment, where SK1 does improve the gate performance. This discrepancy can be explained by an overrotation error that is slowly varying. The raw pulse GST averages over the time-varying overrotations, yielding a PTM that describes average raw pulses for which SK1 would not be useful. Simulations readily reproduce this behavior.

We use pyGSTi (version 0.9.9.1) [43] for all GST-related works. The experi-

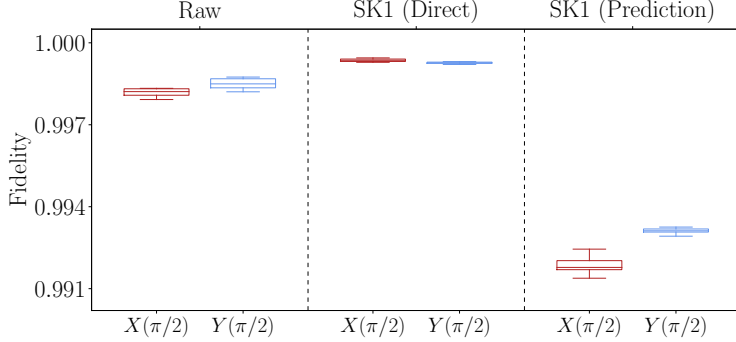


FIGURE 5.4: Average gate fidelity comparison. We compare the average gate fidelity of three instances of  $X(\pi/2)$  (Red) and  $Y(\pi/2)$  (Blue) gates. The three cases considered are the direct characterization of raw gates, direct characterization of SK1 gates, and predicted characterization of SK1 gates based on GST results on the raw gates. The boxplot displays the minimum, the maximum, the sample median, and the first and third quartiles of the dataset.

mental circuits are generated by pyGSTi’s fiducial and germ selection algorithms. Fiducial sequences are used to prepare and measure an informationally complete set of operations. Germs are designed to amplify all possible gate errors. We use the algorithms to generate the appropriate fiducials and germs given a set of operations (also called the gate set). Our gate sets are  $\{X_{SK1}(\pi/2), Y_{SK1}(\pi/2)\}$  and  $\{X(\pi/2), Y(\pi/2), SK1_X^+(\pi/2), SK1_X^-(\pi/2), SK1_Y^+(\pi/2), SK1_Y^-(\pi/2)\}$ . Fiducials and Germs in hand, we choose the length of the experiments (number of times to repeat each germ between fiducial pairs) as  $L = 256$  and  $L = 32$ , respectively. The experiment lengths are different for two gate sets because raw gates are noisier than composite pulse gates, and raw gates reach a similar noise level as composite pulse gates with less noise amplification.

We run standard GST as implemented in pyGSTi. Results of the gate set  $\{X_{SK1}(\pi/2), Y_{SK1}(\pi/2)\}$  follow directly from the output provided by GST (other than error bars which we will discuss next). For the gate set  $\{X(\pi/2), Y(\pi/2), SK1_X^+(\pi/2), SK1_X^-(\pi/2), SK1_Y^+(\pi/2), SK1_Y^-(\pi/2)\}$ , we get the PTMs for the elemen-

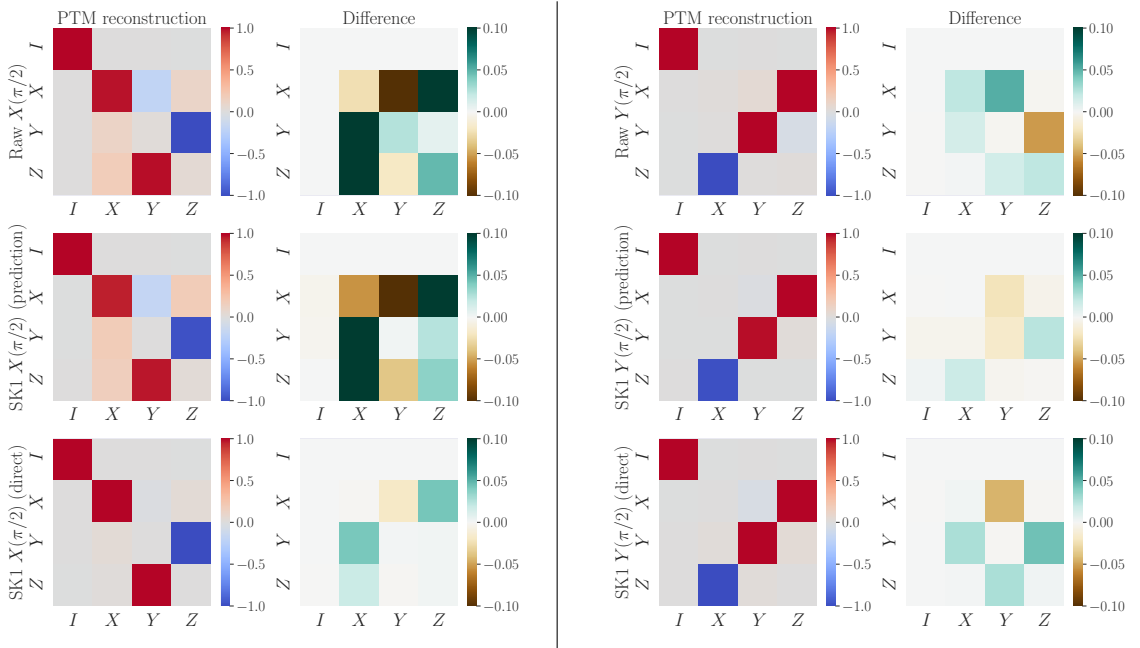


FIGURE 5.5: Characterization of  $X(\pi/2)$  and  $Y(\pi/2)$  gates using Gate Set Tomography. Pauli transfer matrices for raw, SK1 (GST prediction), and SK1 (direct GST characterization). The left two columns represent  $X(\pi/2)$  gates, and the right two columns represent  $Y(\pi/2)$  gates. In each set, the left column shows the experimentally reconstructed PTMs, and the right column shows the difference between the reconstructed PTM and the ideal one.

tary rotations directly from GST. We calculate the predicted SK1 gate PTMs through matrix multiplication of the elementary rotation PTMs,

$$R_{SK1}(\theta, \phi) = SK1_R^-(2\pi)SK1_R^+(2\pi)R(\pi/2),$$

where  $R \in \{X, Y\}$ . Fig. 5.5 presents the results of the analysis above. To generate the error bars on the calculated fidelity metrics, we use a non-parametric bootstrapping technique from pyGSTi. We take the final estimate from running standard GST as the target model for generating non-parametric bootstrapped models and then run gauge optimization on these raw bootstrapped models to generate our final set of models. Error bars are calculated from the standard deviation of average gate fidelity metrics on the set. GST provides information on “Goodness of fit,” i.e., how

well GST estimates the fit to characterize the data, to provide confidence in the data analysis. A rating scale from 1 to 5 summarizes various statistical measures. For both gate sets, the experiments receive a score higher than 4, indicating a good fit.

The noise in the PTMs can be better understood using projections of the gate error generators. These are Linbladian-like operators generated by projecting the error generator into some subspace. We are primarily concerned with the Hamiltonian projection, which produces the coherent error. We use built-in pyGSTi functions to calculate these projections and deduced the amount of overrotation error.

## 5.2 High Fidelity Discrete FM MS Gates

This section contains results from

Ye Wang, Stephen Crain, Chao Fang, **Bichen Zhang**, Shilin Huang, Qiyao Liang, Pak Hong Leung, Kenneth R. Brown, and Jungsang Kim, Phys. Rev. Lett. **125**, 150505 (2020) [30]

### 5.2.1 *Introduction*

The Mølmer-Sørensen (MS) gate [28, 29] is a widely used two-qubit gate with demonstrated fidelities above 99.9% in two-ion systems utilizing axial modes [13, 14]. For practical applications such as digital quantum simulation [44] and fault-tolerant quantum computation [5, 45, 46], the high-fidelity two-qubit gate needs to be extended to all qubits in the system with the ability to address individual qubits.

Individual addressing of atomic qubits in an array to realize qubit control has been accomplished by multi-channel acousto-optic modulators [47, 48], steering beams using acousto/electro-optic modulators [49, 50], and micro-electromechanical system (MEMS) tilting mirrors [51, 38]. For high-fidelity quantum logic gate operations in a larger array of qubits, one must consider the loss of optical phase coherence between individual addressing beams and the crosstalk from an addressing beam

to neighboring qubits that can impact the gate fidelity. Different from the MS gate driven by two global beams, due to the poor optical phase coherence between individual addressing beams, the crosstalk to neighboring qubits from one particular beam has a larger negative impact on the fidelity of the two-qubit gate. Negligible crosstalk has been demonstrated using a MEMS-based individual addressing system [38], and gate schemes that are not sensitive to optical phase drift between the addressing beams have been developed [52, 53, 54] to overcome the fluctuation in optical beam paths among different beams.

Modulated pulse techniques are used to disentangle the internal qubit states from all collective motional modes and increase the robustness against frequency drifts. Amplitude-modulated (AM) gates [55, 56, 47, 48], phase-modulated (PM) gates [57, 58, 59], multitone MS gates [60, 61], and frequency-modulated (FM) gates [62, 63, 64] have been developed and demonstrated. The fidelity of the AM, PM and FM gates demonstrated in a chain of five (or more) ions is around 97% ~ 98.5%, when radial motional modes are used for the gate [47, 48, 59, 62, 64]. Here, we develop the discrete FM gate, which is compatible with simple direct digital synthesizers (DDS) and radiofrequency system on chip (RFSoC).

With an optimized automatic calibration pipeline for the trapped ion system, we demonstrate high-fidelity two-qubit gates in a system with up to 4 ions using a MEMS-based individual qubit addressing system. The two-qubit gate fidelity is 99.49(7)% in a two-ion chain and 99.30(6)% in a four-ion chain. These appear to be the highest two-qubit gate fidelities in systems with the capability of individual addressing reported to date. The residual errors are analyzed and point to future directions for designing a high-fidelity two-qubit gate in longer ion chains.

### 5.2.2 Experimental setups

The qubit is encoded in the hyperfine levels of the  $^2\text{S}_{1/2}$  ground state manifold in a  $^{171}\text{Yb}^+$  ion as  $|0\rangle \equiv |F = 0; m_F = 0\rangle$  and  $|1\rangle \equiv |F = 1; m_F = 0\rangle$  with a qubit frequency splitting of 12.642821 GHz [18], as shown in Fig. 1(a). The qubit coherence time is measured to be more than 1 second using microwave single-qubit operations with a spin-echo pulse. The qubit coherence time can be extended to more than 10 minutes using well-designed dynamical decoupling pulses [65]. The linear chain of  $^{171}\text{Yb}^+$  ions are confined in a microfabricated linear radio-frequency (RF) Paul trap [23] inside an ultra-high vacuum chamber. The two radial trap frequencies are  $\nu_1 = 3.1$  MHz and  $\nu_2 = 2.7$  MHz. The radial principal axes are rotated about  $45^\circ$  to the surface of the trap. The axial trap frequency is 600 kHz and 150 kHz for 2-ion and 4-ion chains with  $5\text{ }\mu\text{m}$  ion spacing, respectively.

The qubits are laser cooled to near the ground state of the radial motional modes and initialized by optical pumping at the start of the experiment. This is followed by the qubit and motional manipulations, driven by stimulated Raman transitions using the beat-note between two orthogonal beams generated from a mode-locked 355 nm picosecond-pulsed laser [26]. The qubits are then measured by state-dependent fluorescence. Photons scattered by each of the qubits are collected by a high numerical aperture lens ( $\text{NA} \approx 0.6$ ) and coupled into individual multi-mode fibers in a fiber array and sent to separate detectors for individual qubit state detection, as shown in Fig. 4.9(c) [66]. Our scheme features negligible detection crosstalk at a level of  $10^{-4}$  in state detection.

The optical setup for implementing Raman quantum gates is schematically illustrated in Fig. 4.9(a) and (b). One of the two orthogonal Raman beams is a global beam with an elliptical profile that illuminates all of the qubits simultaneously. The optical power and beam waist radius of the global beam are 40 mW and  $8\text{ }\mu\text{m} \times$

$110\text{ }\mu\text{m}$ . The other is a pair of tightly focused individual addressing beams that can be independently steered across the qubit chain using a MEMS device. Single-mode photonic crystal fibers are used to deliver the individual addressing beams to the beam-steering system and the global beam to beam-shaping optics [37]. We use acousto-optic modulators (AOMs) to control the frequency, phase and amplitude of all three beams prior to the fibers. Steering of each individual beam is accomplished by a pair of MEMS mirrors each tilting in orthogonal directions. The details of the beam steering system are described in Ref. [38]. A dichroic mirror is used to reflect the Raman beams and transmit the qubit state-dependent fluorescence. The combination of single-mode fiber and MEMS mirrors lead to clean Gaussian beams and low-intensity crosstalk on the neighboring qubits at the level of  $4 \times 10^{-6}$  to  $4 \times 10^{-5}$  with a beam waist radius of  $\sim 2.2\text{ }\mu\text{m}$  and an ion spacing of  $\sim 5\text{ }\mu\text{m}$ . The intensity crosstalk leads to gate crosstalk, which is defined as the ratio of Rabi frequency between the target qubit and the neighboring qubit, at the level of 0.2% to 0.6%. The total number of addressable qubits is  $\sim 11$ , limited by the maximum tilting angle of the MEMS mirrors. A maximum optical power of  $10\text{ mW}$ , a safety limit to avoid degradation from the UV laser, is applied onto the MEMS mirror, which leads to  $1.5\text{ mW}$  addressing beams going into the chamber and a maximum Rabi frequency for the motional sideband transition of  $7\text{ kHz}$ .

### 5.2.3 Discrete FM MS gates

Robust FM MS gates, using a continuous waveform generated by an arbitrary waveform generator (AWG), have been demonstrated in a 5-qubit and a 17-qubit ion chains [62, 64]. To be compatible with DDS, the scheme is reconstituted to its discrete analog. The pulse is designed to be a sequence of equal-time segments, each of which has a constant frequency. The frequencies of the sequence are determined by a numerical optimizer, given the measured radial motional mode frequencies and a

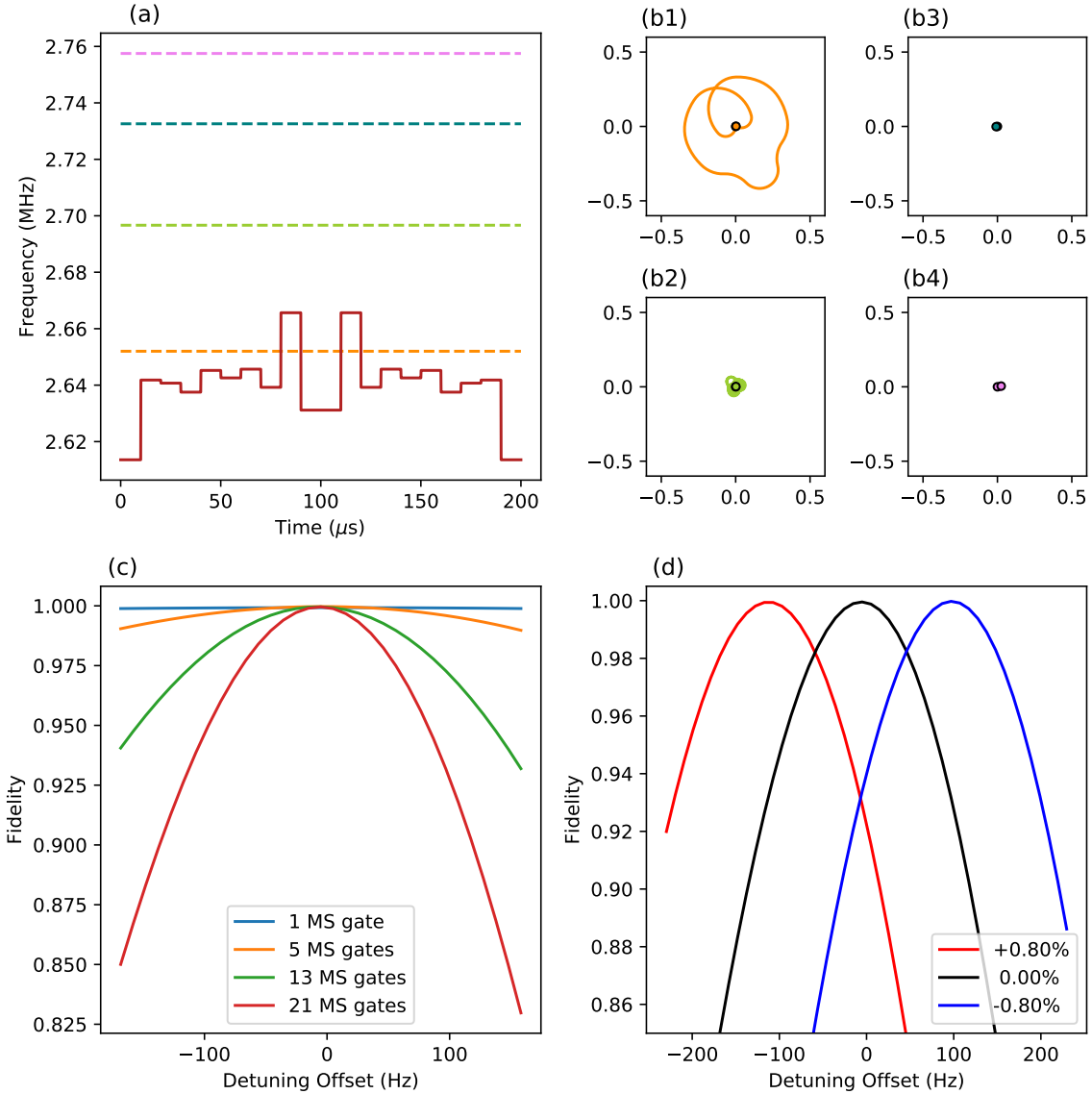


FIGURE 5.6: (a) Discrete frequency modulation pulse sequence in the present experiment. The solution consists of 20 symmetric segments. The total gate time is 200  $\mu$ s. The required sideband Rabi frequencies are 5.55 kHz and 5.47 kHz for FM gates in a 2-ion chain and a 4-ion chain. (b) Phase-space trajectory of four motional modes. (c) The estimated gross gate error of 1, 5, 13, 21 concatenated gates, given different detuning offsets. The estimation includes errors due to residual entanglement between spin and motion and the variation of the rotation angle. (d) The estimated final-state error of 21 consecutive gates with  $\pm 0.8\%$  deviation of Rabi frequency for the motional sideband transition. The amplitude error due to imperfect laser intensity can be compensated by intentional detuning offset.

desired gate time as shown in Fig. 5.6(a). The optimizer generates a pulse sequence that closes the phase-space trajectories of all radial motional modes and therefore disentangles the spins and the motion, as shown in Fig. 5.6(b). It also constrains the Rabi frequency of the motional sideband transitions to be less than 7 kHz.

The detuning error, arising from the drift of motional mode frequencies, leads to unwanted spin-motion entanglement and deviation of the geometric phase for the MS evolution. The error from residual entanglement can be made negligible over  $\pm 1$  kHz detuning error ( $< 2 \times 10^{-5}$ ) in the robust FM gate [62]. The accumulated phase deviation is represented by a deviation of the rotation angle of the gate, which can be considered as an amplitude error. In general, amplitude errors are usually corrected by tuning the laser intensity. However, if the detuning error changes on timescales faster than the time between calibration and the experimental circuit, then the intensity calibration is no longer accurate. Fig. 5.6(c) shows the estimation of final-state fidelity after 1, 5, 13, and 21 consecutive MS gates are applied as a function of detuning offset. The estimation considers both the residual spin-motion entanglement and the deviation of the rotation angle. Taking advantage of the negligible residual spin-motion entanglement against detuning errors in robust FM gates, one can introduce an intentional detuning offset to precisely compensate for the small amplitude error. As shown in Fig. 5.6(d), a  $\pm 100$  Hz detuning offset can compensate roughly  $\mp 0.8\%$  deviation of Rabi frequency for the motional sideband transition.

#### 5.2.4 Calibration pipeline

We designed an automatic calibration process for all critical parameters. The rough calibration is performed every 30 minutes and takes  $\sim 10$  minutes to complete. First, we calibrate the pointing accuracy of the two individual beams by tilting the MEMS mirror and observing the response of the target ion and neighboring ions to the

beams. For each mirror, the tilt angle is calibrated by maximizing the population transfer of the target ion according to a single-qubit  $\pi$  rotation pulse and minimizing the those of the neighboring ions after a single-qubit  $10\pi$  rotation pulse. Next, we address a single ion in the chain and measure all of the mode frequencies by scanning the beat-note frequency and observing the motional sideband transition. The discrete FM solution is calculated based on the measured mode frequencies and the predetermined gate time of 200  $\mu$ s. After loading the resulting pulse sequence to the random access memory (RAM) of a field-programmable gate array (FPGA), the FPGA triggers the frequency updates for the DDS channels in real-time during FM gates [35]. The beam power is calibrated by ensuring the population of target ion in the  $|0\rangle$  state of being 0.5 after an expected  $3.5\pi$  single-qubit rotation.

A final, fine calibration that takes tens of seconds is run just before the experiments to compensate for the small drift of the mode frequency and the laser intensity. As shown in Fig. 5.6(d), the small drift of the laser intensity can be compensated by introducing a detuning offset, which is a more precise method than tuning the laser intensity. This calibration is done by scanning the detuning offset with 21 concatenated gates applied to  $|00\rangle$ . The detuning at which  $|00\rangle$  and  $|11\rangle$  have equal probability indicates the perfect rotation angle for the MS gate. On average, this calibration improves our gate fidelity by about 0.5% compare to just doing the rough calibration.

### 5.2.5 Results

We demonstrate the two-qubit MS gate in a two-ion chain and a four-ion chain. First, we initialize the target qubits to the  $|00\rangle$  state and then apply a sequence of 1,5,13 and 21 MS gates to make the maximally entangled state  $|\psi_+\rangle = (|00\rangle + i|11\rangle)/\sqrt{2}$ . We then extract the state fidelity by measuring the population and the parity contrast [67]. The infidelity due to population leakage and the decrease of

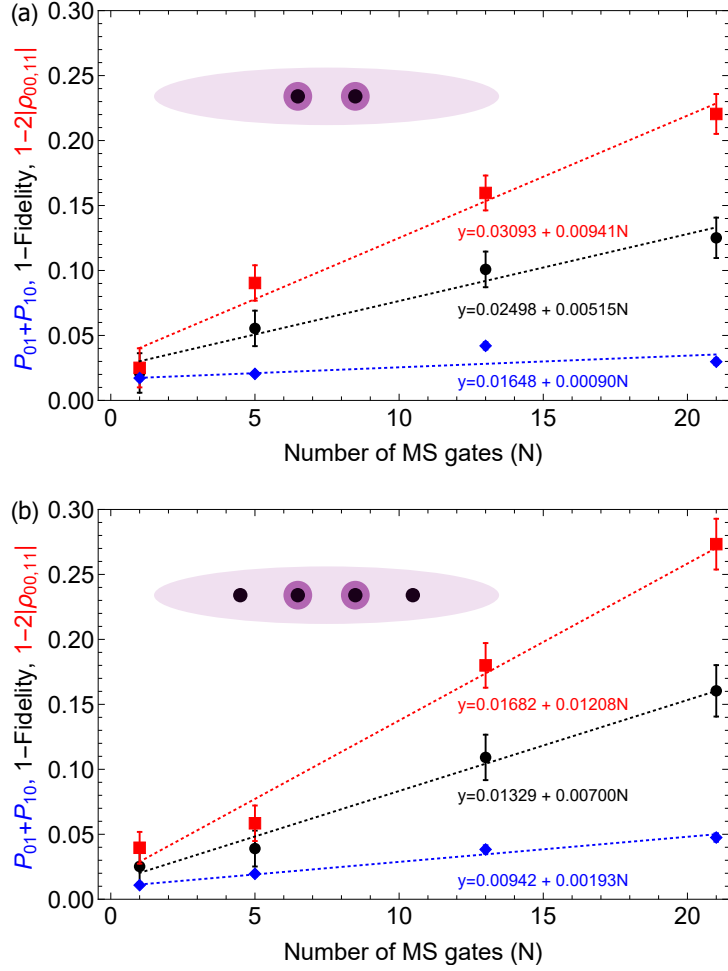


FIGURE 5.7: Infidelity of the entangled state generated by repeated application of MS gates in a **(a)** two- and a **(b)** four-ion chain. The blue diamonds, red squares, and black circles are the population leakage to  $|01\rangle$  and  $|10\rangle$  space, the loss of parity contrast, and the infidelity of the final state, respectively.

the parity contrast is plotted in Fig. 5.7. The stochastic and the coherent error accumulate with concatenated gates in a linear and a quadratic way, respectively. However, the state preparation and measurement (SPAM) error remains constant. Using a linear fit for the data, we can extract the gate fidelity without the SPAM error. The two-qubit gate fidelity is 99.49(7)% in a two-ion chain and 99.30(6)% in a four-ion chain. The data matches a linear fit, indicating that any coherent systematic error is negligible for the two-qubit gate in our system. The  $\approx 2\%$  SPAM

error consists of 1.24% preparation error and 0.98% detection error according to the single-qubit gate gate-set-tomography (GST) analysis [68] performed on the present system. The high SPAM error is due to the limited control bandwidth on DDSs and can be suppressed to less than 0.1% with an updated control system [36].

### 5.2.6 Error analysis

Table 5.1: Mølmer-Sørensen gate error budget. The errors are simulated with the full density matrix using the Master equation, including various error sources. The laser and motional coherence times are measured to be  $83.3 \pm 11.5$  ms and  $36.3 \pm 2.3$  ms, respectively. The beam intensity fluctuation is measured to be 0.8%. The motional heating rate of the center-of-mass mode and the tilt mode in the two-ion chain is measured to be  $\sim 200$  phonons/s and  $< 10$  phonons/s, respectively.

Error source	In 4-ion chain ( $10^{-3}$ )	In 2-ion chain ( $10^{-3}$ )
Laser dephasing	$2.7 \pm 0.4$	$2.7 \pm 0.4$
Motional dephasing	$1.2 \pm 0.1$	$1.1 \pm 0.1$
Raman beam intensity fluctuation	0.16	0.16
Off-resonant coupling	$< 0.3$	$< 0.3$
Motional heating	0.47	0.59
Spontaneous emission	$< 0.25$	$< 0.25$
FM Solution imperfection (due to laser power restriction)	0.76	0.04
Total	$5.84 \pm 0.5$	$5.14 \pm 0.5$

To understand the residual error for the two-qubit gate, we study the impact of various error sources on an ideal two-qubit gate using numerical simulation [29, 13, 14]. The simulated error budget is shown in Table 5.1. Laser dephasing is the leading order effect. We use the optical phase-sensitive gate scheme [53] for our FM gates. This scheme leads to the sensitivities of the laser phase on our FM gates. We measure the laser coherence time with Ramsey interferometry using laser-driven phase-sensitive single-qubit operations. The Rabi frequency of this phase-sensitive operation is affected by motional states of radial modes, as described by the Debye-Waller effect [69, 29]. During the waiting time of Ramsey interferometry, the

motional state is heated from a near ground state to a thermal state due to anomalous heating [70, 71]. The heating rate of the center-of-mass mode and the tilt mode in the 2-ion chain is measured to be  $\sim 200$  phonons/s and  $< 10$  phonons/s, respectively. Therefore, the Ramsey contrast should be amended with the Debye-Waller effect. The corrected Ramsey contrast leads to a laser coherence time of  $83.3 \pm 11.5$  ms. On the other hand, the qubit coherence time is close to 1 second if we use microwave or laser-driven phase-insensitive single-qubit operations for Ramsey interferometry. This significant reduction from 1 second to  $83.3 \pm 11.5$  ms is caused by optical-phase fluctuations of two Raman beams at the qubit location arising from the optical path length variations.

Motional dephasing is the next significant source and has many potential mechanisms [69]. In our system, it is mainly due to the amplitude fluctuation of the RF source used to generate the trapping potential. We apply a Ramsey interferometry to the motional sideband transition to measure the motional coherence time. To avoid the Debye-Waller effect, the measurement is done on the zig-zag mode of a 7-ion chain, which features negligible anomalous heating. The motional coherence time is measured to be  $36.3 \pm 2.3$  ms.

The intensity fluctuation of the tightly focused addressing Raman beams of  $< 0.8\%$  is deduced by observing the decay of Rabi flopping for a phase-insensitive single-qubit gate, driven by a co-propagating pair of Raman beams. The intensity fluctuation of the global beam should be at the same level. The upper bound of the off-resonant coupling to the carrier transition is estimated using the equation in Ref. [29].

#### *5.2.7 Conclusions*

The dominant error sources in our scheme are entirely technical in nature. The fluctuation of the Raman beam path and intensity can be suppressed by better op-

tomechanical design. The noise from the RF source can be suppressed by active feedback on the RF amplitude and better mechanical stability of the helical resonator. We observe UV-induced damage on the MEMS mirrors when the Raman beam power is increased to above 10 mW, so we increase the optical power of the global beam to maintain gate speeds under such power constraint on the individual beams. A faster gate will significantly suppress the error from the laser and the motional dephasing. The error due to spontaneous emission can be suppressed to be less than  $1.7 \times 10^{-4}$  by balancing global and addressing beam intensities. With the achievable laser coherence time ( $\sim 1$  s), motional coherence time ( $\sim 0.5$  s) [13], and negligible spontaneous emission rate [72], a two-qubit gate with fidelities well over 99.9% is possible in a long ion chain.

#### 5.2.8 Performance in a upgraded system

In Sec. 5.2.6, we mention the primary error sources are limited laser dephasing, motional dephasing, and motional heating. After a major system upgrade, the laser coherence time is improved from 83 ms to 334 ms. The improvement is a result of the latest Raman modulation and delivery optics upgrades, which are introduced in Chapter 4. More optical power can be squeezed from the delivery system, and we can run faster MS gates. However, the motional coherence time is reduced to  $\sim 10$  ms. We suspect that the reduction is mainly due to a larger 60 Hz electromagnetic noise in the new laboratory space. The motional heating rate remains the same.

Using the same method in Sec. 5.2.5, we prepare Bell states using consecutive MS gates in a three-ion chain. The error due to population leakage and the decrease of the parity contrast is plotted in Fig. 5.8. We observe a 99.61(3)% gate fidelity. The simulated error budget is listed in Table 5.2.8.

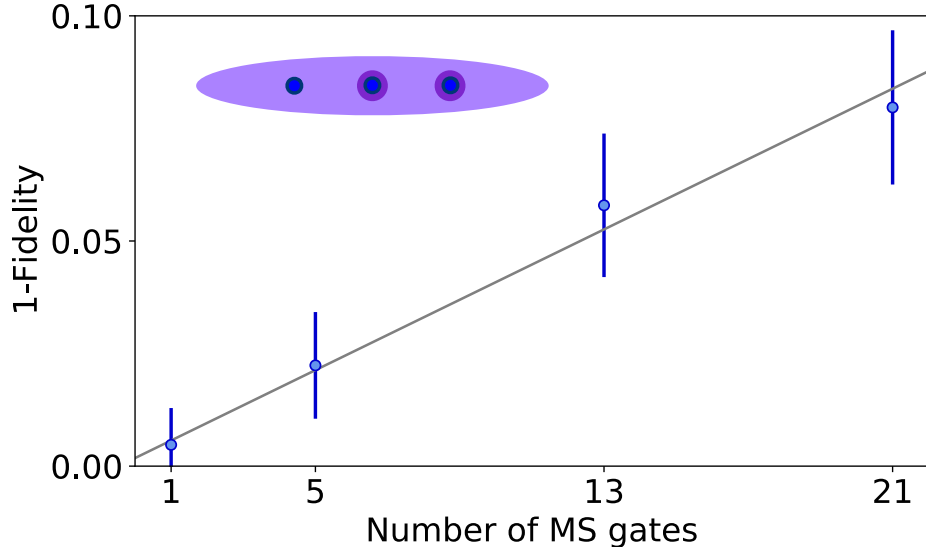


FIGURE 5.8: The error of the Bell state generated by repeated application of MS gates in a three-ion chain. We measure a 99.61(3)% MS gate fidelity and a  $\sim 0.2\%$  SPAM error. This data is taken in an upgraded system with faster gate time (120  $\mu\text{s}$ ) and longer laser coherence time.

Table 5.2: The updated Mølmer-Sørensen gate error budget. Motional dephasing is the leading error source.

Error source	In 3-ion chain ( $10^{-3}$ )
Laser dephasing	$0.4 \pm 0.1$
Motional dephasing	$2.4 \pm 0.1$
Raman beam intensity fluctuation	$< 0.16$
Off-resonant coupling	$< 0.3$
Motional heating	0.35
Spontaneous emission	$< 0.25$
FM Solution imperfection	0
Total	$3.86 \pm 0.2$

### 5.3 High Fidelity Batch-Robust FM MS Gates

This section contains results from

Mingyu Kang, Qiyao Liang, **Bichen Zhang**, Shilin Huang, Ye Wang, Chao Fang, Jungsang Kim, and Kenneth R. Brown, arXiv preprint arXiv:2104.06887 (2021) [73]

### 5.3.1 Introduction

Trapped ion systems are one of the leading candidates for scalable quantum computing platforms [74, 75]. In addition to the near-perfect coherence properties [65, 40] and single-qubit gates with error rates below  $10^{-4}$  [76, 77, 78, 79], trapped ion qubits have significant advantages in entangling gate fidelities. For systems with exactly two ions, state-of-art two-qubit gates reached a fidelity higher than 99.9% by applying state-dependent force with lasers [14, 13] or magnetic field gradients [80]. For larger systems, two-qubit gate fidelities  $> 99\%$  for a four-ion chain [30] and  $> 97\%$  for 13-ion and 17-ion chains [48, 64] have been reported. Trapped ion systems with many qubits are particularly promising as long-range Coulomb interactions between ions lead to all-to-all connectivity between qubits [48, 81].

The central challenge in achieving scalability is to perform high-fidelity entangling gates with a large number of qubits. Entangling gates are performed by briefly exciting the ions' normal modes of motion, which serve as a carrier of quantum information [82, 28]. The driving field should be carefully controlled such that all motional modes are completely disentangled from the internal qubit states at the end of the gate while the qubit states undergo a maximally entangling operation.

In the presence of noise and parameter drifts, pulse design is necessary to achieve fast and robust high-fidelity gates. One approach is to design the amplitudes of multi-chromatic beams that suppress the effect of noise [83, 84, 60, 85, 61, 86]. Another way is to control the amplitude [55, 56, 87, 88, 47, 89], phase [57, 59, 58, 90], and/or frequency [30, 62, 64] modulation over many time segments, which has recently been applied to experiments with many ions [88, 47, 89, 64, 58, 30].

While the methods above lead to analytic robustness by guaranteeing high fidelity up to a certain order [61] for uncertainty in a control parameter, a promising approach is to find the robust pulse numerically using machine learning (ML)-inspired

optimization algorithms. In particular, Ref.[91] shows that training with a large sample set and mini-batches of parameter offsets significantly improves the robustness of the optimized pulse on a generic Hamiltonian with control fields. For trapped ion systems, Ref.[92] demonstrates the application of deep reinforcement learning to robust single-qubit gates.

In this work, we improve on previous discrete and continuous frequency modulation (FM) schemes [30, 62]. We propose two algorithms for FM pulse optimization by training with a large sample set and mini-batches, namely, s(ample)-robust and b(atch)-robust.

### 5.3.2 Robustness conditions

For an ideal MS gate, the qubits should be completely disentangled from the motional states, and the rotation along  $\hat{\sigma}_\phi^{(1)} \otimes \hat{\sigma}_\phi^{(2)}$  axis should reach a  $\pi/4$  angle. The detailed discussion can be found in Sec. 3.3. Hence, the goal of robust FM is to modulate the drive frequency profile  $\delta(t)$  such that  $\alpha_k^j(\tau)$  and  $|\Theta(\tau) - \pi/4|$  are sufficiently minimized, where  $\tau$  is the MS gate time, in the presence of mode frequency offsets  $\epsilon_k$ , i.e.  $\omega_k \rightarrow \omega_k + \epsilon_k$ .

Minimizing  $|\alpha_k^j(\tau)| \propto |\int_0^\tau e^{-i\theta_k(t)} dt|$  is the intuitive criterion for an optimized gate. However, such gate is sensitive to small changes  $\epsilon_k \ll 1/\tau$ . Instead, Ref.[62] induces robustness by minimizing the time-averaged displacement  $|\alpha_{k,\text{avg}}^j| \propto \frac{1}{\tau} |\int_0^\tau \int_0^t e^{-i\theta_k(t')} dt' dt|$ , which is proportional to the first-order correction of  $|\alpha(\tau)|$  when  $\omega_k \rightarrow \omega_k + \epsilon_k$ . Note that a time-symmetric pulse can be used to guarantee that minimizing  $|\alpha_{k,\text{avg}}^j|$  also minimizes  $|\alpha_k^j(\tau)|$ . This optimization scheme, which we call ‘‘robust FM’’, has been used in recent experiments with 4-ion [30] and 17-ion [64] chains. Similar approach with amplitude and phase modulation [90, 58] have also been studied.

Although robust FM is shown to be robust to mode frequency offsets that are an order of magnitude smaller than  $1/\tau$ , it does not guarantee robustness to  $\epsilon_k \lesssim 1/\tau$ .

Moreover, the robustness of the angle  $\Theta(\tau) \approx \pi/4$  to detuning errors is not enforced by this method.

Inspired by the recent work in applying machine learning with large sample sets and mini-batches to quantum control [91], we present “s(ample)-robust” and “b(atch)-robust” FM, which further enhances the robustness of the two-qubit gate. Instead of minimizing the analytic first-order correction, we minimize the average of  $|\alpha_k^j(\tau)|^2$  over an ensemble of offsets, thereby directly incorporating the robustness condition into the cost function. Similarly, we also include the robustness condition of the angle  $\Theta(\tau)$  in our cost function. Note that optimizing robustness of displacement has been achieved to some extent by various methods [60, 61, 58], but not with the additional goal of optimizing robustness of angle <sup>1</sup>, although this is crucial to reach high fidelity in the presence of motional frequency drifts. We find the optimal FM pulse  $\delta(t)$  that minimizes the following cost function  $C_{\mathcal{E}}$ :

$$C_{\mathcal{E}} = \frac{1}{|S_{\mathcal{E}}|} \sum_{\vec{\epsilon} \in S_{\mathcal{E}}} C(\vec{\epsilon}) \quad (5.3)$$

$$C(\vec{\epsilon}) = \sum_k (\alpha_k^{j_1}(\tau, \vec{\epsilon})^2 + \alpha_k^{j_2}(\tau, \vec{\epsilon})^2) + \frac{1}{2} \left( \Theta(\tau, \vec{\epsilon}) - \frac{\pi}{4} \right)^2$$

Here,  $\mathcal{E}$  is the motional frequency uncertainty, and  $S_{\mathcal{E}}$  consists of offset vectors  $\vec{\epsilon}$  whose components  $\epsilon_k$  are independently and randomly drawn from the normal distribution  $\mathcal{N}(0, \mathcal{E})$ .  $\alpha_k^j(\tau, \vec{\epsilon})$  and  $\Theta(\tau, \vec{\epsilon})$  are displacement and angle when  $\omega_k \rightarrow \omega_k + \epsilon_k$ . The two terms of  $C(\vec{\epsilon})$  are simply the displacement error representing residual entanglement with the phonons and the angle error.

The carrier Rabi frequency  $\Omega$  is updated at each iteration such that  $\Theta(\tau, \vec{0}) = \pi/4$ . Since the displacement error is  $\propto \Omega^2$  and angle error is  $\propto \Omega^4$ , this cost function

---

<sup>1</sup> Ref.[60] and supplementary information of Ref.[61] remove the residual entanglement, or the displacement error, up to a certain order in motional frequency offset. However, the rotation angle error is not removed; only its pre-factor of the leading-order term in motional frequency offset is minimized to a non-zero value.

naturally finds the low- $\Omega$  solution. This differs from the robust FM approach, which sets  $\Omega$  after the entire optimization [62], requiring explicit regularization to fit the experimental constraints.

For s-robust FM, we set  $S_{\mathcal{E}}$  as a fixed training set throughout the optimization. For b-robust FM, we set  $S_{\mathcal{E}}$  as a batch, which gets randomly updated at each iteration of the optimization. Therefore, while s-robust FM calculates the cost function repeatedly with a certain set of samples, b-robust FM computes the cost function with a different batch generated from the error distribution throughout the entire optimization. In this work, we set the training set size as 100 for s-robust and batch size as 10 for b-robust. For the batch method, we choose the adaptive moment estimation (ADAM) [93] optimizer to stabilize the gradient during training. We obtain sufficiently good results without hyperparameter tuning. Further details of the numerical analysis can be found in Ref. [73].

### 5.3.3 Experimental results

We compare the experimental results of implementing discrete robust and b-robust FM pulses of length 120  $\mu$ s on a 2-ion chain of  $^{171}\text{Yb}^+$ . The detailed experimental setup is described in Ref.[30]. The RF source for modulating the control lasers has been upgraded from direct digital synthesizers (AD9912) to an RF system on chip (ZCU111) driven by firmware from Sandia National Laboratories [39]. After initializing the qubits to the  $|00\rangle$  state, we apply a sequence of five MS gates, which ideally generates the maximally entangled state  $(|00\rangle + i|11\rangle)/\sqrt{2}$ . To evaluate the effect of motional frequency drifts, we apply pulses with various detuning offsets. Fig. 5.9a, 5.9b show that with b-robust FM,  $|00\rangle$  and  $|11\rangle$  populations deviate from 0.5 more slowly as detuning offset increases, compared to robust FM. Also, the population of unwanted odd-parity states is more suppressed with b-robust pulses. This indicates that b-robust FM is more robust to detuning error than robust FM.

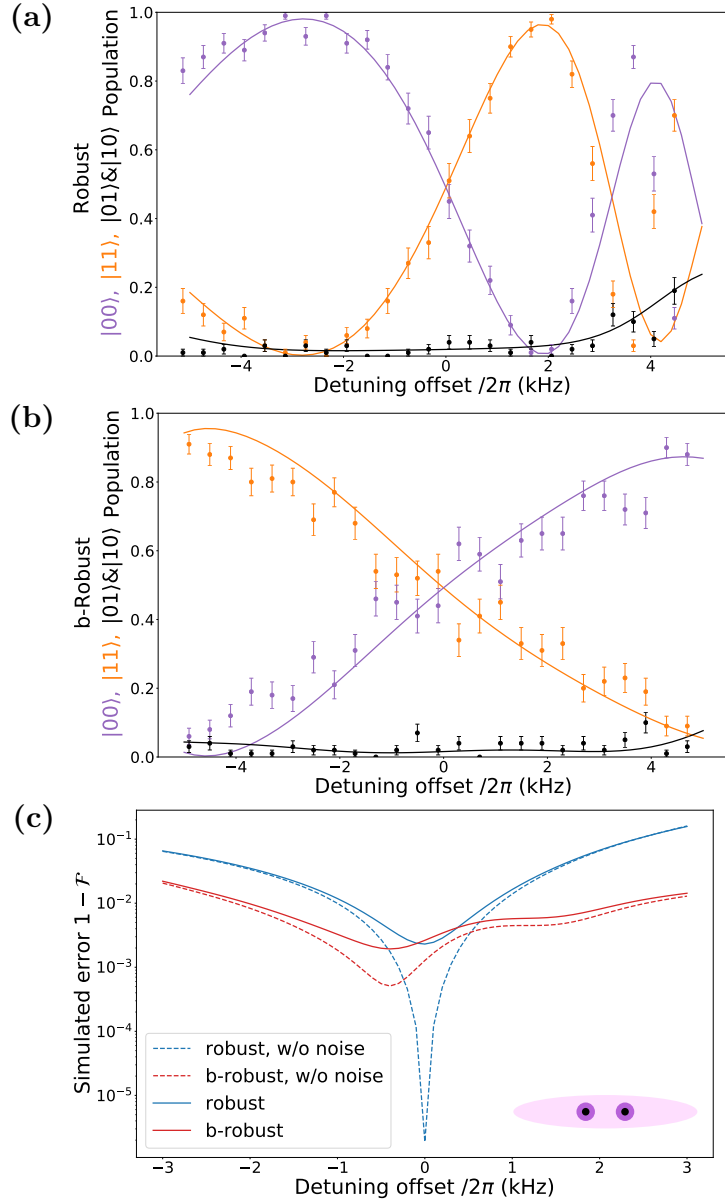


FIGURE 5.9: (a,b) Experimental (points) and simulated (lines) state populations, over a range of detuning offsets, after sequences of five discrete (a) robust and (b) b-robust FM pulses are applied. Error bars represent the shot noise. The smaller slope of even-parity curves and flatter odd-parity curve indicates that b-robust FM is more robust to detuning errors than robust FM. (c) Gate errors averaged over sequences of five gates, simulated with (solid) and without (dashed) dissipative noise. Peak error is lower for b-robust in the presence of noise.

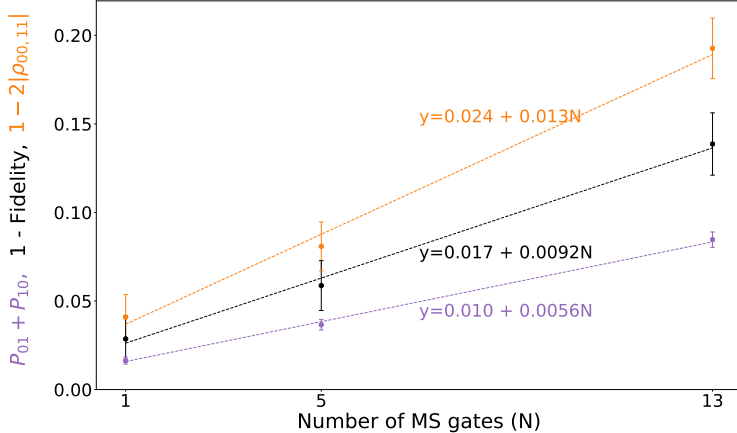


FIGURE 5.10: Experimental errors of the maximally entangled state generated by sequences of repeated MS gates. The purple, orange, and black points represent the population leakage to  $|01\rangle$  and  $|10\rangle$  states, the loss of parity contrast, and the final state error, respectively. Gate error is given by the slope of the black points' linear fit. The same method of gate fidelity estimation is used in Sec. 5.2.5.

Fig.5.9c shows the simulated MS gate errors of discrete robust and b-robust FM, both with and without dissipative noise. Each error is averaged over a sequence of five gates. We use a master equation [32] to simulate MS gate under dissipative noise, which consists of motional dephasing, laser dephasing, and motional heating (see the Supplemental Material of Ref.[30] for details). The noise parameters that describe the current experiment are the following: motional coherence time 8 ms, laser coherence time 333 ms, and motional heating rate 400 quanta/s and 40 quanta/s for center-of-mass mode and tilt mode, respectively. Although the peak gate fidelity of b-robust FM is lower than robust FM without dissipative noise, it is slightly higher (99.81%) than robust FM (99.77%) with the noise. B-robust FM is more robust to slow dephasing noise than robust FM in the presence of motional frequency drifts.

The peak fidelity of b-robust FM occurs at a detuning offset  $-0.4\text{kHz}$ . This is because optimizing over mini-batches does not necessarily set the peak fidelity to be exactly at zero detuning. Simulations with dissipative noise predict that b-robust FM has slightly lower fidelity at zero detuning (99.74%) than robust FM.

Fig. 5.10 shows that the b-robust FM pulse achieves MS gate fidelity 99.08(7)% in the experiment. Note that this is lower than the MS gate fidelity 99.49(7)% reported in Ref.[30], which uses robust FM pulse on the same system. The gate operates at zero detuning, calibrated to the point where the crossover between the populations of  $|00\rangle$  and  $|11\rangle$  states occurs in the experiment described in Fig.5.9b. In future experiments with b-robust FM, the detuning offset should be calibrated to the expected gate fidelity peak. Also, the gate suffers from the high heating rate of the transverse center-of-mass mode and the off-resonant coupling to the motional modes of other directions, which is ignored in the gate pulse design. We expect the gate fidelity to be improved when the trap is operated at a higher RF voltage, which corresponds to higher transverse mode frequency, lower heating rate, and smaller off-resonant coupling. However, the RF voltage in our experiments is currently limited by several malfunctioning electrodes on the surface trap. Although we disable those electrodes, the impedance of the trap changes, and the ions are observed to be unstable when the center-of-mass transverse mode frequency is higher than  $2\pi \cdot 2.1$  MHz.

# 6

## Quantum Circuit Performance Optimization

This chapter contains results from

**Bichen Zhang**, Swarnadeep Majumder, Pak Hong Leung, Stephen Crain, Ye Wang, Chao Fang, Dripto M. Debroy, Jungsang Kim, and Kenneth R. Brown, arXiv preprint arXiv:2104.01119 (2021) [41].

### 6.1 Introduction

Coherent errors are common in quantum computers due to imperfect classical control and parameter drift during the execution of quantum algorithms. Coherent errors can be suppressed by dynamic decoupling [94, 95, 96, 97, 98, 99, 100], composite pulses [101, 102, 103, 78], dynamically-corrected gates [104, 105], or randomized compiling [106], as well as through decoherence-free subspaces [107, 108, 99, 109] and quantum error correction [110, 111, 112, 113]. When we have more information about the structure exhibited by the coherent errors, we can more efficiently suppress them. For many systems, classical control and calibration of the driving fields used to manipulate qubits remain a critical challenge [8]. Fluctuating environmental conditions can lead to slow drifts of system parameters over the course of many experimental

runs.

Here we present a method for canceling coherent errors without requiring any additional gates. We call this method *hidden inverses* because it uses the fact that quantum circuits often contain inverted gates which are hidden due to the common use of self-adjoint unitary operations, for example, the Hadamard ( $H$ ) and controlled-NOT (CNOT) gates. Since these gates are constructed from physical operations, it can be beneficial to choose different pulse sequences. As an example, we could choose  $\text{CNOT}_a = ABC$  or  $\text{CNOT}_b = \text{CNOT}_a^\dagger = C^\dagger B^\dagger A^\dagger$ . The goal is to determine when to implement  $\text{CNOT}_a$ , and when to implement  $\text{CNOT}_a^\dagger$ . This decision will depend on both the intermediate gates and the underlying error models.

## 6.2 Designing gates to control systematic error

For solid-state and atomic quantum systems, quantum gates are performed by applying electromagnetic signals that generate a time-dependent Hamiltonian. For small systems, the advantage of a gate description is questionable and direct optimization of the pulse sequences to optimize the overall evolution is preferable. Gates become a useful abstraction when we consider both larger systems and the challenge of calibration for multiple applications.

Let  $U_0$  be the ideal gate and  $U_a$  be an instance of the gate.  $U_a$  could be a completely positive trace-preserving map, but we invoke the Stinespring dilation to say that all instances of the gate only differ from the ideal gate by a unitary operation that is potentially a larger Hilbert space. We consider both the left and right error operators  $V$ ,  $U_a = U_0 V_{R,a} = V_{L,a} U_0$ . We are interested in the case where  $U_a$  is a good approximation of  $U_0$  and that  $V_R$  and  $V_L$  must be close to the identity.

The system controller does not control the noise but only chooses what signals to apply imperfectly. We further break the unitary label into a control label and an error label  $U_{a,b}$ . The question that we are exploring is whether it makes sense for the

controller to have multiple versions of  $U$  or only a single version and given multiple versions what methods for compilation are.

A very common motif in quantum mechanics and quantum algorithms is a unitary that is transformed by another unitary  $\tilde{W} = UWU^\dagger$ . We should find methods for implementing  $U_a$  and  $U_b^\dagger$  such that averaged over the noise instances  $U_a W U_b^\dagger$  is as close to  $\tilde{W}$ . This will work perfectly, if  $V_{R,a} W V_{L,b}^\dagger = W$ . Ideal cases are when there is no noise and when  $W$  commutes with the  $V$ 's and  $V_{R,a}^\dagger = V_{L,b}^\dagger$ . In many cases,  $W$  itself is a small rotation, and the case that  $V_{R,a}^\dagger = V_{L,b}^\dagger$  will still yield a reduction in error.

Given a quantum circuit with structures  $\tilde{W} = UWU^\dagger$  one can choose the appropriate  $U_a$  and  $U_b^\dagger$  for every  $W$ . We limit ourselves to the case of "hidden inverse" where  $U = U^\dagger$ , which occurs regularly in quantum circuits when operations are conjugated by CNOTs. Our key observation is that in many systems, CNOT is constructed from a series of system-specific gates whose inverses are readily available by changing the sign of the control field. In these cases,  $\text{CNOT}_a$  corresponds to the regular order of gates with the regular control fields, and  $\text{CNOT}_b$  inverts the sequence and inverts the control field. It is the driven Hermitian conjugate of  $\text{CNOT}_a$ . This extends to any unitary, which is self-adjoint.

A commonplace this arises is when multiple CNOTs are used to conjugate a single-qubit rotation to generate a multi-qubit unitary. This structure is common in quantum simulation and quantum optimization algorithms [114, 115]. To generate an  $n + 1$  qubit weight Pauli operation, we can build a circuit that performs a single-qubit  $Z$  rotation whose direction is conditioned on the parity of  $n$  other qubits as

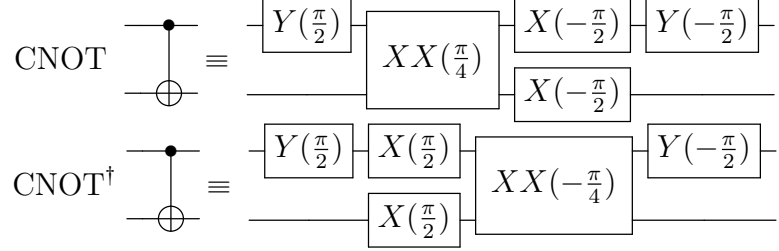


FIGURE 6.1: Standard and Hermitian conjugated decompositions of CNOT gate with native trapped ion quantum operations. Negative rotations are implemented by applying a  $180^\circ$  phase shift in the experiment.

follows:

$$\begin{aligned}
 U &= \prod_{j=1}^n \text{CNOT}_{j,n+1} R_{z,n+1}(\theta) \prod_{j=1}^n \text{CNOT}_{n+1-j,n+1} \\
 &= \exp\left(-i\frac{\theta}{2} \bigotimes_{j=1}^{n+1} Z_j\right).
 \end{aligned} \tag{6.1}$$

The question we are addressing here is whether or not the CNOTs that come before the rotation and the CNOTs that come after the rotation should be the same. At this point, we need to introduce a physical decomposition of the CNOTs and an error model to proceed. We limit ourselves to a model where the entangling operation is generated by a single two-qubit Pauli operator and decorated with single-qubit gates to become the CNOT. It is common for many quantum computing platforms, but for concreteness, we further specialize to an XX-type interaction that is common in Mølmer-Sørensen gates in trapped ions. For this case, the CNOT gate can be performed in either its standard or hidden inverse configurations as displayed in Fig. 6.1. The choice of configuration is non-trivial since CNOT gates are synthesized from a two-qubit gate and multiple single-qubit gates [116], which are subject to systematic overrotations and phase errors in addition to stochastic noise.

In Fig. 6.2(a) and (b) we present circuits which implement the same computation as Eq. 6.1 ( $n = 1$ ) using different choices of CNOT decompositions. These choices

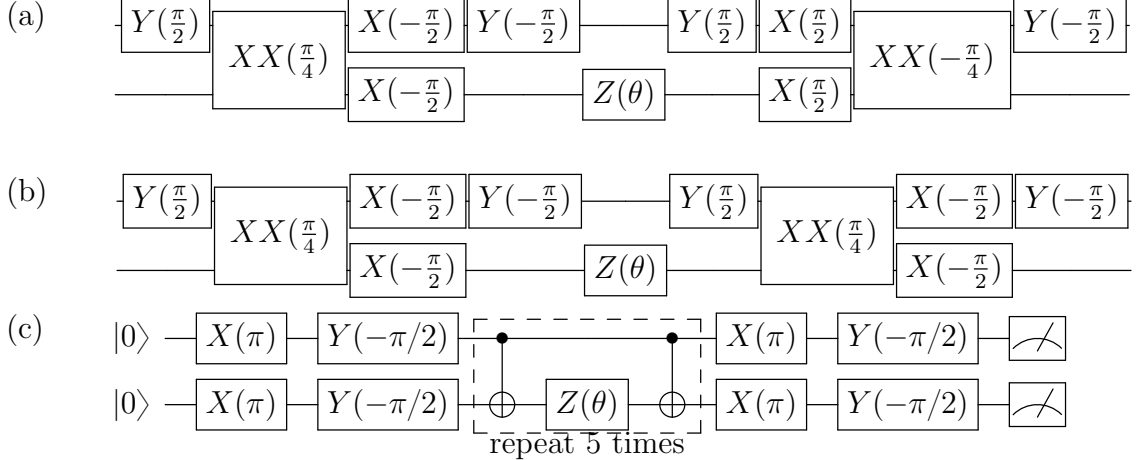
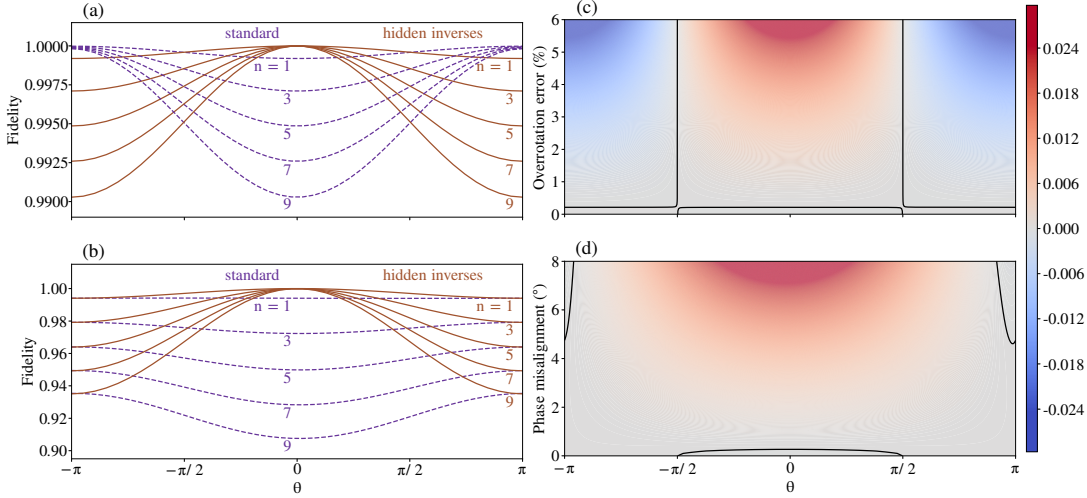


FIGURE 6.2: **Circuit Diagrams** (a) Decomposition of the hidden inverse parity-controlled  $Z$  rotation circuit ( $n = 1$ ) into native gates for trapped-ion qubits where the second CNOT gate has a  $180^\circ$  relative phase shift with respect to the first CNOT gate. (b) Decomposition of the standard circuit into trapped-ion qubit operations where the second CNOT gate is the same as the first one. (c) The experimental circuit for investigating the impact of hidden inverses. The portion of the circuit highlighted by the dashed box is repeated five times in order to amplify the effects of the coherent errors.

impact circuit performance when each gate is subject to overrotation. Fig. 6.3(a) and (b) present the performance of the circuits for  $-\pi < \theta < \pi$ , assuming that every single-qubit and two-qubit gate in the CNOTs only suffers from overrotation errors and from phase misalignment error, respectively.

We observe that the hidden inverse configuration outperforms the standard one considerably when the  $Z(\theta)$  rotation angle is small. This can be understood by noting that a small angle is near the identity, so the systematic errors are approximately canceled. We further note that the oscillatory behavior suggests the need for compilation tools to determine which CNOTs should be inverted in more complex circuits. The amplitude of the oscillation is positively correlated with the number of control qubits.

This behavior is generic and comes from any model where the dominant error of the gates building the CNOTs are overrotations. In any real system, there will be



**FIGURE 6.3: Multi-qubit parity controlled-Z circuit simulated performance**

(a) Average gate fidelities of parity controlled-Z rotation circuits according to Eq. 6.1 with standard (dashed lines) and hidden inverse (solid lines) configurations for 1 to 9 control qubits, with each two-qubit gate subject to 2.0% overrotation and each single-qubit gate subject to 0.2% overrotation. The hidden inverse configuration outperforms the standard one when the absolute value of the  $Z$  rotation angle is less than  $\sim \pi/2$ . (b) Average gate fidelities of parity controlled-Z rotation circuits with 3.5° phase misalignment. The performance of the hidden inverse configuration is higher than or equal to the standard one regardless of  $\theta$ . These shows the scalability of the hidden inverse technique. In (c) and (d), we present the average gate fidelity difference between hidden inverse and standard configuration when  $n = 1$ . The warm color shows the area where the hidden inverse configuration outperforms the standard one. Curves in black represent the boundary where the fidelity difference is zero. When the coherent error is small, fidelities of standard configuration surpass the hidden inverse configuration by  $\sim 10^{-5}$  due to the imperfect motional state coherence.

multiple error types, and the potential advantage can differ. Here we theoretically examine the  $n = 1$  case using a detailed ion trap error model.

We simulate the  $n = 1$  case with more details. Fig. 6.3 (c) presents the performance of the circuits under different overrotation errors. We note that for the simulations shown in Fig. 6.3(c) and (d), we consider all dominant stochastic error sources in our experimental system, including laser dephasing error, motional de-

phasing error, and motional heating. We use the master equation in Lindblad form to simulate the open quantum system. The dominant stochastic error sources are depicted by corresponding collapse operators, while parameter offsets in the Hamiltonian represent the coherent error sources. The stochastic error is why standard configuration outperforms hidden inverse configuration when the relatively small coherent error of interest. However, the fidelity difference is at the level of  $10^{-5}$  for a circuit fidelity differing from one by  $10^{-2}$ , which can not be detected in our current experiment system considering the slow-drifting coherent error.

Besides overrotation error, we find that the hidden inverses configuration also makes the circuit robust to single and two-qubit gate phase misalignment. Two-qubit and single-qubit gates are driven by different fields and mechanisms with the  $Z$  basis usually well defined by the energy eigenbasis of the undriven system Hamiltonian.  $X$  and  $Y$  in the rotating frame simply differ by a phase, and a common experimental challenge is to align the  $X$  in a two-qubit  $XX$  interaction with the single-qubit  $X$  interaction. Fig. 6.3 (d) presents that hidden inverse configuration suppresses phase misalignment in almost all the areas of interest. In the small region where hidden inverse configuration exaggerates the phase misalignment, the fidelity difference is at the level of  $10^{-5}$ . Unlike the robustness over overrotation error, which requires the  $Z(\theta)$  rotation angle to be small, the hidden inverse configuration provides a wide fidelity improvement over phase misalignment error.

### 6.3 Experiment implementation of an arbitrary quantum circuit

In the experiment, a chain of  $^{171}\text{Yb}^+$  ions are trapped in a linear chain  $70\ \mu\text{m}$  above the surface of a microfabricated surface trap made by Sandia National Laboratories. The  $|0\rangle$  and  $|1\rangle$  states of the qubit are encoded in the hyperfine ground states,  ${}^2\text{S}_{1/2}|F=0, m_f=0\rangle$  and  ${}^2\text{S}_{1/2}|F=1, m_f=0\rangle$ , respectively. A  $369.5\ \text{nm}$  laser is used to Doppler cool, EIT cool, and prepare the ions in the  $|0\rangle$  state. State detec-

tion is performed through state-dependent fluorescence by resonantly exciting the  $^2S_{1/2}|F=1\rangle$  to  $^2P_{1/2}|F=0\rangle$  transition and collecting the emitted photons [36, 117]. The scattered photons are imaged with a 0.6 numerical aperture lens and coupled into a linear array of multi-mode fibers with 100  $\mu\text{m}$  diameter cores [66]. Each fiber in the array is connected to individual photomultiplier tubes (PMTs), allowing for individual qubit readout. For the following experiments the Doppler cooling, EIT cooling, state initialization, and state detection take 1 ms, 500  $\mu\text{s}$ , 15  $\mu\text{s}$ , and 300  $\mu\text{s}$ , respectively.

Stimulated Raman transitions using a 355 nm picosecond pulsed laser drive single-qubit and two-qubit gates [69, 118, 53]. An elliptical beam addresses both of the qubits in the chain simultaneously, while two tightly focused beams perpendicular to the elliptical beam individually address the two qubits [38]. Steering of each individual beam over the ion chain is accomplished by a pair of MEMS mirrors, each tilting in orthogonal directions. The number of atomic qubits in our trapped ion quantum processor is limited to 13 by the steering range of the MEMS mirrors. In this experiment, only two  $^{171}\text{Yb}^+$  ions are trapped to prove the principle. The beams pass through acousto-optic modulators (AOMs) driven by the Radio Frequency System on Chip (RFSoC), which provides the ability to change the amplitude, frequency, and phase of each beam. The RFSoC firmware is provided by Sandia National Laboratories QSCOUT project [39]. By controlling the duration of the pulse and the phase of one of the two Raman beams, we can perform arbitrary single-qubit rotations,  $R(\theta, \phi)$ . Two-qubit gates are implemented using the Mølmer-Sørensen (MS) scheme [29]. Discrete frequency modulation (FM) of the Raman beams is performed in order to robustly disentangle the qubit states from all of the motional modes [62, 64, 30]. Further details of the setup can be found in Ref [30].

The universal gate set of our system contains MS ( $XX(\pi/4)$ ) gate,  $X(\pi/4)$  gate, and arbitrary  $Z$  rotations. Arbitrary  $Z(\theta)$  rotations are implemented in a virtual

way by accumulating a  $-\theta$  phase in the following gate operations. Here we examine two-qubit circuits.

We implement the Mølmer Sørensen gate in a spin phase-sensitive configuration [53]. In this configuration, the rotation axis is not exactly aligned with the XX axis due to mechanical fluctuation in the optical path of the Raman beams. We note the intrinsic phase instability and the slight difference of the AC Stack shift between single and two-qubit gates, and it is necessary to calibrate the phase between these gates. We initialize the qubits in  $|00\rangle$  state and implement a  $XX(\pi/4)$  gate on them. Then we apply a single-qubit  $\pi/2$  rotation on both qubits. The phase  $\phi$  of the single-qubit gates is varied from 0 to  $2\pi$ . Finally, both qubits are measured in  $Z$ -basis. When we plot the parity measurement results versus the single-qubit phase  $\phi$ , we obtain a sinusoid,  $\cos(\phi_0 + 2\phi)$ , with a phase offset  $\phi_0$ . In experiments, we observe the phase offset drifts as much as  $4^\circ$  within several hours. Right after calibration, we can reduce the misalignment to as low as  $\sim 0.2^\circ$ .

Due to the limits of our ability to stabilize laser intensity and phase at the ion, we know there will be systematic errors between gates. For single-qubit gates, we use gate set tomography (GST) on both direct quantum pulses and composite quantum pulses to characterize systematic errors. The results of GST infer time-varying overrotations exist in our system. Details of the single-qubit GST experiment can be found in Sec. 5.1.1.

## 6.4 Hidden inverse experimental performance

The base circuit for the hidden inverse experiment is the portion highlighted by the dashed box in Fig. 6.2(c). A CNOT gate is performed followed by a  $Z(\theta)$  rotation on the target qubit [30, 116]. The second CNOT gate is applied either with the same phase as the first (CNOT) or with a phase shift of  $\pi$  relative to the first ( $\text{CNOT}^\dagger$ ). The latter configuration is the hidden inverse case. We reverse the gate sequence

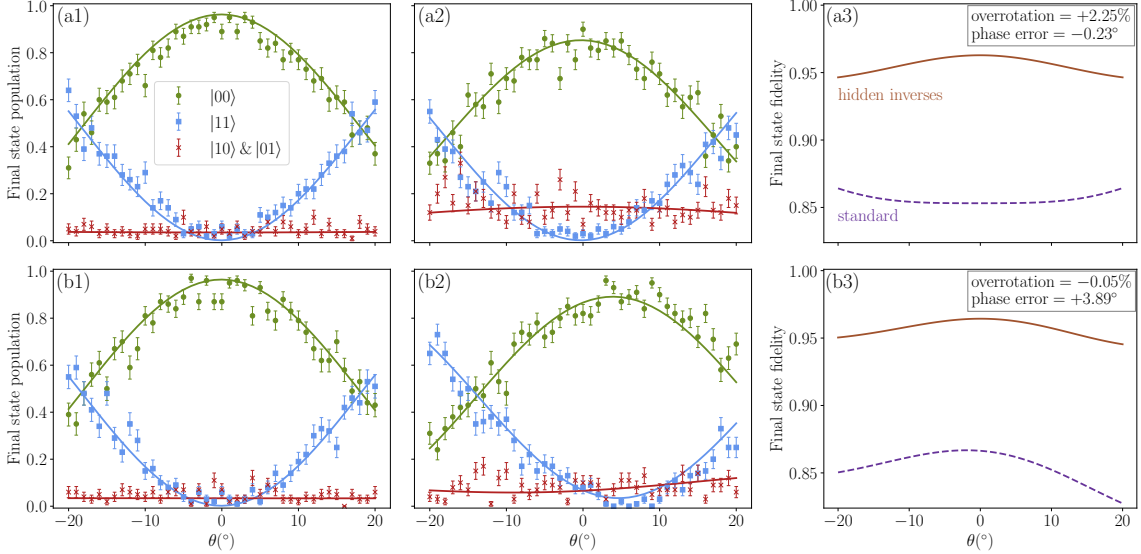


**FIGURE 6.4: Hidden inverses experiment data and simulated final state fidelity** Here we present comparisons of the circuits shown in Fig. 6.2. For the data in the top row, the  $XX(\pi/4)$  gate experiences  $2.25 \pm 0.04\%$  overrotation error. While for the data in the bottom row, a  $3.89 \pm 0.09^\circ$  phase misalignment is introduced to the circuits instead. In (a1) and (b1), we present results for the case where our hidden inverse method is implemented, inverting the second CNOT, while in (a2) and (b2) we present results for the standard case where the CNOT is left unchanged. In these figures the green points represent the population of the  $|00\rangle$  state, the red points represent the  $|01\rangle$  and  $|10\rangle$  state, and the blue points represent the  $|11\rangle$  state. Solid lines show the results of the simulation with the two types of coherent errors, as well as other dephasing errors. The error bars represent the standard error of the data. Figures (a3) and (b3) show the simulated final state fidelity of the circuits with and without hidden inverses. Hidden inverse circuits outperform the original circuits in both conditions.

order and each element gate’s sign in the CNOT decomposition to conform to the Hermitian adjoint’s anti-distributivity. The base circuit is repeated five times to amplify the two-qubit gate overrotation error and phase misalignment error between single-qubit and two-qubit gates, which are the dominant coherent error sources in the circuit. We note that for the repeated circuits, we cannot experimentally distinguish cancellation of CNOT and  $\text{CNOT}^\dagger$  errors across  $Z(\theta)$  with cancellation from the next CNOT. However, the circuit in Fig. 6.2(c) is needed to amplify the

error.

Two separate sets of experiments are conducted to characterize the two-qubit gate overrotations, phase misalignment between single-qubit and two-qubit gate, and the effectiveness of the hidden inverses scheme. In both sets of experiments, the two-qubit gate fidelity is  $\sim 99.4\%$  before injecting the coherent errors. The  $Z(\theta)$  rotation angle is varied. For the first set of experiments, we introduce a  $2.25 \pm 0.04\%$  two-qubit gate overrotation error into the circuits and maintain the phase misalignment as small as possible ( $-0.23 \pm 0.17^\circ$ ). The circuit in Fig. 6.2(c) is implemented with and without the hidden inverses to quantify the suppression of overrotation errors. The system can be seen to suffer from two-qubit overrotation error significantly. Fig. 6.4(a1) shows the probability of detecting the  $|00\rangle$ ,  $|10\rangle$  &  $|01\rangle$ , and  $|11\rangle$  states at the end of the circuit with the hidden inverses, and Fig. 6.4(a2) shows the results without the hidden inverses. The solid lines indicate fitted simulation results with two free variables, the overrotation error of the  $XX$  gates and the phase misalignment between single-qubit and two-qubit gates. When hidden inverses are used, the contrast of the  $|00\rangle$  is improved, and the residual population in the odd parity states is significantly reduced. This indicates suppression of overrotation errors from the  $XX$  gates. Using the theoretical model and fitting results, the final state fidelities of the circuits in both configurations are estimated. As shown in Fig. 6.4(a3), the final state fidelities are improved from approximately 85% to 95% due to the usage of hidden inverses. While the  $Z(\theta)$  rotation angle increases, the improvement results from hidden inverses decreases.

In the second set of experiments, we introduce a phase misalignment error of  $3.89 \pm 0.09^\circ$  and minimize the two-qubit gate overrotation ( $-0.05 \pm 0.22\%$ ). We implement the circuit in both configurations to examine the suppression of phase misalignment errors for the hidden inverse circuit. Fig. 6.4(b1) and (b2) show the results of the circuits with and without hidden inverses, respectively, for the set of

experiments when phase misalignment is dominant. With the hidden inverse configuration, along with the improved contrast of the  $|00\rangle$  population and the reduced odd parity population, the curves regain symmetry about the  $0^\circ Z$  rotation. This shows a correction of the phase misalignment between single-qubit gates and two-qubit gates. Fig. 6.4(b3) represents the estimated final state fidelities of the circuits in both configurations. The fidelities are improved from approximately 84% to 95%. In the case of phase misalignment, we note the improvement from hidden inverses fades away much slower than the case of overrotation error as the  $Z(\theta)$  rotation angle increases.

## 6.5 Alternative methods for reducing systematic errors

Systematic errors can be reduced in a number of ways, and we briefly compare our method with other techniques in the context of the experiment.

### 6.5.1 Two-Qubit SK1 Composite Pulses

Composite pulses developed for single-qubit gates to fix overrotations can be used to reduce overrotations in two-qubit gates using an isomorphism between one qubit Pauli operators and a subgroup of two-qubit Pauli operators [119, 120]. Previous calculations of hidden inverses built from composite two-qubit pulses were shown to greatly reduce circuit error in theory when the only error is gate overrotation [121]. In practice, we have not seen an experimental advantage for these pulses. SK1 adds two additional  $\pi$  Mølmer-Sørensen gates resulting in a gate that is nine times longer.

We numerically consider the implementation of SK1 sequences for Mølmer-Sørensen gate [121] using a simplified error model to understand why these methods do not provide an advantage. The average gate fidelity difference is presented in Fig. 6.5. When we only consider overrotation error (coherent) and motional heating (stochastic), given an overrotation error that is around 1% to 2% a few minutes after laser

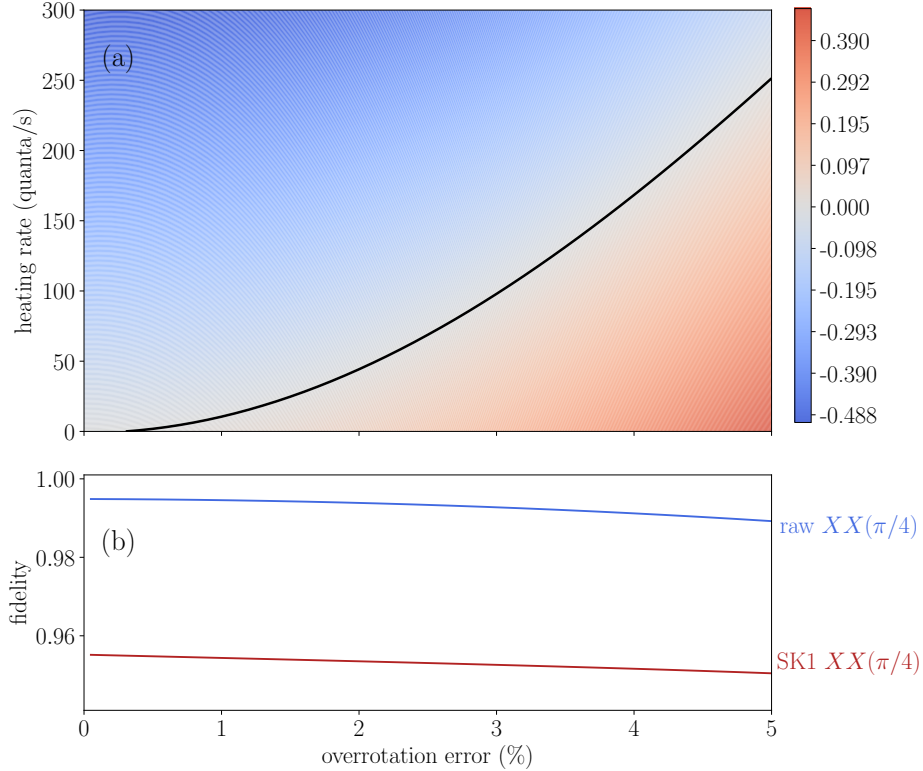


**FIGURE 6.5: SK1 two-qubit gates performance** (a) In the top contour plot, we present the simulation result of the average gate fidelity improvement resulted from SK1 compensate pulses under different overrotation and stochastic error conditions. Warm color represents a fidelity improvement comparing to the raw two-qubit gate, and cool color represents a fidelity degrading. The diagonal curve in black is where the compensate pulses have a neutral impact. (b) We consider all dominant stochastic error sources in our experiment system in the bottom plot, including laser dephasing error, motional dephasing error, and motional heating. Under the actual experimental condition, SK1 two-qubit compensate pulses are not viable even with 5% overrotation error.

intensity calibration, we estimate that the motional heating rate would need to be as low as 20 quanta per second for the SK1 sequence to help. This is one order of magnitude lower than what we see in our systems. When we consider all stochastic and coherent error sources in our system, SK1 sequences severely limit the fidelity, as shown in Fig. 6.5(b).

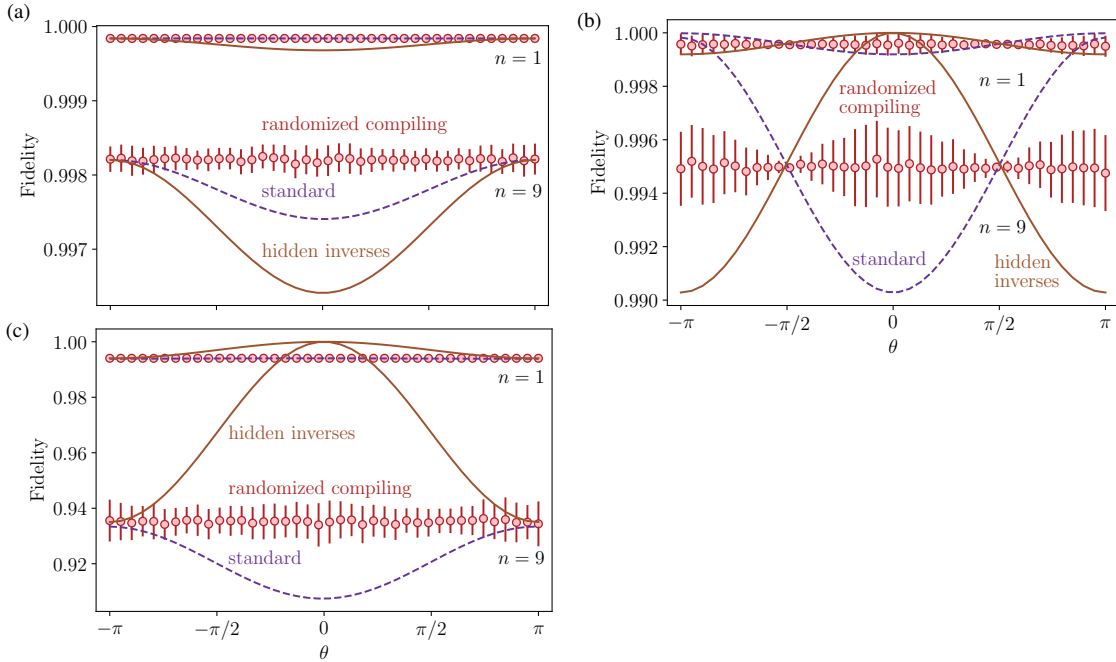


**FIGURE 6.6: Randomized compiling protocol performance.** The average gate fidelity comparison among randomized compiling, hidden inverses, and standard configurations. The results are generated by unitary operator simulations where the error mode is (a) two-qubit gates with 1% detuning error, (b) two-qubit gates with 2% overrotation error and single-qubit gates with 0.2% overrotation error, and (c) 3.5° phase misalignment between single and two-qubit gates.

### 6.5.2 Randomized Compiling

Randomized compiling (RC) [106] is a protocol for converting coherent errors into stochastic errors. RC introduces independent random single-qubit gates into a circuit such that in the absence of noise, the overall ideal unitary remains the same. In the presence of noise, RC twirls the error channel into a stochastic Pauli channel. As a result, RC compiled circuits improve worst-case cumulative errors, and their algorithmic performance can be predicted from randomized benchmarking like protocols.

In order to compare the performance of our hidden inverses protocol with randomized compiling, we numerically simulate each protocol on unitaries from Eq. 6.1

under three different noise models: detuning error, overrotation error, and phase misalignment. In the RC protocol, we sample 100 equivalent circuits for each value of  $\theta$  (in  $RZ(\theta)$ ) from Eq. 6.1) and calculate the average gate fidelity of this ensemble. This average gate fidelity comparison is presented in Fig 6.6. We find that the hidden inverse configuration outperforms RC under overrotation error and phase misalignment, showed in Fig. 6.6(b) and (c). Fig. 6.6 (a) shows that RC outperforms hidden inverses when detuning error dominants. It is because the orientation of detuning error does not invert when the gate orientation changes. Detuning errors in Mølmer Sørensen gates come from inaccurate ac Stark shift calibration. With frequency-modulated gate sequences, ac Stark shift only has a fourth-order error which can be safely ignored after proper calibration.

### 6.5.3 Hardware Specific Compilation

Hidden inverses are developed in the context of a gate model of quantum computation. These gates need to be mapped onto a physical system, and there are multiple software and hardware layers between the user and the device. As a result, the quantum computer operator often prefers to compiling any algorithm to the most hardware efficient form to yield the highest overall fidelity.

In our example circuit, the multi-qubit parity controlled Z rotation, Eq. 6.1, there are many hardware-specific ways to generate the same functionality. A clear example is the base  $n = 1$  circuit of a Z-rotation by angle  $\theta$  surrounding by two CNOTs composed of two  $XX(\pi/4)$ . This can be replaced by a single  $XX(\theta/2)$  gate surrounded by single-qubit gates. Given that two-qubit gates are typically noisier than single-qubit gates, this transformation is experimentally useful for quantum systems with Ising-type two-qubit couplings from nuclear magnetic resonance [122] to trapped ions[123]. The cost here is that one needs to calibrate the two-qubit gate for multiple angles, which is inherently more error-prone than the control of the  $Z$

rotation, which is only advancing a digital phase in experiments. We recognize that calibration may be less of a concern for near-term variational algorithms given the mismatch between algorithm performance at an ideal angle versus the programmed angle [124].

For  $n > 1$ , the additional CNOTs could still benefit from hidden inverses, even if we change the internal primitive. In some ion trap systems [125], the natural two-qubit interaction is a global Mølmer- Sørensen. In this case, there could be a further reduction of the time complexity of the overall procedure. We have not considered this case in detail since our micro-mirror system is not compatible with a global Mølmer-Sørensen gate.

#### 6.5.4 Total optimization

Finally, various noise adaptive compilers have been proposed recently in the literature. They range from aggregation of multiple logical operations into larger units [126], mapping & optimization of high-level quantum programs based on hardware specifications [127] to using machine learning & variational algorithms to develop noise aware circuit learning [128], [129]. While ideas in these protocols are novel and outperform standard compilers for near-term devices with a few qubits and shorter depths, they are not expected to scale efficiently to be useful in large-scale fault-tolerant machines. On the other hand, hidden inverses take advantage of local optimization and could be efficiently added as part of a compiler routine for large-scale quantum systems.

## 6.6 Conclusions and outlook

Slowly varying experimental noise sources can either be corrected by frequent calibrations or by introducing circuit-level protections such as composite pulses and hidden inverses. Gate set tomography reveals that SK1 sequences outperform pre-

dictions based on the individual pulses that compose them. This implies that while there is a long-term drift in the system, composite pulses can effectively cancel out that drift. By taking advantage of gates with self-adjoint, we can compile a circuit to cancel out coherent errors as long as the drift occurs at a timescale slower than the time between the two gates. We have shown a reduction of overrotations and phase misalignment for CNOT gates in a trapped-ion-based architecture. Overall, these low-cost circuit compilation schemes provide a robust platform for reducing systematic error and have already been shown theoretically to provide an advantage for quantum chemistry circuits [130].

Hidden inverses can be applied to any system where the gates are derived from flexible pulse control. We also note that hidden inverses can be expanded to be not-true inverses but only inverses on subspaces. We can reconsider the cancellation of coherent errors in stabilizer measurements by stabilizer slicing [110] as noting a hidden inverse on the subspace. Furthermore, it shows the utility of having multiple versions of the same basic gate for improving circuit performance in the presence of systematic errors.

# 7

## Conclusions

### 7.1 Conclusions

This thesis shows the efforts for performing quantum circuits with high quality on a trapped-ion quantum computing platform. The results are introduced in a bottom-to-top structure: high-quality qubit preparation and measurement, high-fidelity quantum gates, and high-fidelity quantum circuits. Although the experiments are conducted with trapped ions in this thesis, the principles and ideas can be transplanted to other scalable quantum systems, such as superconducting circuits and Rydberg atoms.

Understanding the strength and weakness of an engineered quantum system is a prerequisite to any contribution towards a better system. As one of the most mature quantum computing platforms, trapped ions provide almost perfect individual qubits with developed preparation and measurement techniques. The glory age of exploring physics behind ion trapping may have faded away, especially for trapped Ytterbium ions, but there is room to improve reliability and precision. Chapter 2 and Chapter 4 presents the work on how we polish the existing techniques with proper engineering.

For example, the ultra-stable beam modulation and delivery system stays aligned for months with a precision of a few microns. The system performance, such as laser coherence time, improves, and in the meanwhile, researchers are freed from daily optical alignment tasks and have more time to think at a higher level. It suggests a path for other laser-based quantum computing platforms which wish to step out of laboratories of research institutes.

The experimental control system is built to polish the strengths of trapped ions and further improve system performance. Since trapped ions are provided with ultra-long  $T_2^*$  [65, 40] and relatively slow gate times comparing to superconducting circuits and Rydberg atoms, we prefer DDS/RFSoC than AWG so that one may conduct longer quantum circuits. The control system is also built in a way that possesses the potential of conducting intermediate measurement, which is critical for implementing quantum error correction (QEC). Let us consider the noises in the frequency domain. The ones with high frequencies are considered stochastic errors by the qubits, and they are suppressed by proper engineering. The noises with low frequencies are considered coherent slow drifts by the qubits, and they can be treated with active control. Besides the regular laser frequency stabilization, we perform active stabilization on various parameters: beam intensities, trap RF amplitudes, pulsed laser repetition rate, etc. The tailored control system facilitates not only high-quality qubit manipulations but also reliable ones.

Entangling gates with fidelity above 99.9% have been demonstrated in two-ion chains using axial motional modes [13, 14, 12]. However, scalable 99.9%+ fidelity entangling gates in larger trapped ion systems have not been demonstrated in experiments. The work in Chapter 3 and Chapter 6 provides a way of achieving high fidelity entangling gates using radial motional modes, which is in principle a more scalable approach than axial-mode gates. In Ref. [30], we demonstrate MS gates with 99.5% and 99.3% fidelities in a two-ion and a four-ion chains, respectively. Fol-

lowing the same approach, we have recently pushed the fidelity to 99.7% and 99.2% in a three-ion and five-ion chains, respectively. One of the most critical challenges of achieving high fidelity quantum operations is identifying different types of errors in the system. Error analysis tools, both in experiments and in numerical simulations, are introduced in this thesis.

Coherent gate errors are a concern in many proposed quantum computing architectures. Such errors in single-qubit gates can be suppressed by composite pulse sequences effectively. However, similar techniques are less viable for two-qubit gates because stochastic errors play a significant role in their error budgets. For the work in Chapter 6 we proposed a low-cost quantum circuit compilation technique called hidden inverses that creates circuits robust to overrotation and phase errors. The technique is demonstrated to be effective both in a two-qubit and a five-qubit trapped-ion system. The idea of hidden inverses can be applied to any system where the user has access to low-level pulse design.

## 7.2 Outlooks

Comparing to another leading technology for large-scale quantum computing, superconducting circuits, the bottleneck of trapped ion platforms is scalability. At the time when I started writing this thesis, superconducting circuits platforms featured 53 [10] and 66 qubits [11] have been demonstrated, while the number of qubits in trapped ion platforms is limited at a level of  $\sim 30$ s. Ideas have been proposed to overcome the obstacle.

Quantum CCD architecture for trapped ions has been demonstrated, and it has the potential to push the number of qubits beyond 1000 [131, 15]. In QCCD architecture, mobile ions are used as qubits. The ion qubits are shuttled between interaction zones and storage zones. Therefore, the demonstrated high fidelity operations in small ion crystals maintain. Meanwhile, the total number of qubits can be extended

without a surge of error rate.

The first requirement of the QCQD architecture is sympathetic cooling. Even if the ions are not shuttled during the time of a circuit, operation fidelity is downgraded when the motional states are heated up to high  $\bar{n}$  thermal states. Shutting the ion by using dynamic trapping electrodes makes motional heating deteriorates. The choice of coolant ions and the mixed ion-chain arrangement influence the cooling effect significantly. Therefore, there is further work required to find a general method to optimize the sympathetic cooling scheme for different ion isotopes and length of ion chains.

To further extend the scale of trapped-ion quantum computing platforms, we need coupling between different vacuum chambers. A promising medium is photons, and coupling of a single ion to an optical cavity has been demonstrated using  $^{40}\text{Ca}^+$  [132]. Therefore, realizing ion-photon coupling with  $^{171}\text{Yb}^+$  and  $^{133}\text{Ba}^+$  is an important and promising project in our lab at Duke.

The  $1/r$  Coulomb interaction is the foundation of current trapping and entangling technology. This strong interaction is perfect for trapping ions at desired locations; however, it remains debated whether it is too long-range. Being charged particles, ions' Coulomb interaction always presents. It requires complicated classical control when the number of ions in a single crystal scales up. In a long ion chain trapped in an inharmonic potential, precise measurement of motional modes coupling strengths is still challenging. Different motional mode coupling strengths undermine the advantage from the identical character of atomic qubits to some extent. Inspired by the recent progress in Rydberg atoms, I believe Rydberg ions are an approach that is worth exploring [133, 134, 135, 136]. Rydberg ions possess a long trapping lifetime and adjustable coupling at the same time. It is convenient for extending to large-scale systems by using adjustable Rydberg interaction instead of always-present long-range Coulomb interaction.

Lastly, QEC is a requisite for any ultimate quantum computing platform. Small-size QEC code has been demonstrated in trapped ions [137, 138]. Although trapped ions are leading the QEC race now, more theoretical efforts on trapped-ion-tailored fault-tolerant quantum computation schemes are required. By knowing the leading error type, the code distance and fault-tolerant threshold of a tailored QEC code can be significantly better than the standard one's [139, 140].

# Appendix A

## Two-dimensional Motional State Reconstruction

This chapter contains results which are simple extensions of Ref. [141], while they are useful for motional states determination where two motional modes are involved. Here we refer the number of dimensions as to the number of motional modes, which is not the dimension of Hilbert space.

To reconstruct the two-dimensional density matrix  $\rho$ , similar to what Leibfried et al. did for one-dimensional motional states in Ref. [141], we define

$$\begin{aligned} Q_{k_x k_y}(\alpha, \beta) &= \langle k_x | \langle k_y | D_x^\dagger(\alpha) D_y^\dagger(\beta) \rho D_y(\beta) D_x(\alpha) | k_y \rangle | k_x \rangle \\ &= \frac{1}{k_x! k_y!} \langle 0 | \langle 0 | a_x^{k_x} a_y^{k_y} D_x^\dagger(\alpha) D_y^\dagger(\beta) \rho D_y(\beta) D_x(\alpha) a_x^{\dagger k_x} a_y^{\dagger k_y} | 0 \rangle | 0 \rangle, \end{aligned} \quad (\text{A.1})$$

where  $D_x(\alpha)$  and  $D_y(\beta)$  are displacement operators of mode  $x$  and mode  $y$ . Using the relation  $D^\dagger(\alpha)aD(\alpha) = a + \alpha$  and  $D(\alpha)aD^\dagger(\alpha) = a - \alpha$  repeatedly, we have

$$Q_{k_x k_y}(\alpha, \beta) = \frac{1}{k_x! k_y!} \langle \alpha | \langle \beta | (a_x - \alpha)^{k_x} (a_y - \beta)^{k_y} \rho (a_x^\dagger - \alpha^*)^{k_x} (a_y^\dagger - \beta^*)^{k_y} | \beta \rangle | \alpha \rangle. \quad (\text{A.2})$$

Now we substitute the coherent state  $|\alpha\rangle$  with  $e^{-\frac{|\alpha|^2}{2}} \sum_{n=0}^{\infty} \frac{\alpha^n}{\sqrt{n!}} |n\rangle$ , and further we

obtain:

$$Q_{k_x k_y}(\alpha, \beta) = \frac{1}{k_x! k_y!} e^{-|\alpha|^2 - |\beta|^2} \sum_{n_x, n_y, n'_x, n'_y=0}^{\infty} \frac{(\alpha^*)^{n_x}}{\sqrt{n_x!}} \frac{(\beta^*)^{n_y}}{\sqrt{n_y!}} \frac{(\alpha)^{n'_x}}{\sqrt{n'_x!}} \frac{(\beta)^{n'_y}}{\sqrt{n'_y!}} \cdot \langle n_x | \langle n_y | (a_x - \alpha)^{k_x} (a_y - \beta)^{k_y} \rho(a_x^\dagger - \alpha^*)^{k_x} (a_y^\dagger - \beta^*)^{k_y} | n'_y \rangle | n'_x \rangle.$$

According to Binomial expansion, we can expand the equation above.

$$\begin{aligned} (a_x - \alpha)^{k_x} &= \sum_{j_x=0}^{k_x} \binom{k_x}{j_x} a_x^{j_x} (-\alpha)^{k_x - j_x} \\ (a_x^\dagger - \alpha^*)^{k_x} &= \sum_{j'_x=0}^{k_x} \binom{k_x}{j'_x} a_x^{\dagger j'_x} (-\alpha^*)^{k_x - j'_x} \\ (a_y - \beta)^{k_y} &= \sum_{j_y=0}^{k_y} \binom{k_y}{j_y} a_y^{j_y} (-\beta)^{k_y - j_y} \\ (a_y^\dagger - \beta^*)^{k_y} &= \sum_{j'_y=0}^{k_y} \binom{k_y}{j'_y} a_y^{\dagger j'_y} (-\beta^*)^{k_y - j'_y} \\ Q_{k_x k_y}(\alpha, \beta) &= \frac{1}{k_x! k_y!} e^{-|\alpha|^2 - |\beta|^2} \sum_{n_x, n_y, n'_x, n'_y=0}^{\infty} \sum_{j_x, j'_x=0}^{k_x} \sum_{j_y, j'_y=0}^{k_y} \frac{(\alpha^*)^{n_x}}{\sqrt{n_x!}} \frac{(\beta^*)^{n_y}}{\sqrt{n_y!}} \frac{(\alpha)^{n'_x}}{\sqrt{n'_x!}} \frac{(\beta)^{n'_y}}{\sqrt{n'_y!}} \cdot \\ &\quad \cdot \binom{k_x}{j_x} \binom{k_x}{j'_x} \binom{k_y}{j_y} \binom{k_y}{j'_y} \cdot \sqrt{\frac{(n_x + j_x)!}{n_x!}} \sqrt{\frac{(n_y + j_y)!}{n_y!}} \cdot \\ &\quad \cdot \sqrt{\frac{(n'_x + j'_x)!}{n'_x!}} \sqrt{\frac{(n'_y + j'_y)!}{n'_y!}} (-\alpha)^{k_x - j_x} (-\beta)^{k_y - j_y} \cdot \\ &\quad \cdot (-\alpha^*)^{k_x - j'_x} (-\beta^*)^{k_y - j'_y} \rho_{n_x + j_x, n_y + j_y, n'_x + j'_x, n'_y + j'_y} \end{aligned}$$

$$\begin{aligned}
&= \frac{1}{k_x! k_y!} e^{-|\alpha|^2 - |\beta|^2} |\alpha|^{2k_x} |\beta|^{2k_y} \sum_{n_x, n_y, n'_x, n'_y=0}^{\infty} \sum_{j_x, j'_x=0}^{k_x} \sum_{j_y, j'_y=0}^{k_y} (-1)^{-(j_x + j_y + j'_x + j'_y)} \cdot \\
&\quad \cdot \frac{(\alpha^*)^{n_x - j'_x}}{n_x!} \frac{(\beta^*)^{n_y - j'_y}}{n_y!} \frac{(\alpha)^{n'_x - j_x}}{n'_x!} \frac{(\beta)^{n'_y - j_y}}{n'_y!} \binom{k_x}{j_x} \binom{k_x}{j'_x} \binom{k_y}{j_y} \binom{k_y}{j'_y} \cdot \\
&\quad \cdot \sqrt{(n_x + j_x)!(n_y + j_y)!(n'_x + j'_x)!(n'_y + j'_y)!} \rho_{n_x+j_x, n_y+j_y, n'_x+j'_x, n'_y+j'_y}
\end{aligned}$$

To determine different matrix elements, we displace the state along a circle in both mode  $x$  and mode  $y$ . Let us assume we select  $2N$  different displacement operators for each mode, then we have  $4N^2$  different combinations of displacement on two modes.

$$\begin{aligned}
\alpha_p &= |\alpha| \exp[i(\pi/N)p] \\
\beta_q &= |\beta| \exp[i(\pi/N)q] \\
p, q &\in \{-N, -N+1, \dots, N-1\}.
\end{aligned}$$

After performing a discrete Fourier transformation, Eq. A.1 becomes:

$$\begin{aligned}
Q_{k_x, k_y}^{(l_x, l_y)} &= \frac{1}{4N^2} \sum_{q=-N}^{N-1} \frac{1}{k_x! k_y!} e^{-|\alpha|^2 - |\beta|^2} |\alpha|^{2k_x} |\beta|^{2k_y} \sum_{n_x, n_y, n'_x, n'_y=0}^{\infty} \sum_{j_x, j'_x=0}^{k_x} \sum_{j_y, j'_y=0}^{k_y} \cdot \\
&\quad \cdot (-1)^{-(j_x + j_y + j'_x + j'_y)} \frac{|\alpha|^{n_x - j'_x}}{n_x!} \frac{(|\beta| \exp[-i(\pi/N)q])^{n_y - j'_y}}{n_y!} \cdot \\
&\quad \cdot \frac{|\alpha|^{n'_x - j_x}}{n'_x!} \frac{(|\beta| \exp[i(\pi/N)q])^{n'_y - j_y}}{n'_y!} \cdot \exp[-il_y(\pi/N)q] \cdot \\
&\quad \cdot \binom{k_x}{j_x} \binom{k_x}{j'_x} \binom{k_y}{j_y} \binom{k_y}{j'_y} \cdot \\
&\quad \cdot \sqrt{(n_x + j_x)!(n_y + j_y)!(n'_x + j'_x)!(n'_y + j'_y)!} \rho_{n_x+j_x, n_y+j_y, n'_x+j'_x, n'_y+j'_y} \cdot \\
&\quad \cdot \sum_{p=-N}^{N-1} \exp[-i(\pi/N)p(l_x - n_x + j'_x + n'_x - j_x)].
\end{aligned}$$

Assume  $n_x + j_x = m_x$ ,  $n'_x + j'_x = m'_x$ ,  $n_x = m_x - j_x$ ,  $n'_x = m'_x - j'_x$ , we obtain:

$$\begin{aligned}
Q_{k_x, k_y}^{(l_x, l_y)} &= \frac{1}{4N^2} \frac{1}{k_x! k_y!} e^{-|\alpha|^2 - |\beta|^2} |\alpha|^{2k_x} |\beta|^{2k_y} \sum_{n_x, n_y, n'_x, n'_y=0}^{\infty} \sum_{j_x, j'_x=0}^{k_x} \sum_{j_y, j'_y=0}^{k_y} \cdot \\
&\quad \cdot (-1)^{-(j_x + j_y + j'_x + j'_y)} \frac{|\alpha|^{n_x - j'_x}}{n_x!} \frac{|\beta|^{n_y - j'_y}}{n_y!} \frac{|\alpha|^{n'_x - j_x}}{n'_x!} \frac{|\beta|^{n'_y - j_y}}{n'_y!} \cdot \\
&\quad \cdot \sum_{q=-N}^{N-1} \exp[-i(\pi/N)q(l_y - m_y + m'_y)] \cdot \\
&\quad \cdot \binom{k_x}{j_x} \binom{k_x}{j'_x} \binom{k_y}{j_y} \binom{k_y}{j'_y} \cdot \\
&\quad \cdot \sqrt{(n_x + j_x)!(n_y + j_y)!(n'_x + j'_x)!(n'_y + j'_y)!} \rho_{n_x + j_x, n_y + j_y, n'_x + j'_x, n'_y + j'_y} \cdot \\
&\quad \cdot \sum_{p=-N}^{N-1} \exp[-i(\pi/N)p(l_x - m_x + m'_x)].
\end{aligned}$$

Only if  $m_x = l_x + m'_x$ ,  $m_y = l_y + m'_y$ , the sum over  $p$  and the sum over  $q$  are not zero.

Since  $n_x = m_x - j_x > 0$ ,  $j_x < l_x + m'_x$ , we obtain the following equation:

$$Q_{k_x, k_y}^{(l_x, l_y)} = \sum_{m'_x \in \max(0, -l_x)}^{\infty} \sum_{m'_y \in \max(0, -l_y)}^{\infty} \gamma_{k_x, m'_x, k_y, m'_y}^{(l_x, l_y)} \rho_{(l_x + m'_x), (l_y + m'_y), m'_x, m'_y}$$

where

$$\begin{aligned}
\gamma_{k_x, m'_x, k_y, m'_y}^{(l_x, l_y)} &= \frac{e^{-|\alpha|^2 - |\beta|^2} |\alpha|^{2k_x} |\beta|^{2k_y}}{k_x! k_y!} \sum_{j_x=0}^{\min(k_x, m'_x + l_x)} \sum_{j'_x=0}^{\min(k_x, m'_x)} \sum_{j_y=0}^{\min(k_y, m'_y + l_y)} \sum_{j'_y=0}^{\min(k_y, m'_y)} \\
&\quad |\alpha|^{l_x + 2(m'_x - j_x - j'_x)} |\beta|^{l_y + 2(m'_y - j_y - j'_y)} (-1)^{-(j_x + j_y + j'_x + j'_y)} \cdot \\
&\quad \cdot \binom{k_x}{j_x} \binom{k_x}{j'_x} \binom{k_y}{j_y} \binom{k_y}{j'_y} \cdot \\
&\quad \cdot \frac{\sqrt{(l_x + m'_x)!(l_y + m'_y)!m'_x!m'_y!}}{(l_x + m'_x - j_x)!(l_y + m'_y - j_y)!(m'_x - j'_x)!(m'_y - j'_y)!}.
\end{aligned}$$

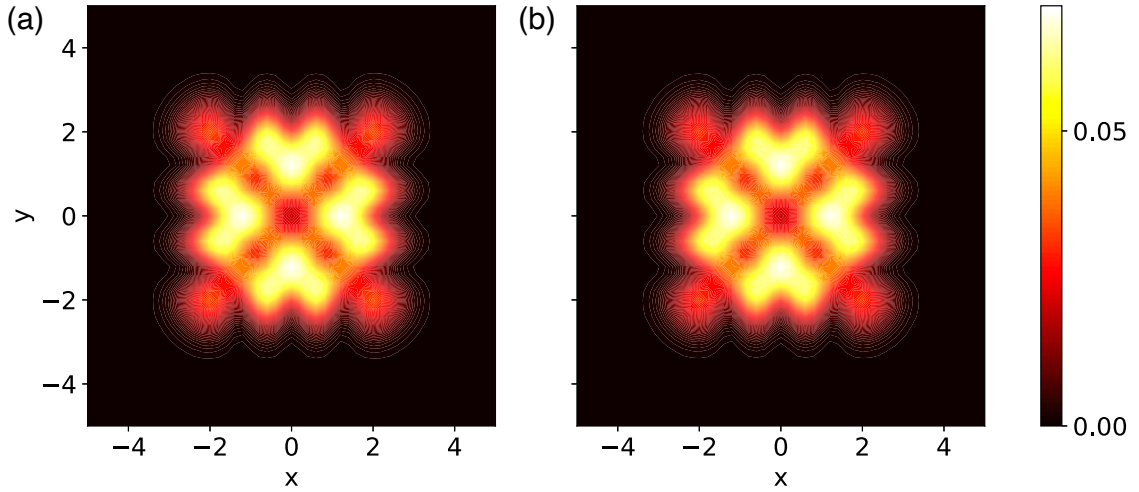


FIGURE A.1: (a) The contour plot presents the ideal spacial probability,  $|\Phi(x,y)|^2 = \langle x, y | \rho | x, y \rangle$ , of the two-dimensional motional entangling state,  $|0\rangle_x |0\rangle_y + e^{i\pi/2} |1\rangle_x |1\rangle_y + e^{i\pi} |2\rangle_x |2\rangle_y + e^{i3\pi/2} |3\rangle_x |3\rangle_y$ . (b) The plot shows the spacial probability reconstructed by the method that is introduced in this section.

In experiments, we measure  $Q_{k_x, k_y}(\alpha, \beta)$  and apply Fourier transform to obtain  $Q_{k_x, k_y}^{(l_x, l_y)}$ , and then we can reconstruct the diagonal terms of  $\rho_{(l_x+m'_x), (l_y+m'_y), m'_x, m'_y}$  by knowing the value of  $\gamma_{k_x, m'_x, k_y, m'_y}^{(l_x, l_y)}$ . We can reduce the times of measurement in the two-dimensional motional state determination experiment using this method. For example, if we would like to determine a two-dimensional motional entangling state  $|0\rangle_x |0\rangle_y + e^{i\pi/2} |1\rangle_x |1\rangle_y + e^{i\pi} |2\rangle_x |2\rangle_y + e^{i3\pi/2} |3\rangle_x |3\rangle_y$  [142], we can reconstruct the density matrix of the motional state with 64 measurements as shown in Fig. A.1 using this method.

# Appendix B

## Phase Issues in Experiments and Simulations

### B.1 Optical Phase Continuity in FM MS Gate Simulation

During frequency-modulated gates, RF signals with varying frequencies are delivered to an AOM, while the optical phase of the light is always continuous. The FM gate is designed under the phase continuity condition. In the experiment, the phase continuity is taken care of by the phase accumulator in DDS/RFSoC. When an AWG is used, it must emulate the phase accumulator to maintain continuity. Similarly, master equation simulation requires the same phase continuity treatment.

An easy approach to understand it is to think about applying discrete pulse sequences with frequencies  $\{\omega_1, \omega_2, \dots, \omega_n, \dots\}$ . Let us assume that the phase at the beginning of the  $i$ -th segment is  $\phi_i$  and the initial phase is  $\phi_0$ . Since the optical phase must be continuous we have

$$\phi_{n+1} = \sum_{i=1}^n \omega_i \cdot \tau + \phi_0,$$

where  $\tau$  is the duration of each segment.

In the  $n + 1$ -th segment, the start phase is represented as  $\omega_{n+1} \cdot n\tau + \phi_0^{n+1}$  in the

Hamiltonian. Therefore, we have

$$\begin{aligned}
\omega_{n+1} \cdot n\tau + \phi_0^{n+1} &= \sum_{i=1}^n \omega_i \cdot \tau + \phi_0 \\
\phi_0^{n+1} &= \sum_{i=1}^n \omega_i \tau - \omega_{n+1} n \tau + \phi_0 \\
&= \left( \sum_{i=1}^n \omega_i - \omega_{n+1} n \right) \tau + \phi_0.
\end{aligned}$$

We set the phase  $\phi_0^{n+1}$ ,  $n \in \{0, 1, 2, \dots\}$  as  $(\sum_{i=1}^n \omega_i - \omega_{n+1} n) \tau + \phi_0$  in the AWG and the master equation simulator to emulate a phase accumulator.

When we have a continuous frequency modulated pulse  $\omega(t)$ , a similar result can be obtained:

$$\phi_0(t) = \int_0^t \omega(t') dt' - \omega(t)t + \phi_0,$$

by substituting the summation with the integration.

## B.2 RFSoC Phase Synchronization

The task of phase controlling in quantum circuits has been simplified with the phase bookkeeping function provided by RFSoC [39]. The RFSoC is able to generate a signal of  $2^{48}$  different frequencies, and it keeps recording the phase for every frequency. Unlike a traditional DDS, the phase coherence maintains even if we switch the frequency of one RFSoC output channel.

In trapped-ion quantum computers, we usually face the situation that the ac stark shifts of single-qubit and two-qubit gates are different. It is not a fundamental limitation if someone uses an AWG with careful phase bookkeeping. However, with the RFSoC, we can solve the problem easily. Let us consider an example of a portion of the quantum circuit as shown in Fig. B.1.

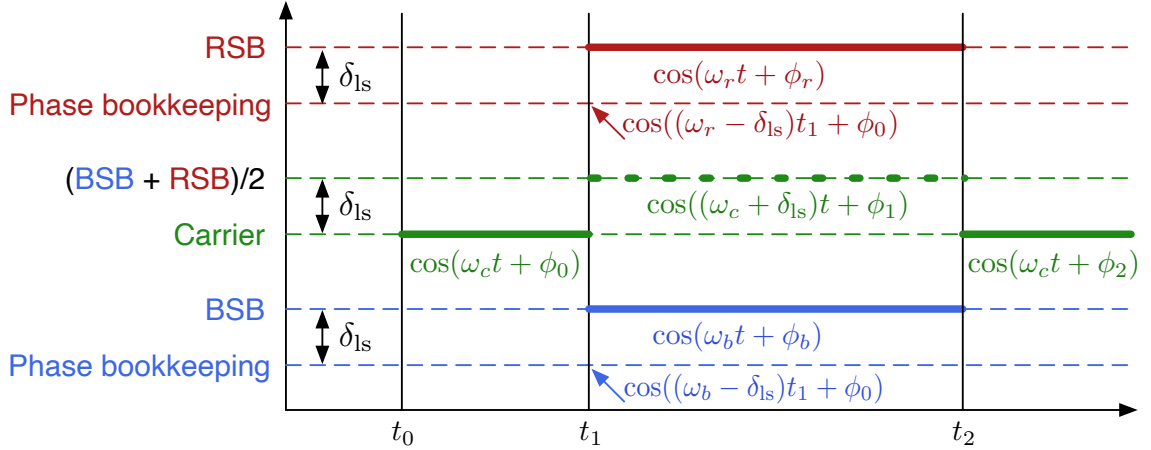


FIGURE B.1: **Phase control scheme using RFSoC** From  $t_0$  to  $t_1$ , a single-qubit gate driving by carrier frequency is implemented; from  $t_1$  to  $t_2$ , a two-qubit gate driving by two-tone rf signal is implemented; when  $t > t_2$ , another single-qubit gate is implemented. An ac Stark shift difference between single and two-qubit gates are represented by  $\delta_{ls}$  in the figure.

Let us assume for one qubit, during time  $t_0 < t < t_1$  and time  $t > t_2$ , we implement a single-qubit gate on it using a signal with frequency  $\omega_c$ , which is the calibrated carrier frequency. When  $t_1 < t < t_2$ , we implement a MS rotation with a blue tone ( $\omega_b$ ) and a red tone ( $\omega_r$ ). Because of the Stark shift difference, we observe that  $(\omega_r + \omega_b)/2 - \omega_r = \delta_{ls}$ . Without loss of generality, we assume the single-qubit rotation is along  $X$  axis, and the two-qubit rotation is along  $YY$  axis. In this case, the phase is continuous. Therefore, we have several conditions to satisfy:

$$\omega_r t_1 + \phi_r = (\omega_r - \delta_{ls}) t_1 + \phi_0 \quad (B.1)$$

$$\omega_b t_1 + \phi_b = (\omega_b - \delta_{ls}) t_1 + \phi_0 \quad (B.2)$$

$$\omega_c t_1 + \phi_0 = (\omega_c + \delta_{ls}) t_1 + \phi_1 \quad (B.3)$$

$$(\omega_c + \delta_{ls}) t_2 + \phi_1 = \omega_c t_2 + \phi_2 \quad (B.4)$$

We can fulfill the conditions by defining the two-qubit gate pulse in the following ways:

- The blue tone ( $\omega_b$ ) is started with the phase recorded by frequency  $\omega_b - \delta_{ls}$ .

We synchronize the phase at frequency  $\omega_b - \delta_{ls}$  (with synchronization mask on) before running the pulse at frequency  $\omega_b$  (with synchronization mask off).

- The red tone ( $\omega_r$ ) is started with the phase recorded by frequency  $\omega_r - \delta_{ls}$ , using the same method as above.
- Advance the phase by  $\delta_{ls}(t_2 - t_1)$  at the end of the gate, using the  $Z$ -frame rotation accumulator feature provided by RFSoC.

The single-qubit gate pulse definitions remain unchanged.

# Bibliography

- [1] Richard P Feynman. Quantum mechanical computers. In *Conference on Lasers and Electro-Optics*, page TUAA2. Optical Society of America, 1984.
- [2] D Deutsch. Rapid solution of problems by quantum computation. *Proceedings of the Royal Society A*, 435:563–574, 1991.
- [3] Peter W Shor. Algorithms for quantum computation: discrete logarithms and factoring. In *Proceedings 35th annual symposium on foundations of computer science*, pages 124–134. Ieee, 1994.
- [4] Lov K Grover. A fast quantum mechanical algorithm for database search. In *Proceedings of the twenty-eighth annual ACM symposium on Theory of computing*, pages 212–219, 1996.
- [5] Peter W Shor. Scheme for reducing decoherence in quantum computer memory. *Physical review A*, 52(4):R2493, 1995.
- [6] A. M. Steane. Error correcting codes in quantum theory. *Phys. Rev. Lett.*, 77:793–797, Jul 1996.
- [7] David P DiVincenzo. The physical implementation of quantum computation. *Fortschritte der Physik: Progress of Physics*, 48(9-11):771–783, 2000.
- [8] Colin D Bruzewicz, John Chiaverini, Robert McConnell, and Jeremy M Sage. Trapped-ion quantum computing: Progress and challenges. *Applied Physics Reviews*, 6(2):021314, 2019.
- [9] Alexandre Blais, Arne L Grimsmo, SM Girvin, and Andreas Wallraff. Circuit quantum electrodynamics. *Reviews of Modern Physics*, 93(2):025005, 2021.
- [10] Frank Arute, Kunal Arya, Ryan Babbush, Dave Bacon, Joseph C Bardin, Rami Barends, Rupak Biswas, Sergio Boixo, Fernando GSL Brandao, David A Buell, et al. Quantum supremacy using a programmable superconducting processor. *Nature*, 574(7779):505–510, 2019.
- [11] Yulin Wu, Wan-Su Bao, Sirui Cao, Fusheng Chen, Ming-Cheng Chen, Xiawei Chen, Tung-Hsun Chung, Hui Deng, Yajie Du, Daojin Fan, et al. Strong

- quantum computational advantage using a superconducting quantum processor. *arXiv preprint arXiv:2106.14734*, 2021.
- [12] Craig R Clark, Holly N Tinkey, Brian C Sawyer, Adam M Meier, Karl A Burkhardt, Christopher M Seck, Christopher M Shappert, Nicholas D Guise, Curtis E Volin, Spencer D Fallek, et al. High-fidelity bell-state preparation with  $^{40}\text{Ca}^+$  optical qubits. *arXiv preprint arXiv:2105.05828*, 2021.
  - [13] CJ Ballance, TP Harty, NM Linke, MA Sepiol, and DM Lucas. High-fidelity quantum logic gates using trapped-ion hyperfine qubits. *Physical review letters*, 117(6):060504, 2016.
  - [14] John P Gaebler, Ting Rei Tan, Y Lin, Y Wan, R Bowler, Adam C Keith, S Glancy, K Coakley, E Knill, D Leibfried, et al. High-fidelity universal gate set for 9+ ion qubits. *Physical review letters*, 117(6):060505, 2016.
  - [15] Juan M Pino, Jennifer M Dreiling, Caroline Figgatt, John P Gaebler, Steven A Moses, MS Allman, CH Baldwin, M Foss-Feig, D Hayes, K Mayer, et al. Demonstration of the trapped-ion quantum ccd computer architecture. *Nature*, 592(7853):209–213, 2021.
  - [16] Prakash Murali, Dripto M Debroy, Kenneth R Brown, and Margaret Martonosi. Architecting noisy intermediate-scale trapped ion quantum computers. In *2020 ACM/IEEE 47th Annual International Symposium on Computer Architecture (ISCA)*, pages 529–542. IEEE, 2020.
  - [17] Daniel A Lidar and Todd A Brun. *Quantum error correction*. Cambridge university press, 2013.
  - [18] Steve Olmschenk, Kelly C Younge, David L Moehring, Dzmitry N Matsukevich, Peter Maunz, and Christopher Monroe. Manipulation and detection of a trapped  $\text{Yb}^+$  hyperfine qubit. *Physical Review A*, 76(5):052314, 2007.
  - [19] Harold J Metcalf and Peter van der Straten. Laser cooling and trapping of atoms. *JOSA B*, 20(5):887–908, 2003.
  - [20] Giovanna Morigi, Jürgen Eschner, and Christoph H Keitel. Ground state laser cooling using electromagnetically induced transparency. *Physical review letters*, 85(21):4458, 2000.
  - [21] Mu Qiao, Ye Wang, Zhengyang Cai, Botao Du, Pengfei Wang, Chunyang Luan, Wentao Chen, Heung-Ryoul Noh, and Kihwan Kim. Double-electromagnetically-induced-transparency ground-state cooling of stationary two-dimensional ion crystals. *Physical Review Letters*, 126(2):023604, 2021.
  - [22] Melissa C Revelle. Phoenix and peregrine ion traps. *arXiv preprint arXiv:2009.02398*, 2020.

- [23] Peter Lukas Wilhelm Maunz. High optical access trap 2.0. Technical report, Sandia National Lab.(SNL-NM), Albuquerque, NM (United States), 2016.
- [24] M Cetina, LN Egan, CA Noel, ML Goldman, AR Risinger, D Zhu, D Biswas, and C Monroe. Quantum gates on individually-addressed atomic qubits subject to noisy transverse motion. *arXiv preprint arXiv:2007.06768*, 2020.
- [25] Shi-Liang Zhu, Chris Monroe, and L-M Duan. Trapped ion quantum computation with transverse phonon modes. *Physical review letters*, 97(5):050505, 2006.
- [26] David Hayes, Dzmitry N Matsukevich, Peter Maunz, David Hucul, Qudsia Quraishi, Steve Olmschenk, W Campbell, Jonathan Mizrahi, Crystal Senko, and Christopher Monroe. Entanglement of atomic qubits using an optical frequency comb. *Physical review letters*, 104(14):140501, 2010.
- [27] Laird Nicholas Egan. *Scaling Quantum Computers with Long Chains of Trapped Ions*. PhD thesis, University of Maryland, College Park, 2021.
- [28] Anders Sørensen and Klaus Mølmer. Quantum computation with ions in thermal motion. *Physical review letters*, 82(9):1971, 1999.
- [29] Anders Sørensen and Klaus Mølmer. Entanglement and quantum computation with ions in thermal motion. *Physical Review A*, 62(2):022311, 2000.
- [30] Ye Wang, Stephen Crain, Chao Fang, Bichen Zhang, Shilin Huang, Qiyao Liang, Pak Hong Leung, Kenneth R Brown, and Jungsang Kim. High-fidelity two-qubit gates using a microelectromechanical-system-based beam steering system for individual qubit addressing. *Physical Review Letters*, 125(15):150505, 2020.
- [31] David Lee Hayes. *Remote and local entanglement of ions using photons and phonons*. University of Maryland, College Park, 2012.
- [32] Crispin Gardiner, Peter Zoller, and Peter Zoller. *Quantum noise: a handbook of Markovian and non-Markovian quantum stochastic methods with applications to quantum optics*. Springer Science & Business Media, 2004.
- [33] Goran Lindblad. On the generators of quantum dynamical semigroups. *Communications in Mathematical Physics*, 48(2):119–130, 1976.
- [34] Daniel Greenbaum. Introduction to quantum gate set tomography. *arXiv preprint arXiv:1509.02921*, 2015.
- [35] Emily Mount, Daniel Gaultney, Geert Vrijen, Michael Adams, So-Young Baek, Kai Hudek, Louis Isabella, Stephen Crain, Andre van Rynbach, Peter Maunz, et al. Scalable digital hardware for a trapped ion quantum computer. *Quantum Information Processing*, 15(12):5281–5298, 2016.

- [36] Rachel Noek, Geert Vrijen, Daniel Gaultney, Emily Mount, Taehyun Kim, Peter Maunz, and Jungsang Kim. High speed, high fidelity detection of an atomic hyperfine qubit. *Optics letters*, 38(22):4735–4738, 2013.
- [37] Yves Colombe, Daniel H Slichter, Andrew C Wilson, Dietrich Leibfried, and David J Wineland. Single-mode optical fiber for high-power, low-loss uv transmission. *Optics express*, 22(16):19783–19793, 2014.
- [38] S Crain, E Mount, S Baek, and J Kim. Individual addressing of trapped  $^{171}\text{yb}^+$  ion qubits using a microelectromechanical systems-based beam steering system. *Applied Physics Letters*, 105(18):181115, 2014.
- [39] Susan M Clark, Daniel Lobser, Melissa Revelle, Christopher G Yale, David Bossert, Ashlyn D Burch, Matthew N Chow, Craig W Hogle, Megan Ivory, Jessica Pehr, et al. Engineering the quantum scientific computing open user testbed (qscout): Design details and user guide. *arXiv preprint arXiv:2104.00759*, 2021.
- [40] Pengfei Wang, Chun-Yang Luan, Mu Qiao, Mark Um, Junhua Zhang, Ye Wang, Xiao Yuan, Mile Gu, Jingning Zhang, and Kihwan Kim. Single ion qubit with estimated coherence time exceeding one hour. *Nature communications*, 12(1):1–8, 2021.
- [41] Bichen Zhang, Swarnadeep Majumder, Pak Hong Leung, Stephen Crain, Ye Wang, Chao Fang, Dripto M Debroy, Jungsang Kim, and Kenneth R Brown. Hidden inverses: Coherent error cancellation at the circuit level. *arXiv preprint arXiv:2104.01119*, 2021.
- [42] Michael A Nielsen. The entanglement fidelity and quantum error correction. *arXiv preprint quant-ph/9606012*, 1996.
- [43] Erik Nielsen, Kenneth Rudinger, Timothy Proctor, Antonio Russo, Kevin Young, and Robin Blume-Kohout. Probing quantum processor performance with pygsti. *Quantum Science and Technology*, 5(4):044002, 2020.
- [44] Ben P Lanyon, Cornelius Hempel, Daniel Nigg, Markus Müller, Rene Gerritsma, F Zähringer, Philipp Schindler, Julio T Barreiro, Markus Rambach, Gerhard Kirchmair, et al. Universal digital quantum simulation with trapped ions. *Science*, 334(6052):57–61, 2011.
- [45] A Yu Kitaev. Fault-tolerant quantum computation by anyons. *Annals of Physics*, 303(1):2–30, 2003.
- [46] Dorit Aharonov and Michael Ben-Or. Fault-tolerant quantum computation with constant error rate. *SIAM Journal on Computing*, 2008.

- [47] Shantanu Debnath, Norbert M Linke, Caroline Figgatt, Kevin A Landsman, Kevin Wright, and Christopher Monroe. Demonstration of a small programmable quantum computer with atomic qubits. *Nature*, 536(7614):63–66, 2016.
- [48] K Wright, KM Beck, Sea Debnath, JM Amini, Y Nam, N Grzesiak, J-S Chen, NC Pisenti, M Chmielewski, C Collins, et al. Benchmarking an 11-qubit quantum computer. *Nature communications*, 10(1):1–6, 2019.
- [49] Ferdinand Schmidt-Kaler, Hartmut Häffner, Mark Riebe, Stephan Gulde, Gavin PT Lancaster, Thomas Deuschle, Christoph Becher, Christian F Roos, Jürgen Eschner, and Rainer Blatt. Realization of the cirac–zoller controlled-not quantum gate. *Nature*, 422(6930):408–411, 2003.
- [50] DD Yavuz, PB Kulatunga, E Urban, Todd A Johnson, N Proite, T Henage, TG Walker, and M Saffman. Fast ground state manipulation of neutral atoms in microscopic optical traps. *Physical Review Letters*, 96(6):063001, 2006.
- [51] C. Knoernschild, X. L. Zhang, L. Isenhower, A. T. Gill, F. P. Lu, M. Saffman, and J. Kim. Independent individual addressing of multiple neutral atom qubits with a micromirror-based beam steering system. *Applied Physics Letters*, 97(13):134101, 2010.
- [52] Patricia J Lee, Kathy-Anne Brickman, Louis Deslauriers, Paul C Haljan, Lu-Ming Duan, and Christopher Monroe. Phase control of trapped ion quantum gates. *Journal of Optics B: Quantum and Semiclassical Optics*, 7(10):S371, 2005.
- [53] IV Inlek, G Vittorini, D Hucul, C Crocker, and C Monroe. Quantum gates with phase stability over space and time. *Physical Review A*, 90(4):042316, 2014.
- [54] Ting Rei Tan, John P Gaebler, Yiheng Lin, Yong Wan, R Bowler, D Leibfried, and David J Wineland. Multi-element logic gates for trapped-ion qubits. *Nature*, 528(7582):380–383, 2015.
- [55] Shi-Liang Zhu, Christopher Monroe, and L-M Duan. Arbitrary-speed quantum gates within large ion crystals through minimum control of laser beams. *EPL (Europhysics Letters)*, 73(4):485, 2006.
- [56] Christian F Roos. Ion trap quantum gates with amplitude-modulated laser beams. *New Journal of Physics*, 10(1):013002, 2008.
- [57] Todd J Green and Michael J Biercuk. Phase-modulated decoupling and error suppression in qubit-oscillator systems. *Physical review letters*, 114(12):120502, 2015.

- [58] Alistair R Milne, Claire L Edmunds, Cornelius Hempel, Federico Roy, Sandeep Mavadia, and Michael J Biercuk. Phase-modulated entangling gates robust to static and time-varying errors. *Physical Review Applied*, 13(2):024022, 2020.
- [59] Yao Lu, Shuaining Zhang, Kuan Zhang, Wentao Chen, Yangchao Shen, Jiali Zhang, Jing-Ning Zhang, and Kihwan Kim. Global entangling gates on arbitrary ion qubits. *Nature*, 572(7769):363–367, 2019.
- [60] Yotam Shapira, Ravid Shaniv, Tom Manovitz, Nitzan Akerman, and Roee Ozeri. Robust entanglement gates for trapped-ion qubits. *Physical review letters*, 121(18):180502, 2018.
- [61] Reinhold Blumel, Nikodem Grzesiak, and Yunseong Nam. Power-optimal, stabilized entangling gate between trapped-ion qubits. *arXiv preprint arXiv:1905.09292*, 2019.
- [62] Pak Hong Leung, Kevin A Landsman, Caroline Figgatt, Norbert M Linke, Christopher Monroe, and Kenneth R Brown. Robust 2-qubit gates in a linear ion crystal using a frequency-modulated driving force. *Physical review letters*, 120(2):020501, 2018.
- [63] Pak Hong Leung and Kenneth R Brown. Entangling an arbitrary pair of qubits in a long ion crystal. *Physical Review A*, 98(3):032318, 2018.
- [64] Kevin A Landsman, Yukai Wu, Pak Hong Leung, Daiwei Zhu, Norbert M Linke, Kenneth R Brown, Luming Duan, and C Monroe. Two-qubit entangling gates within arbitrarily long chains of trapped ions. *Physical Review A*, 100(2):022332, 2019.
- [65] Ye Wang, Mark Um, Junhua Zhang, Shuoming An, Ming Lyu, Jing-Ning Zhang, L-M Duan, Dahyun Yum, and Kihwan Kim. Single-qubit quantum memory exceeding ten-minute coherence time. *Nature Photonics*, 11(10):646–650, 2017.
- [66] Stephen Crain, Clinton Cahall, Geert Vrijen, Emma E Wollman, Matthew D Shaw, Varun B Verma, Sae Woo Nam, and Jungsang Kim. High-speed low-crosstalk detection of a 171  $\text{yb}^+$  qubit using superconducting nanowire single photon detectors. *Communications Physics*, 2(1):1–6, 2019.
- [67] Dietrich Leibfried, Brian DeMarco, Volker Meyer, David Lucas, Murray Barrett, Joe Britton, Wayne M Itano, B Jelenković, Chris Langer, Till Rosenband, et al. Experimental demonstration of a robust, high-fidelity geometric two ion-qubit phase gate. *Nature*, 422(6930):412–415, 2003.
- [68] Robin Blume-Kohout, John King Gamble, Erik Nielsen, Kenneth Rudinger, Jonathan Mizrahi, Kevin Fortier, and Peter Maunz. Demonstration of qubit

operations below a rigorous fault tolerance threshold with gate set tomography. *Nature communications*, 8(1):1–13, 2017.

- [69] David J Wineland, C Monroe, Wayne M Itano, Dietrich Leibfried, Brian E King, and Dawn M Meekhof. Experimental issues in coherent quantum-state manipulation of trapped atomic ions. *Journal of research of the National Institute of Standards and Technology*, 103(3):259, 1998.
- [70] Louis Deslauriers, S Olmschenk, D Stick, WK Hensinger, J Sterk, and C Monroe. Scaling and suppression of anomalous heating in ion traps. *Physical Review Letters*, 97(10):103007, 2006.
- [71] D. A. Hite, Y. Colombe, A. C. Wilson, K. R. Brown, U. Warring, R. Jördens, J. D. Jost, K. S. McKay, D. P. Pappas, D. Leibfried, and D. J. Wineland. 100-fold reduction of electric-field noise in an ion trap cleaned with in situ argon-ion-beam bombardment. *Phys. Rev. Lett.*, 109:103001, Sep 2012.
- [72] R. Ozeri, W. M. Itano, R. B. Blakestad, J. Britton, J. Chiaverini, J. D. Jost, C. Langer, D. Leibfried, R. Reichle, S. Seidelin, J. H. Wesenberg, and D. J. Wineland. Errors in trapped-ion quantum gates due to spontaneous photon scattering. *Phys. Rev. A*, 75:042329, Apr 2007.
- [73] Mingyu Kang, Qiyao Liang, Bichen Zhang, Shilin Huang, Ye Wang, Chao Fang, Jungsang Kim, and Kenneth R. Brown. Batch optimization of frequency-modulated pulses for robust two-qubit gates in ion chains. *Phys. Rev. Applied*, 16:024039, Aug 2021.
- [74] Christopher Monroe and Jungsang Kim. Scaling the ion trap quantum processor. *Science*, 339(6124):1164–1169, 2013.
- [75] Kenneth R Brown, Jungsang Kim, and Christopher Monroe. Co-designing a scalable quantum computer with trapped atomic ions. *npj Quantum Information*, 2(1):1–10, 2016.
- [76] Kenton R Brown, Andrew C Wilson, Yves Colombe, C Ospelkaus, Adam M Meier, Emanuel Knill, Dietrich Leibfried, and David J Wineland. Single-qubit-gate error below  $10^{-4}$  in a trapped ion. *Physical Review A*, 84(3):030303, 2011.
- [77] T. P. Harty, D. T. C. Allcock, C. J. Ballance, L. Guidoni, H. A. Janacek, N. M. Linke, D. N. Stacey, and D. M. Lucas. High-fidelity preparation, gates, memory, and readout of a trapped-ion quantum bit. *Phys. Rev. Lett.*, 113:220501, Nov 2014.
- [78] Emily Mount, Chingiz Kabytayev, Stephen Crain, Robin Harper, So-Young Baek, Geert Vrijen, Steven T Flammia, Kenneth R Brown, Peter Maunz, and Jungsang Kim. Error compensation of single-qubit gates in a surface-electrode ion trap using composite pulses. *Physical Review A*, 92(6):060301, 2015.

- [79] DPL Aude Craik, NM Linke, MA Sepiol, TP Harty, JF Goodwin, CJ Ballance, DN Stacey, AM Steane, DM Lucas, and DTC Allcock. High-fidelity spatial and polarization addressing of ca+ 43 qubits using near-field microwave control. *Physical Review A*, 95(2):022337, 2017.
- [80] Raghavendra Srinivas, SC Burd, HM Knaack, RT Sutherland, Alex Kwiatkowski, Scott Glancy, Emanuel Knill, DJ Wineland, Dietrich Leibfried, AC Wilson, et al. High-fidelity laser-free universal control of two trapped ion qubits. *arXiv preprint arXiv:2102.12533*, 2021.
- [81] Norbert M Linke, Dmitri Maslov, Martin Roetteler, Shantanu Debnath, Caroline Figgatt, Kevin A Landsman, Kenneth Wright, and Christopher Monroe. Experimental comparison of two quantum computing architectures. *Proceedings of the National Academy of Sciences*, 114(13):3305–3310, 2017.
- [82] Klaus Mølmer and Anders Sørensen. Multiparticle entanglement of hot trapped ions. *Physical Review Letters*, 82(9):1835, 1999.
- [83] Farhang Haddadfarshi and Florian Mintert. High fidelity quantum gates of trapped ions in the presence of motional heating. *New Journal of Physics*, 18(12):123007, 2016.
- [84] Anna E Webb, Simon C Webster, S Collingbourne, David Breaud, Adam M Lawrence, Sebastian Weidt, Florian Mintert, and Winfried K Hensinger. Resilient entangling gates for trapped ions. *Physical review letters*, 121(18):180501, 2018.
- [85] G Zarantonello, H Hahn, J Morgner, M Schulte, A Bautista-Salvador, RF Werner, K Hammerer, and C Ospelkaus. Robust and resource-efficient microwave near-field entangling be+ 9 gate. *Physical review letters*, 123(26):260503, 2019.
- [86] Yotam Shapira, Ravid Shani, Tom Manovitz, Nitzan Akerman, Lee Peleg, Lior Gazit, Roei Ozeri, and Ady Stern. Theory of robust multiqubit nonadiabatic gates for trapped ions. *Physical Review A*, 101(3):032330, 2020.
- [87] Kihwan Kim, M-S Chang, Rajibul Islam, Simcha Korenblit, L-M Duan, and Christopher Monroe. Entanglement and tunable spin-spin couplings between trapped ions using multiple transverse modes. *Physical review letters*, 103(12):120502, 2009.
- [88] Taeyoung Choi, Shantanu Debnath, TA Manning, Caroline Figgatt, Z-X Gong, L-M Duan, and Christopher Monroe. Optimal quantum control of multimode couplings between trapped ion qubits for scalable entanglement. *Physical review letters*, 112(19):190502, 2014.

- [89] Caroline Figgatt, Aaron Ostrander, Norbert M Linke, Kevin A Landsman, Dai-wei Zhu, Dmitri Maslov, and Christopher Monroe. Parallel entangling operations on a universal ion-trap quantum computer. *Nature*, 572(7769):368–372, 2019.
- [90] Christopher DB Bentley, Harrison Ball, Michael J Biercuk, Andre RR Carvalho, Michael R Hush, and Harry J Slatyer. Numeric optimization for configurable, parallel, error-robust entangling gates in large ion registers. *Advanced Quantum Technologies*, 3(11):2000044, 2020.
- [91] Re-Bing Wu, Haijin Ding, Daoyi Dong, and Xiaoting Wang. Learning robust and high-precision quantum controls. *Physical Review A*, 99(4):042327, 2019.
- [92] Ming-Zhong Ai, Yongcheng Ding, Yue Ban, José D Martín-Guerrero, Jorge Casanova, Jin-Ming Cui, Yun-Feng Huang, Xi Chen, Chuan-Feng Li, and Guang-Can Guo. Experimentally realizing efficient quantum control with reinforcement learning. *arXiv preprint arXiv:2101.09020*, 2021.
- [93] Diederik P Kingma and Jimmy Ba. Adam: A method for stochastic optimization. *arXiv preprint arXiv:1412.6980*, 2014.
- [94] Erwin L Hahn. Spin echoes. *Physical review*, 80(4):580, 1950.
- [95] Lorenza Viola, Emanuel Knill, and Seth Lloyd. Dynamical decoupling of open quantum systems. *Physical Review Letters*, 82(12):2417, 1999.
- [96] Michael J Biercuk, Hermann Uys, Aaron P VanDevender, Nobuyasu Shiga, Wayne M Itano, and John J Bollinger. Optimized dynamical decoupling in a model quantum memory. *Nature*, 458(7241):996–1000, 2009.
- [97] Haoyu Qi, Jonathan P Dowling, and Lorenza Viola. Optimal digital dynamical decoupling for general decoherence via walsh modulation. *Quantum Information Processing*, 16(11):1–18, 2017.
- [98] Gregory Quiroz and Daniel A Lidar. Optimized dynamical decoupling via genetic algorithms. *Physical Review A*, 88(5):052306, 2013.
- [99] Daniel A Lidar. Review of decoherence free subspaces, noiseless subsystems, and dynamical decoupling. *Adv. Chem. Phys.*, 154:295–354, 2014.
- [100] Junkai Zeng, Xiu-Hao Deng, Antonio Russo, and Edwin Barnes. General solution to inhomogeneous dephasing and smooth pulse dynamical decoupling. *New Journal of Physics*, 20(3):033011, 2018.
- [101] J True Merrill and Kenneth R Brown. Progress in compensating pulse sequences for quantum computation. *Adv. Chem. Phys.*, 154:241–294, 2014.

- [102] Guang Hao Low, Theodore J Yoder, and Isaac L Chuang. Optimal arbitrarily accurate composite pulse sequences. *Physical Review A*, 89(2):022341, 2014.
- [103] Guang Hao Low, Theodore J Yoder, and Isaac L Chuang. Methodology of resonant equiangular composite quantum gates. *Physical Review X*, 6(4):041067, 2016.
- [104] Kaveh Khodjasteh and Lorenza Viola. Dynamically error-corrected gates for universal quantum computation. *Physical review letters*, 102(8):080501, 2009.
- [105] Donovan Buterakos, Sankar Das Sarma, and Edwin Barnes. Geometrical formalism for dynamically corrected gates in multiqubit systems. *PRX Quantum*, 2(1):010341, 2021.
- [106] Joel J Wallman and Joseph Emerson. Noise tailoring for scalable quantum computation via randomized compiling. *Physical Review A*, 94(5):052325, 2016.
- [107] Daniel A Lidar, Isaac L Chuang, and K Birgitta Whaley. Decoherence-free subspaces for quantum computation. *Physical Review Letters*, 81(12):2594, 1998.
- [108] Paul G Kwiat, Andrew J Berglund, Joseph B Altepeter, and Andrew G White. Experimental verification of decoherence-free subspaces. *Science*, 290(5491):498–501, 2000.
- [109] Dripto M Debroy, Laird Egan, Crystal Noel, Andrew Risinger, Daiwei Zhu, Debopriyo Biswas, Marko Cetina, Chris Monroe, and Kenneth R Brown. Optimizing stabilizer parities for improved logical qubit memories. *arXiv preprint arXiv:2105.05068*, 2021.
- [110] Dripto M Debroy, Muyuan Li, Michael Newman, and Kenneth R Brown. Stabilizer slicing: coherent error cancellations in low-density parity-check stabilizer codes. *Physical review letters*, 121(25):250502, 2018.
- [111] Stefanie J Beale, Joel J Wallman, Mauricio Gutiérrez, Kenneth R Brown, and Raymond Laflamme. Quantum error correction decoheres noise. *Physical review letters*, 121(19):190501, 2018.
- [112] Eric Huang, Andrew C Doherty, and Steven Flammia. Performance of quantum error correction with coherent errors. *Physical Review A*, 99(2):022313, 2019.
- [113] Joseph K Iverson and John Preskill. Coherence in logical quantum channels. *New Journal of Physics*, 22(7):073066, 2020.
- [114] James D Whitfield, Jacob Biamonte, and Alán Aspuru-Guzik. Simulation of electronic structure hamiltonians using quantum computers. *Molecular Physics*, 109(5):735–750, 2011.

- [115] Panagiotis Kl Barkoutsos, Jerome F Gonthier, Igor Sokolov, Nikolaj Moll, Gian Salis, Andreas Fuhrer, Marc Ganzhorn, Daniel J Egger, Matthias Troyer, Antonio Mezzacapo, et al. Quantum algorithms for electronic structure calculations: Particle-hole hamiltonian and optimized wave-function expansions. *Physical Review A*, 98(2):022322, 2018.
- [116] Dmitri Maslov. Basic circuit compilation techniques for an ion-trap quantum machine. *New Journal of Physics*, 19(2):023035, 2017.
- [117] AH Myerson, DJ Szwarc, SC Webster, DTC Allcock, MJ Curtis, G Imreh, JA Sherman, DN Stacey, AM Steane, and DM Lucas. High-fidelity readout of trapped-ion qubits. *Physical Review Letters*, 100(20):200502, 2008.
- [118] Emily Mount, So-Young Baek, Matthew Blain, Daniel Stick, Daniel Gaultney, Stephen Crain, Rachel Noek, Taehyun Kim, Peter Maunz, and Jungsang Kim. Single qubit manipulation in a microfabricated surface electrode ion trap. *New Journal of Physics*, 15(9):093018, 2013.
- [119] Jonathan A Jones. Robust ising gates for practical quantum computation. *Physical Review A*, 67(1):012317, 2003.
- [120] Yu Tomita, JT Merrill, and Kenneth R Brown. Multi-qubit compensation sequences. *New Journal of Physics*, 12(1):015002, 2010.
- [121] Daniel C Murphy and Kenneth R Brown. Controlling error orientation to improve quantum algorithm success rates. *Physical Review A*, 99(3):032318, 2019.
- [122] Kenneth R Brown, Robert J Clark, and Isaac L Chuang. Limitations of quantum simulation examined by simulating a pairing hamiltonian using nuclear magnetic resonance. *Physical review letters*, 97(5):050504, 2006.
- [123] Yunseong Nam, Jwo-Sy Chen, Neal C Pisenti, Kenneth Wright, Conor De-laney, Dmitri Maslov, Kenneth R Brown, Stewart Allen, Jason M Amini, Joel Apisdorf, et al. Ground-state energy estimation of the water molecule on a trapped-ion quantum computer. *npj Quantum Information*, 6(1):1–6, 2020.
- [124] Peter JJ O’Malley, Ryan Babbush, Ian D Kivlichan, Jonathan Romero, Jarrod R McClean, Rami Barends, Julian Kelly, Pedram Roushan, Andrew Tranter, Nan Ding, et al. Scalable quantum simulation of molecular energies. *Physical Review X*, 6(3):031007, 2016.
- [125] Esteban A Martinez, Thomas Monz, Daniel Nigg, Philipp Schindler, and Rainer Blatt. Compiling quantum algorithms for architectures with multi-qubit gates. *New Journal of Physics*, 18(6):063029, 2016.

- [126] Yunong Shi, Nelson Leung, Pranav Gokhale, Zane Rossi, David I Schuster, Henry Hoffmann, and Frederic T Chong. Optimized compilation of aggregated instructions for realistic quantum computers. In *Proceedings of the Twenty-Fourth International Conference on Architectural Support for Programming Languages and Operating Systems*, pages 1031–1044, 2019.
- [127] Prakash Murali, Jonathan M Baker, Ali Javadi-Abhari, Frederic T Chong, and Margaret Martonosi. Noise-adaptive compiler mappings for noisy intermediate-scale quantum computers. In *Proceedings of the Twenty-Fourth International Conference on Architectural Support for Programming Languages and Operating Systems*, pages 1015–1029, 2019.
- [128] Lukasz Cincio, Kenneth Rudinger, Mohan Sarovar, and Patrick J Coles. Machine learning of noise-resilient quantum circuits. *PRX Quantum*, 2(1):010324, 2021.
- [129] Kunal Sharma, Sumeet Khatri, Marco Cerezo, and Patrick J Coles. Noise resilience of variational quantum compiling. *New Journal of Physics*, 22(4):043006, 2020.
- [130] Kübra Yeter-Aydeniz, Bryan T Gard, Jacek Jakowski, Swarnadeep Majumder, George S Barron, George Siopsis, Travis S Humble, and Raphael C Pooser. Benchmarking quantum chemistry computations with variational, imaginary time evolution, and krylov space solver algorithms. *Advanced Quantum Technologies*, page 2100012, 2021.
- [131] David Kielpinski, Chris Monroe, and David J Wineland. Architecture for a large-scale ion-trap quantum computer. *Nature*, 417(6890):709–711, 2002.
- [132] Hiroki Takahashi, Ezra Kassa, Costas Christoforou, and Matthias Keller. Strong coupling of a single ion to an optical cavity. *Physical review letters*, 124(1):013602, 2020.
- [133] Markus Müller, Linmei Liang, Igor Lesanovsky, and Peter Zoller. Trapped rydberg ions: from spin chains to fast quantum gates. *New Journal of Physics*, 10(9):093009, 2008.
- [134] T Feldker, P Bachor, M Stappel, D Kolbe, R Gerritsma, J Walz, and F Schmidt-Kaler. Rydberg excitation of a single trapped ion. *Physical review letters*, 115(17):173001, 2015.
- [135] Gerard Higgins, Fabian Pokorny, Chi Zhang, Quentin Bodart, and Markus Hennrich. Coherent control of a single trapped rydberg ion. *Physical review letters*, 119(22):220501, 2017.

- [136] Jonas Vogel, Weibin Li, Arezoo Mokhberi, Igor Lesanovsky, and Ferdinand Schmidt-Kaler. Shuttling of rydberg ions for fast entangling operations. *Physical review letters*, 123(15):153603, 2019.
- [137] Laird Egan, Dripto M Debroy, Crystal Noel, Andrew Risinger, Daiwei Zhu, Debopriyo Biswas, Michael Newman, Muyuan Li, Kenneth R Brown, Marko Cetina, and Christopher Monroe. Fault-tolerant operation of a quantum error-correction code. *arXiv preprint arXiv:2009.11482*, 2020.
- [138] C Ryan-Anderson, JG Bohnet, K Lee, D Gresh, A Hankin, JP Gaebler, D Francois, A Chernoguzov, D Lucchetti, NC Brown, et al. Realization of real-time fault-tolerant quantum error correction. *arXiv preprint arXiv:2107.07505*, 2021.
- [139] Iris Cong, Sheng-Tao Wang, Harry Levine, Alexander Keesling, and Mikhail D Lukin. Hardware-efficient, fault-tolerant quantum computation with rydberg atoms. *arXiv preprint arXiv:2105.13501*, 2021.
- [140] J Pablo Bonilla Ataides, David K Tuckett, Stephen D Bartlett, Steven T Flammia, and Benjamin J Brown. The xzzx surface code. *Nature communications*, 12(1):1–12, 2021.
- [141] Dietrich Leibfried, DM Meekhof, BE King, CH Monroe, Wayne M Itano, and David J Wineland. Experimental determination of the motional quantum state of a trapped atom. *Physical Review Letters*, 77(21):4281, 1996.
- [142] Zhubing Jia et al. in preparation.

# Biography

Bichen Zhang attended the University of Science and Technology of China (USTC) from 2011 to 2015, majoring in physics. After graduating from USTC, Bichen entered the physics doctorate program at Georgia Institute of Technology, working with Professor Ken Brown. Bichen received a Master’s Degree in physics in 2017, and he transferred to Duke University as a PhD student in Electrical and Computer Engineering together with Ken’s relocation in January 2018. Bichen’s research has been focused on experimental ion trap quantum computing, first with Ken at Georgia Tech and then Ken and Prof. Jungsang Kim at Duke. He has achieved 99.7%+ two-qubit gate fidelity in up to a three-ion chain [30], shown the advantage of a control technique called hidden inverses for reducing systematic errors [41], and implemented complex frequency-modulated gates generated by batch optimization techniques [73]. After finish his PhD work in September 2021, Bichen will join Princeton University as a postdoctoral research associate, working on neutral atom qubits with Professor Jeff Thompson.